Design of Oxidation Catalysts Based on Bimetal Effect among Two Metal/Metal Oxide Components

二種の金属/金属酸化物間のバイメタル効果に基づいた酸化触媒の設計

Yuji MAHARA

馬原　優治

Department of Molecular Design and Engineering, Graduate School of Engineering
Nagoya University

2018

Preface

Nowadays, the population all over the world exceeds 7 billion people and many developing countries undergo remarkable economic growth. It is expected that all human beings will be filled with things, and discharge exhaust gas while consuming more nature resources and energy.

Development of new heterogeneous catalysts is an important issue for both efficient energy conversion, exhaust gas purification, and reduction of the usage of metal resources. Heterogeneous catalysts are used to efficiently advance a lot of chemical and industrial processes. A supported-metal catalyst is representative and is most useful heterogeneous catalysts. Human beings have traditionally changed the type of "support" and "metal" of catalysts, and have adapted supported-metal catalysts for various catalytic reactions. However, the number of usable elements is limited to about 80 kinds for Human beings. For further development of new supported metal catalysts, "bimetallization" is indispensable.

The studies in this thesis focus on the development of bimetal catalyst used for oxidation reaction and elucidation of its performance enhancement mechanism. The studies in this thesis were carried out under the guidance of Professor Atsushi Satsuma, Dr. Kyoichi Sawabe, and Dr. Junya Ohyama at Graduate School of Engineering, Nagoya University during the period from April 2013 to February 2018.

The author would like to express his sincere gratitude to Professor Atsushi Satsuma for his exact guidance, fruitful discussions, and valuable comments throughout this study. The author makes grateful acknowledgements to Dr. Kyoichi Sawabe for his instructive discussions and continual encouragement. The author is deeply grateful to Dr. Junya Ohyama for his valuable supervision, insightful suggestions, and helpful supports.

The author also make acknowledgements to Professor Ken-ichi Shimizu at Hokkaido University for our collaboration works. The author demonstrates his gratitude at Professor Tsunehiro Tanaka at Kyoto University, Professor Hiromi Yamashita at Osaka University, Professor Tetsuya Shishido at Tokyo Metropolitan University, Professor Tatsuya Tsukuda at the University of Tokyo, Professor Hisao Yoshida at Kyoto University, Professor Tomoko Yoshida at Osaka City University, Professor Seiji Yamazoe at Tokyo Metropolitan University, Professor Jeroen A van Bokhoven at Paul Scherrer Institut, Dr. Kentaro Teramura at Kyoto University, Dr. Saburo Hosokawa at Kyoto University, Dr. Masazumi Tamura at Tohoku University, Dr. Hiroyuki Asakura at Kyoto University, Dr. Hiroki Miura at Tokyo Metropolitan University, Dr. Shun Nishimura at Japan Advanced Institute of Science and Technology, Dr. Yohei Uemura at Institute for Molecular Science, Dr. Akira Yamamoto at Kyoto University, and Dr. Maxim Zabilskiy at Paul Scherrer Institut for their valuable discussions, warmhearted advices and cheerful messages. The author would like to thank Ryusuke Kanao, Takumi Tojo, Kakuya Ueda, Hiroyuki Ishikawa, Takumi Nishiyama, and Kazumasa Murata for fruitful discussion and competition.

The author wishes to express his appreciation to Prof. Shigeo Arai and Mr. Yuta Yamamoto at

High Voltage Electron Microscope Laboratory, Nagoya University for the grateful guidance of TEM. The author also would like to thank Mr. Kazuo Kato at Japan Synchrotron Radiation Research Institute for in situ XAFS measurements.

The author grateful acknowledgements to Grant-in-Aids from the Ministry of Education, Culture, Sports, Science and Technology (MEXT) and Elements Strategy Initiative for Catalysts and Batteries (ESICB) program. The author deeply appreciates financial supports from Japan Society for the Promotion of Science (JSPS). The author thanks to Integrative Graduate Education and Research Program in Green Natural Sciences (IGER).

The author would like to express a lot of appreciation to all member of Satsuma Laboratory. Thanks to them, the author was able to have a wonderful experience with both physical and mental health.

Finally, the author thanks his parents, brothers, and fiancé for their understanding and encouragements.

Yuji Mahara

Nagoya,
January 9, 2018

CONTENTS

General introduction

Current Study of Catalyst

Catalyst is functional substance used for efficient conversion of chemical material and energy, synthesis of monomers, purification of harmful gasses for environmental preservation, etc. Along with the explosive population increase in developing countries, more efficient use of resources and energy all over the world is required.

Catalysts include homogeneous catalysts that dissolve in solution to promote chemical reactions and heterogeneous catalysts that function in different phases from the reactants. Heterogeneous catalysts, which are easy to separate from reactants, is mainly used as an industrial catalyst. A supported-metal catalyst is a heterogeneous catalyst applied to the most various reactions.[1-3] For metal nanoparticles, noble metal (*i.e.* Pt, Pd, Rh, Ru, Ir, Au, Ag) and transition metal (*i.e.* Cu, Ni, Co, Fe, Mn, V) oxides are used for the intended reaction. As a support, mainly metal oxides with a high surface area (for example, SiO_2, Al_2O_3, TiO_2, CeO_2, ZrO_2, MgO, etc.) or carbon, silicon carbide (SiC), boron nitride (BN), zeolite and mesoporous silica are chosen. Since the catalytic metal is dispersed on the support in nanometer size, many active sites can react as compared with bulk metal.[4] In addition, coordinatively unsaturated metal site called steps, edges, and kinks are active sites with high catalytic reactivity. Supported-metal catalysts have been put to practical use in surprisingly varied reactions and catalytic systems. However, there is a number of challenging catalytic reactions still to be solved. And, this catalyst development is desirable to use base metals as abundant as possible on the earth. The design and synthesis of novel supported-metal catalysts is a crucial theme for sustainable chemistry and efficient energy conversion.

Study of Oxidation Catalysts

Oxidation catalysts have been especially studied and put to practical use.[2,5,6] For example, CO and hydrocarbon discharged from the engine downstream of the automobile are converted to harmless CO_2 and H_2O by using the oxidation catalyst.[2] Methane, which is an unburned substance that can be discharged at the thermal power generation and natural gas vehicle, has a global warming potential of about 20 times that of CO_2, and it needs to be burned completely by oxidation catalyst to prevent it from being discharged to the atmosphere.[7-10]

The reaction mechanism of the oxidation reaction is classified into Langmuir-Hinshelwood (LH), Eley-Rideal (ER) and Mars-Van Krevelen (MK) kinetics. Regarding the CO oxidation reaction under the lean-burn condition, the reaction often proceeds on the noble metal catalyst such as Pd or Pt with the LH mechanism in which the O_2 dissociation is the rate-limiting step. Although CO oxidation on CoO_x and FeO_x proceeds by the MK mechanism, the turnover frequency for the reaction is lower than that using Pd or Pt catalysts. In the case of methane oxidation, C–H dissociation of CH_4 is the most significant step. The reaction proceeds most efficiently in the MK mechanism where O is used with PdO on C–H dissociation. From the above, particularly useful

catalysts for the oxidation reactions are platinum group metals (PGMs) catalysts such as Pt and Pd. However, PGMs are expensive and rare. From the elemental viewpoint, a reduction in PGM usage or the development of alternative oxidation catalysts are desired.

Bimetal Catalyst Based on Metal-Metal Interaction

Bimetallization is one of the powerful approaches for catalysts development. Catalytic activity and selectivity are often promoted by combining two different metals because of metal–metal interactions. Regarding bimetallic catalysts, since the study of dehydrogenation using alloy catalysts was reported in 1950 by *Schwab*,[11] the influence of metal–metal interaction on catalytic performance has been studied experimentally or theoretically. Metal–metal interactions modify catalytic properties via several factors: (1) the ligand effect, where changes in the electronic state of metal surfaces influence the reactivity of the catalyst;[12-14] (2) the ensemble effect, where the unique geometric structure of bimetallic catalysts allows/forbids the progress of catalytic reactions;[15-17] (3) the strain effect, where disorder in the atomic arrangement due to the mismatching of lattice constants changes the catalytic activity.[18] These bimetallic effects influence the catalyst performance by causing a change in the outermost shell d band of the catalyst surface involved in adsorption or desorption of the reactant. Nørskov and co-workers revealed that the adsorption or desorption energy of the reactants can be predicted at the position of the center of the d-band relative to the Fermi level (d-band-center theory).[19-21] Based on the above theory, we need to design metal combinations or bimetal structures to successfully adjust the position of d-band-center.

Finding alternatives to PGMs that contain only base metal is an arduous task, and the most practical method is to combine a noble and a base metal. The structure of the bimetallic catalyst is classified into a solid solution, core shell, and Janus (phase separation type) as shown in Fig. 1.

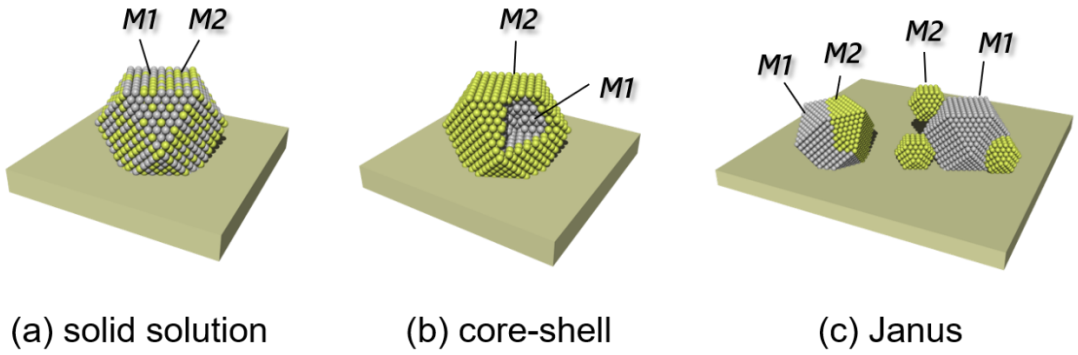

Figure 1. Schematic representation of bimetal structure: (a) solid solution, (b) core-shell, and (c) Janus.

Since a closer contact between heterogeneous metals leads to stronger metal–metal interaction, ultimately, the electronic state may drastically change in the solid solution (alloy) form. However, many substitutional alloys of noble and base metals are unstable because of the mismatching of their

lattice constants and crystal structures. For example, with respect to alloys of Ag and base metals, Ag–Co and Ag–Ni are immiscible combinations.[22-24] Similarly, Ru–Co, Ru–Cu and Ru–Ni are immiscible because of the differences in crystal structure.[25,26] In the case of Pd, even when Pd–M (M: V, Mn, Fe, Co, Ni, Zn, Sn) is synthesised as alloy particles, phase separation occurs depending on the temperature and gaseous atmosphere.[27,28] Therefore, the investigation of stable and highly active catalysts with a phase-separated structure (core-shell or Janus) is reasonable.

Metal–Metal Oxide Interaction among Bimetal Catalyst

As in the above example,[28] when the bimetallic catalysts between noble metals and base metal are applied to the oxidation reaction, it is possible that the catalytic metal is oxidized due to the high temperature under the reaction and the oxygen gas atmosphere. In these cases, the bimetallic effect works as a metal-metal oxide interaction. This interaction can affect electronic modification of metal[29-32] (like the ligand effect) and mobility of adsorbate. Regarding the latter, oxygen (O) can move through contact between metal and metal oxide. CeO_2 and CeO_2-ZrO_2 have oxygen storage capacity (OSC) and promote catalytic activity for CO, methane, and ethane oxidation by contact with catalytic metals.[33-37] As an example other than CeO_2, it have been reported that when metal oxides such as Co_3O_4 and $NiAl_2O_4$ contact with Pd, methane oxidation activity is promoted due to electronic interaction or exchange of oxygen at the interface.[38-40] Therefore, the activity for the reaction where the oxidation-reduction (redox) of the metal is a key factor in methane combustion is improved due to the metal-metal oxide interaction.

From the above two sections, it is necessary to develop regarding metal-metal interaction and metal-metal oxide interaction with the core-shell or Janus structure in accordance with the desired oxidation reaction.

Preparation Method of Bimetal Catalyst

Preparation of bimetallic nanoparticles from metal salts can be divided into two groups; co-reduction and sequential reduction of two metal precursor.[41,42] In the co-reduction method, bimetal catalyst with a solid solution structure is prepared by using the co-impregnation method with H_2 reduction at relatively high temperature.[43,44] By using organic ligands and acetylacetonate complex as precursor metals, bimetallic catalysts with further controlled size and structure are synthesized.[28] In sequential reduction, a core-shell or Janus type bimetallic catalyst is prepared by using a difference in reactivity between a metal precursor and a reducing agent (citrate, alcohol, amine).[32,45,46] In the examples of the preparation method described above, bimetallic catalysts were prepared using external reduction agents such as H_2, amines, alcohols as complete agents. Furthermore, bimetallic catalysts prepared by redox reaction between different metals have also been reported.

Galvanic deposition (GD) is a useful preparation method for making a bimetallic catalyst with

a core shell or Janus structure. Scheme 1 shows an overview of the GD method. With the GD method, a metal (M_1) having a high ionisation tendency is previously reduced and supported, and a solution that contains ions of another metal (M_2) with a relatively low ionisation tendency is dropped thereon, whereby M_2 is stabilised on M_1 according to the following formula:

$$nM_1^0 + mM_2^{n+} \rightarrow nM_1^{m+} + mM_2^0$$

As a result, the M_2 monolayer, which provides good active sites, ideally precipitates on M_1 particles. Thereafter, the underlying metal is eroded by the additive metal, thus exposing a unique surface, and the added metal is deposited on this surface. This contact could cause higher strain and stronger metal–metal interactions than that of the bimetallization among stable phases. The GD method has attracted attention as a method of preparing electrode catalysts for fuel cells.[47-57] In recent years, it has been applied to a wide range of reactions such as hydrogenation,[58-62] oxidation[38] and selective reduction.[63,64]

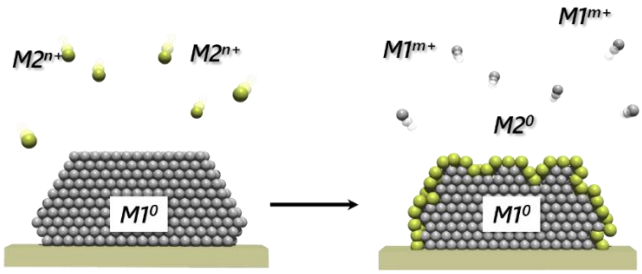

Scheme 1. Illustration of GD method.

Outline of This Thesis

On these backgrounds, I aim to synthesize bimetal catalysts with core-shell/Janus structure using the galvanic deposition method for oxidation reaction, studied the metal–metal interaction and metal–metal oxide interaction of these catalysts, and developed catalysts which demonstrates high performance.

In Part I of this thesis, the metal–metal interaction is demonstrated by CO oxidation as a model in which the metallic species is an active species. Chapter 1 establishes synthesize of Ni-Ag core-shell (Ni@Ag) catalysts for the CO oxidation. These Ag-system bimetal catalysts are prepared to aim to be instead of conventional PGM catalysts. In Chapter 2, the metal–metal interactions of these Ni@Ag catalysts are demonstrated for using other 3d transition metals (Fe, Co, and Cu) instead of Ni. The theoretical study suggests the modification of the density of states of Ag.

In Part II of this thesis, we have verified the metal–metal oxide interaction by using the methane combustion and automotive three-way reaction. In Chapter 3, Pd-Co catalysts with a phase-separated structure is prepared by galvanic deposition and used for methane combustion. Chapter 4 establishes the synthesis of Pd-$CoAl_2O_4$ catalysts having further high activity for methane combustion. The metal–metal oxide interaction is demonstrated as the investigation of redox cycle

among Pd^0-PdO using *operando* X-ray absorption fine structure (XAFS). In Chapter 5, time-resolved in situ XAFS analysis is demonstrated to clarify redox cycle among Pd^0-PdO under methane combustion. Finally, to apply the metal–metal oxide interaction, chapter 6 is intended to synthesize a noble Co-Ru core-shell (Co@Ru) catalysts for three-way reaction.

The prospect of this study is to develop new bimetallic catalysts, design catalysts for oxidation reactions, and contribute to higher performance and resource saving of catalysts.

References

1 Blaser, H. U. *et al. Adv. Synth. Catal.* **345**, 103-151, (2003).

2 Gandhi, H. S., Graham, G. W. & McCabe, R. W. *J. Catal.* **216**, 433-442, (2003).

3 Grunes, J., Zhu, J. & Somorjai, G. A. *Chemical Communications*, (2003).

4 Zheng, N. & Stucky, G. D. *J. Am. Chem. Soc.* **128**, 14278-14280, (2006).

5 Engel, T. & Ertl, G. *Adv. Catal.* **28**, 1-78, (1979).

6 Thormählen, P., Skoglundh, M., Fridell, E. & Andersson, B. *J. Catal.* **188**, 300-310, (1999).

7 Centi, G. *J. Mol. Catal. A: Chem.* **173**, 287-312, (2001).

8 Choudhary, T., Banerjee, S. & Choudhary, V. *Appl. Catal., A* **234**, 1-23, (2002).

9 Castellazzi, P. *et al. Catal. Today* **155**, 18-26, (2010).

10 Farrauto, R. J. *Science* **337**, 659-660, (2012).

11 Schwab, G.-M. *Discussions of the Faraday Society* **8**, 166-171, (1950).

12 Greeley, J. & Nørskov, J. K. *Surf. Sci.* **592**, 104-111, (2005).

13 Zhang, J., Jin, H., Sullivan, M. B., Lim, F. C. & Wu, P. *Phys. Chem. Chem. Phys.* **11**, 1441-1446, (2009).

14 Xie, S. *et al. Nano Lett.* **14**, 3570-3576, (2014).

15 Chen, M. S. & Goodman, D. W. *Science* **306**, 252-255, (2004).

16 Gao, F. & Goodman, D. W. *Chem. Soc. Rev.* **41**, 8009-8020, (2012).

17 Miura, H., Endo, K., Ogawa, R. & Shishido, T. *ACS Catal.* **7**, 1543-1553, (2017).

18 Mavrikakis, M., Hammer, B. & Nørskov, J. K. *Phys. Rev. Lett.* **81**, 2819, (1998).

19 Hammer, B. & Nørskov, J. K. *Adv. Catal.* **45**, 71-129, (2000).

20 Norskov, J. K. *et al. Chem. Soc. Rev.* **37**, 2163-2171, (2008).

21 Norskov, J. K., Abild-Pedersen, F., Studt, F. & Bligaard, T. *Proc. Natl. Acad. Sci.* **108**, 937-943, (2011).

22 Holewinski, A., Idrobo, J. C. & Linic, S. *Nat. Chem.* **6**, 828-834, (2014).

23 Zhang, Z., Nenoff, T. M., Huang, J. Y., Berry, D. T. & Provencio, P. P. *J. Phys. Chem. C* **113**, 1155-1159, (2009).

24 Zhang, Z. *et al. J. Phys. Chem. C*, (2010).

25 Cerro-Alarcón, M., Maroto-Valiente, A., Rodríguez-Ramos, I. & Guerrero-Ruiz, A. *Appl. Catal., A* **275**, 257-269, (2004).

26 He, X., Liang, S.-H., Li, J.-H. & Liu, B.-X. *Phys. Rev. B* **75**, (2007).

27 Persson, K., Ersson, A., Jansson, K., Iverlund, N. & Jaras, S. *J. Catal.* **231**, 139-150, (2005).

28 Willis, J. J. *et al. J. Am. Chem. Soc.* **139**, 11989-11997, (2017).

29 Senftle, T. P., van Duin, A. C. T. & Janik, M. J. *ACS Catal.* **7**, 327-332, (2016).

30 Colussi, S. *et al. Angew. Chem. Int. Ed.* **48**, 8481-8484, (2009).
31 Kopelent, R. *et al. Angew. Chem. Int. Ed.* **54**, 8728-8731, (2015).
32 Gawande, M. B. *et al. Chem. Soc. Rev.* **44**, 7540-7590, (2015).
33 Sugiura, M. *Catal. Surv. Asia* **7**, 77-87, (2003).
34 Kolli, T., Rahkamaa-Tolonen, K., Lassi, U., Savimäki, A. & Keiski, R. *Top. Catal.* **30**, 341-346, (2004).
35 Nagai, Y. *et al. Top. Catal.* **47**, 137-147, (2007).
36 Cargnello, M. *et al. Science* **337**, 713-717, (2012).
37 Satsuma, A. *et al. RSC Adv.* **4**, 54187-54193, (2014).
38 Pan, X., Zhang, Y., Miao, Z. & Yang, X. *J. Energy Chem.* **22**, 610-616, (2013).
39 Ercolino, G. *et al. Catal. Today* **257**, 66-71, (2015).
40 Chen, Z. *et al. Appl. Catal., A* **532**, 95-104, (2017).
41 Toshima, N. & Yonezawa, T. *New J. Chem.* **22**, 1179-1201, (1998).
42 Ferrando, R., Jellinek, J. & Johnston, R. L. *Chem. Rev.* **108**, 845-910, (2008).
43 Skoglundh, M., Löwendahl, L. & Otterated, J.-E. *Applied catalysis* **77**, 9-20, (1991).
44 Furukawa, S., Endo, M. & Komatsu, T. *ACS Catal.* **4**, 3533-3542, (2014).
45 Lim, B. *et al. J. Am. Chem. Soc.* **132**, 2506-2507, (2010).
46 Xiang, J. *et al. Nano Res.* **7**, 1337-1343, (2014).
47 Zhang, J., Vukmirovic, M. B., Xu, Y., Mavrikakis, M. & Adzic, R. R. *Angew. Chem. Int. Ed.* **44**, 2132-2135, (2005).
48 Price, S. W., Speed, J. D., Kannan, P. & Russell, A. E. *J. Am. Chem. Soc.* **133**, 19448-19458, (2011).
49 Papadimitriou, S. *et al. J. Phys. Chem. C* **114**, 5217-5223, (2010).
50 Lu, Y., Du, S. & Steinberger-Wilckens, R. *Appl. Catal., B* **199**, 292-314, (2016).
51 Shao, M., Liu, P., Zhang, J. & Adzic, R. *J. Phys. Chem. B* **111**, 6772-6775, (2007).
52 Wang, M. *et al. ACS Appl. Mater. Interfaces* **5**, 12708-12715, (2013).
53 Lim, B. *et al. Science* **324**, 1302-1305, (2009).
54 Mintsouli, I. *et al. J. Solid State Electrochem.* **17**, 435-443, (2012).
55 Son, J., Cho, S., Lee, C., Lee, Y. & Shim, J. H. *Langmuir* **30**, 3579-3588, (2014).
56 Shao, M., Sasaki, K., Marinkovic, N., Zhang, L. & Adzic, R. *Electrochem. Commun.* **9**, 2848-2853, (2007).
57 Zhang, H. *et al. J. Am. Chem. Soc.* **133**, 6078-6089, (2011).
58 Zhu, L. *et al. Mater. Chem. Phys.* **192**, 8-16, (2017).
59 Zhu, L. *et al. Appl. Surf. Sci.* **409**, 29-34, (2017).
60 Kim, T., Fu, X., Warther, D. & Sailor, M. J. *ACS Nano* **11**, 2773-2784, (2017).
61 Wu, Y. *et al. J. Am. Chem. Soc.* **136**, 11594-11597, (2014).
62 Yoshii, T., Nakatsuka, K., Kuwahara, Y., Mori, K. & Hiromi Yamashita, H. Y. *RSC Adv.* **7**, 22294-22300, (2017).
63 Kim, J.-H. *et al. Appl. Catal., B* **213**, 211-215, (2017).
64 Zhang, Y., Diao, W., Monnier, J. R. & Williams, C. T. *Catal. Sci. Technol.* **5**, 4123-4132, (2015).

Part I

CO Oxidation Reaction for Ag-Based Bimetal Catalysts Based on the Metal–Metal Interaction

Chapter 1
Enhanced CO oxidation Activity of Ni@Ag Core-Shell Nanoparticles

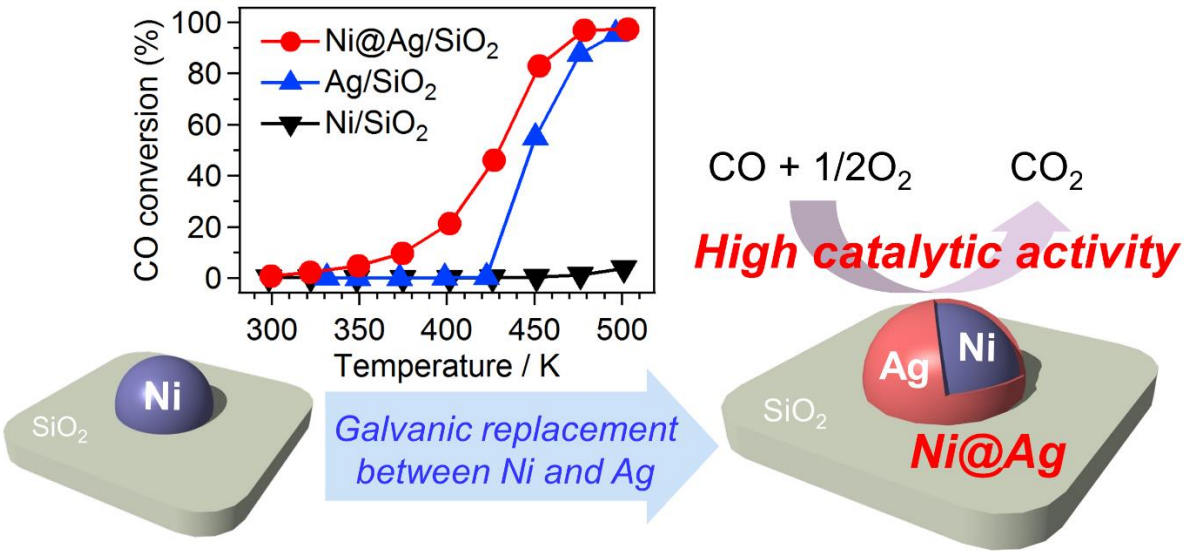

Ni@Ag core-shell nanoparticles supported on SiO_2 were prepared using a galvanic replacement reaction between Ni and Ag at low temperature (213 K). The Ni@Ag core-shell catalyst showed higher catalytic activity for CO oxidation than Ag and Ni monometallic catalysts as well as than Ni-Ag bimetallic catalyst prepared by a conventional impregnation method.

Contents

1-1. Introduction

Nobel metal catalysts, more specifically platinum group metal (PGM) catalysts, are essential for a lot of industrial processes including petroleum chemistry, synthesis of fine chemicals, and purification of exhaust gases from plant and automobile.[1-3] However, alternatives to PGMs are increasingly required due to their scarce resource and high cost. Bimetallization is one of the strategies to design new PGM-free catalysts having high catalytic performance. Among the bimetal systems, Au-Pd has been extensively investigated because of its high catalytic performance than monometallic Au and Pd catalysts for various reactions.[4-8] It is proposed that the electron transfer from Pd to Au atoms is the key to the enhanced catalytic activity of Au-Pd bimetallic catalysts.[8-11] The enhancement of catalytic activity by bimetallization is also seen in Au-Pt system.[12,13] It is expected that the bimetallization, more specifically, combination of metals in the groups 8 and 9, produces high catalytic activity. From this point of view, Ag and Ni, which are relatively abundant and cheap metals in comparison with the PGMs as well as with gold, is a promising combination.

Ag-Ni catalyst usually has phase segregated structure due to the large lattice mismatch.[14] Although Ag-Ni alloy nanoparticles has been synthesized by specific methods such as Co γ irradiation and laser ablation, the catalysis of Ag-Ni alloy nanoparticles has not been investigated so far.[15,16] It has been reported that the segregated but contacted Ag and Ni particles show enhanced catalytic activity for epoxidation of propylene and hydrogenation of benzene.[17,18] Core-shell structure, which is also a phase separated structure, often greatly improves catalytic performance of metal catalysts due to geometric and electronic effects.[8,19] Previously, Ag@Ni core-shell nanoparticles have been synthesized using a seed-growth method, and exhibited excellent catalytic activity for transfer hydrogenation reactions.[20] The inverse core-shell, Ni@Ag, nanoparticles are also expected to show higher catalytic performance in comparison with the monometallic Ag and Ni catalysts. However, to our knowledge, there is no report on improvement of Ag catalytic performance by Ni core. In this study, we synthesized supported Ni-Ag core-shell nanoparticles and investigated their catalytic activity for CO oxidation reaction which is known as a benchmark reaction for heterogeneous catalysts and as a practically important reaction for, e.g., purification of automobile exhaust gas and preferential oxidation (PROX) for polymer electrolyte fuel cell.[21,22]

1-2. Experimental and Results

We prepared SiO_2 (JRC-SIO-5 supplied from Catalysis Society of Japan) supported Ni@Ag catalysts by using a galvanic replacement reaction between Ni and Ag[23]: When Ni metal is exposed to Ag ion in a solution, Ni metal is oxidized to Ni ion and at the same time Ag ion is reduced to Ag metal because of a lower ionization tendency of Ag than Ni. SiO_2 supported Ni metal (denoted as Ni/SiO_2, 5wt%, 500 mg) was prepared by a conventional impregnation method[24] with O_2 treatment and subsequent H_2 reduction at 773 K. An aqueous solution of CH_3COOAg (0.02 mol L^{-1}, 11.6 mL) was added to an aqueous suspension of Ni/SiO_2 under N_2 at 281 K in an ice bath. After stirring for 15 min, the suspension was filtered, and the residue was washed with water and dried at 353 K for 12 h. The

loading amounts of Ag and Ni determined by inductively-coupled plasma (ICP) spectroscopy (Thermo Jarrel Ash IRIS/AP) were 1wt% and 2.4wt%, respectively. The Ag loading amount (1wt%, 0.046 mmol) was not consistent with the loss of Ni metal (2.6wt%, 0.22 mmol). It is likely that Ag and Ni was eluted as metal and/or metal oxide clusters formed in the replacement reaction. The resulting catalyst is denoted as Ni(2.4)@Ag(1.0)-281K.

Figure 1(a) shows the X-ray diffraction (XRD) of Ni(2.4)@Ag(1.0)-281K. The XRD analysis indicated that Ni(2.4)@Ag(1.0)-281K has Ag and Ni metals. The structure of Ni(2.4)@Ag(1.0)-281K was observed by using high angle annular dark field scanning transmission electron microscopy (HAADF-STEM) and energy dispersive X-ray spectroscopy (EDS) on a JEOL-200kV Cs-corrected S/TEM (Figure 2). Ni(2.4)@Ag(1.0)-281K showed Ag nanoparticles formed on Ni. In addition to the Ag nanoparticles, the EDS map exhibited some dispersed Ag on Ni, which was not distinguished as particles on the HAADF-STEM image. On the other areas, almost all of Ag species were observed on Ni with particle or dispersed form. The data suggest that the galvanic replacement method is effective for deposition of Ag on Ni; however, in this condition, Ag was not well-dispersed on Ni and it covered only a part of Ni particle surface.

In order to control the Ag deposition on Ni, the galvanic replacement reaction was carried out at much lower temperature than 281 K: An ethanol solution of $AgNO_3$ was added to an ethanol suspension of Ni/SiO_2 at 213 K controlled by using a dry ice/acetone cooling bath; the mixture was stirred for 15 min, filtered, and then washed with ethanol. The metal loadings of the resulting catalyst determined by means of ICP spectroscopy were 0.3wt% Ag and 3.0wt% Ni. The relative loading of Ag is smaller than that of Ni(2.4)@Ag(1.0)-281K. This result suggests the milder reduction of Ag under the low reaction temperature. The prepared catalyst is denoted as Ni(3.0)@Ag(0.3)-213K.

Figure 1 shows the XRD of Ni(3.0)@Ag(0.3)-213K recorded on a Rigaku MiniFlex II/AP diffractometer with Cu Kα radiation. The XRD of Ni(3.0)@Ag(0.3)-213K indicated the formation of Ni and Ag metals. Thus, Ag-Ni bimetal catalyst was prepared by the galvanic replacement reaction at the low temperature. The intensity XRD line derived from Ag metal of Ni(3.0)@Ag(0.3)-213K was much smaller than that of Ni(2.4)@Ag(1.0)-281K due to small Ag loading amount of Ni(3.0)@Ag(0.3)-213K, and possibly due to the formation of smaller Ag nanoparticles or thinner Ag layer on Ni(2.4)@Ag(1.0)-213K than on Ni(2.4)@Ag(1.0)-213K.

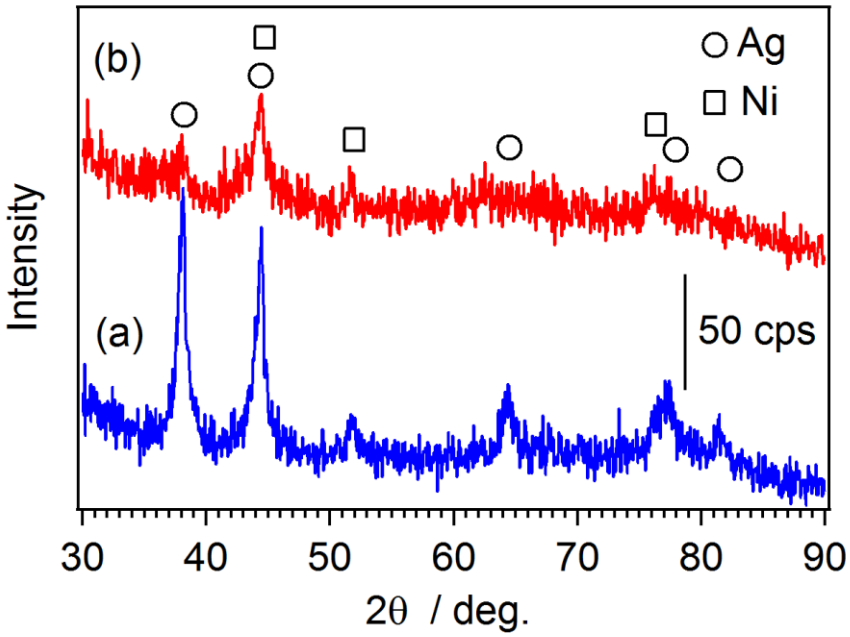

Figure 1. The XRD of (a) Ni(2.4)@Ag(1.0)-281K and (b) Ni(3.0)@Ag(0.3)-213K.

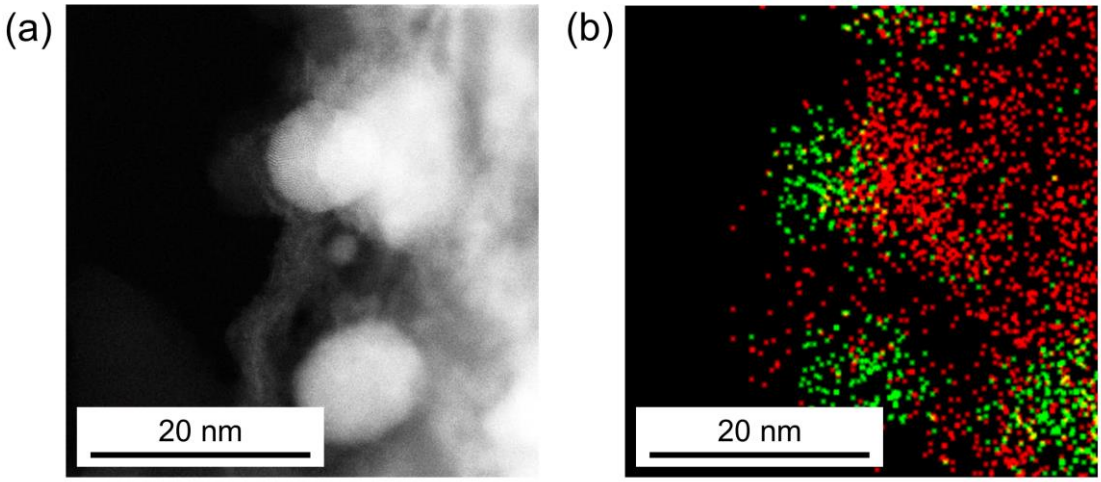

Figure 2. (a) A typical HAADF-STEM image and (b) an EDS elemental map of Ni(2.4)@Ag(1.0)-213K (Ag: green; Ni: red).

The structure of Ni(3.0)@Ag(0.3)-213K was investigated using the HAADF-STEM and EDS. A low magnification STEM observation indicated the formation of Ni and Ag particles on SiO_2 (Figure 3). Figure 4 exhibits the high magnification HAADF-STEM image and EDS map (Ag and Ni) of Ni(3.0)@Ag(0.3)-213K. The EDS mapping analysis indicated that Ag covers much larger area of Ni particle surface in comparison with Ni(2.4)@Ag(1.0)-281K. Thus, Ni@Ag core-shell nanoparticles were successfully prepared. The slow galvanic replacement reaction at low temperature would permit homogeneous reaction between Ag ion and Ni metal on its particle surface.

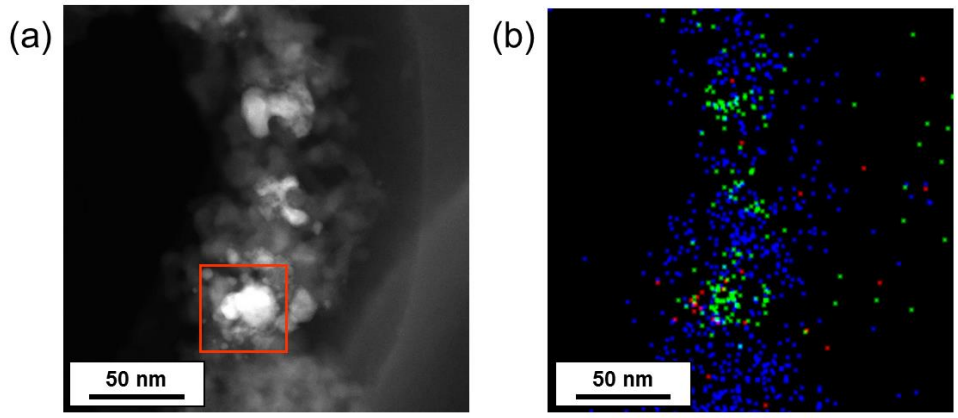

Figure 3. (a) A typical low magnification HAADF-STEM image and (b) an EDS elemental map of Ni(2.4)@Ag(0.3)-213K (Ag: green; Ni: red; Si: blue). The red square indicates the area of Figure 4.

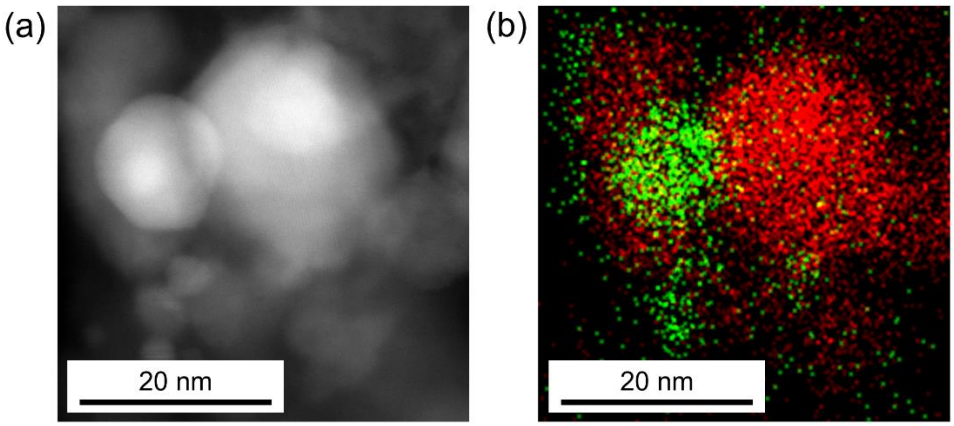

Figure 4. (a) A typical HAADF-STEM image and (b) an EDS elemental map of Ni(3.0)@Ag(0.3)-213K (Ag: green; Ni: red).

CO oxidation reaction was carried out using Ni(3.0)@Ag(0.3)-213K showing core-shell structure. As reference catalysts, we prepared SiO_2 supported Ag and Ni monometallic catalysts with 0.3wt% Ag loading and 3.0wt% Ni loading by a conventional impregnation method (denoted as Ag(0.3) and Ni(3.0), respectively), and also prepared SiO_2 supported Ag-Ni bimetallic catalyst with 0.3wt% Ag and 3.0wt% Ni loading by a co-impregnation method (denoted as Ag(0.3)Ni(3.0)). The metal loadings of the reference catalysts were adjusted to those of Ni(3.0)@Ag(0.3)-213K. Before the catalytic CO oxidation reaction, the catalysts were pretreated at 773 K for 10 min under 10%O_2/N_2 with a total flow rate of 100 cm^3 min^{-1}, and reduced in a flow of 3%H_2/N_2 at 773 K for 10 min. The CO oxidation was performed using a conventional fixed-bed flow reactor at atmospheric pressure with 10 mg of catalyst inside a Pyrex glass tube under a flow of 0.4% CO/10% O_2/He with a total flow rate of 100 cm^3 min^{-1}. The effluent gas was analyzed during stepwise increase in the reaction temperature, and the steady state CO conversion was measured after 10min for each temperature using

nondispersive infrared (NDIR) CO/CO_2 analyzer (Horiba VIA510).

Figure 5 shows the conversion of CO over Ni(3.0)@Ag(0.3)-213K together with those over Ag(0.3), Ni(3.0), and Ag(0.3)Ni(3.0) for comparison. The temperature at 50% CO conversion (so-called light-off temperature) over Ni(3.0)@Ag(0.3)-213K was ca. 425 K, and the CO conversion reached to 100 % at ca. 480 K. The both temperatures were lower than Ag(0.3) and Ni(3.0). Thus, Ni(3.0)@Ag(0.3)-213K with Ni@Ag core-shell structure has higher catalytic activity for CO oxidation than the monometallic catalysts. It should be noted that Ni(3.0) showed negligible CO oxidation activity below 480 K, and Ag(0.3) showed much higher catalytic activity than Ni(3.0). The result indicates that the active species of Ni(3.0)@Ag(0.3)-213K for the CO oxidation is not the bare Ni surface, but the surface of Ag shell. In comparison with Ag(0.3)Ni(3.0), Ni(3.0)@Ag(0.3)-213K also showed higher catalytic activity. It is suggested that Ni@Ag core-shell nanoparticles had higher catalytic activity for CO oxidation than individual Ag and Ni particles. The electron transfer from Ni core to Ag shell would enhance the catalytic activity of Ag for CO oxidation.[8,10,11] The origin of the high catalytic activity of Ni@Ag core-shell structure is now under investigation using spectroscopies and quantum chemical calculations.

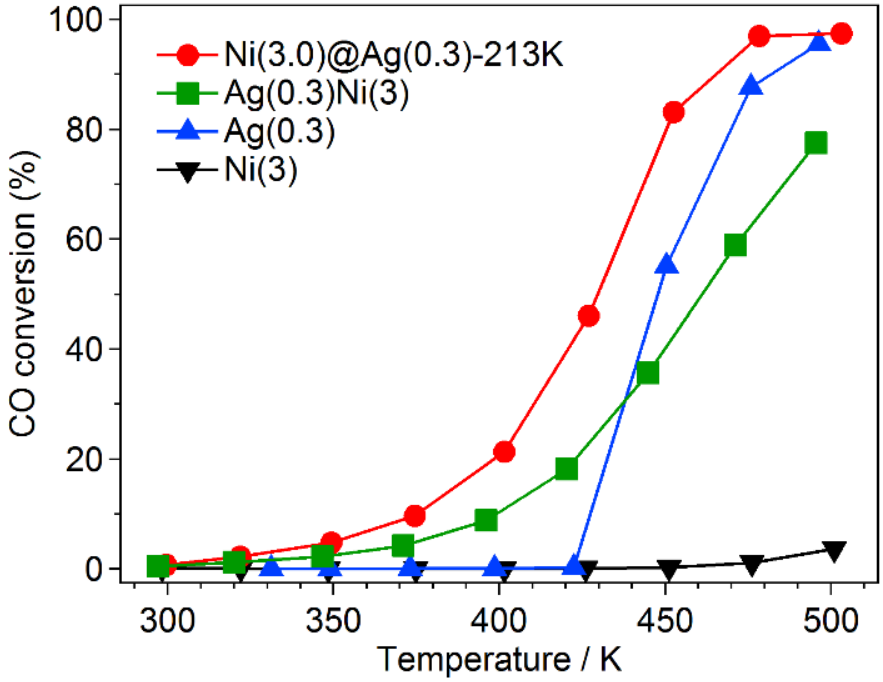

Figure 5. Conversion of CO into CO_2 over Ni(3.0)@Ag(0.3)-213K (●), Ag(0.3) (▲), Ni(3) (▼), and Ag(0.3)Ni(3) (■) as a function of temperature.

1-3. Conclusion

Ni@Ag core-shell nanoparticles supported on SiO_2 were prepared using a galvanic replacement reaction between Ni and Ag. The Ni@Ag core-shell catalyst showed higher catalytic activity for CO oxidation than Ag and Ni monometallic catalysts as well as than Ni-Ag bimetallic catalyst prepared by a conventional impregnation method.

1-4. References

1 Bhasin, M., McCain, J., Vora, B., Imai, T. & Pujado, P. *Appl. Catal., A* **221**, 397-419, (2001).

2 Blaser, H. U. *et al. Adv. Synth. Catal.* **345**, 103-151, (2003).

3 Gandhi, H. S., Graham, G. W. & McCabe, R. W. *J. Catal.* **216**, 433-442, (2003).

4 Toshima, N. & Yonezawa, T. *New J. Chem.* **22**, 1179-1201, (1998).

5 Guczi, L. *J. Mol. Catal. A: Chem.* **204-205**, 545-552, (2003).

6 Hou, W., Dehm, N. & Scott, R. *J. Catal.* **253**, 22-27, (2008).

7 Gao, F., Wang, Y. & Goodman, D. W. *J. Am. Chem. Soc.* **131**, 5734-5735, (2009).

8 Zhang, H., Watanabe, T., Okumura, M., Haruta, M. & Toshima, N. *Nat Mater* **11**, 49-52, (2011).

9 Negishi, Y., Munakata, K., Ohgake, W. & Nobusada, K. *J. Phys. Chem. Lett.* **3**, 2209-2214, (2012).

10 Nishimura, S., Yakita, Y., Katayama, M., Higashimine, K. & Ebitani, K. *Catal. Sci. Technol.* **3**, 351-359, (2013).

11 Yamazoe, S., Koyasu, K. & Tsukuda, T. *Accounts Chem. Res.* **47**, 816-824, (2014).

12 Brett, G. L. *et al. Angew. Chem. Int. Ed.* **50**, 10136-10139, (2011).

13 Qian, H. *et al. J. Am. Chem. Soc.* **134**, 16159-16162, (2012).

14 Rapallo, A. *et al. J. Chem. Phys.* **122**, (2005).

15 Zhang, Z., Nenoff, T. M., Huang, J. Y., Berry, D. T. & Provencio, P. P. *J. Phys. Chem. C* **113**, 1155-1159, (2009).

16 Xiao, Q. *et al. Thin Solid Films* **519**, 7116-7119, (2011).

17 Takahashi, A., Hamakawa, N., Nakamura, I. & Fujitani, T. *Appl. Catal., A* **294**, 34-39, (2005).

18 Wojcieszak, R., Monteverdi, S., Ghanbaja, J. & Bettahar, M. M. *J. Colloid Interface Sci.* **317**, 166-174, (2008).

19 Wang, X. *et al. J. Am. Chem. Soc.* **135**, 5938-5941, (2013).

20 Gawande, M. B. *et al. RSC Adv.* **3**, 1050-1054, (2013).

21 Kahlich, M., Gasteiger, H. & Behm, R. *J. Catal.* **171**, 93-105, (1997).

22 Shimizu, K. i., Sawabe, K. & Satsuma, A. *ChemCatChem* **3**, 1290-1293, (2011).

23 Zhang, J. *et al. J. Phys. Chem. B* **109**, 22701-22704, (2005).

24 Shimizu, K., Nishimura, M. & Satsuma, A. *ChemCatChem* **1**, 497-503, (2009).

Chapter 2
Ag–M (M: Ni, Co, Cu, Fe) bimetal catalysts prepared by galvanic deposition method for CO oxidation

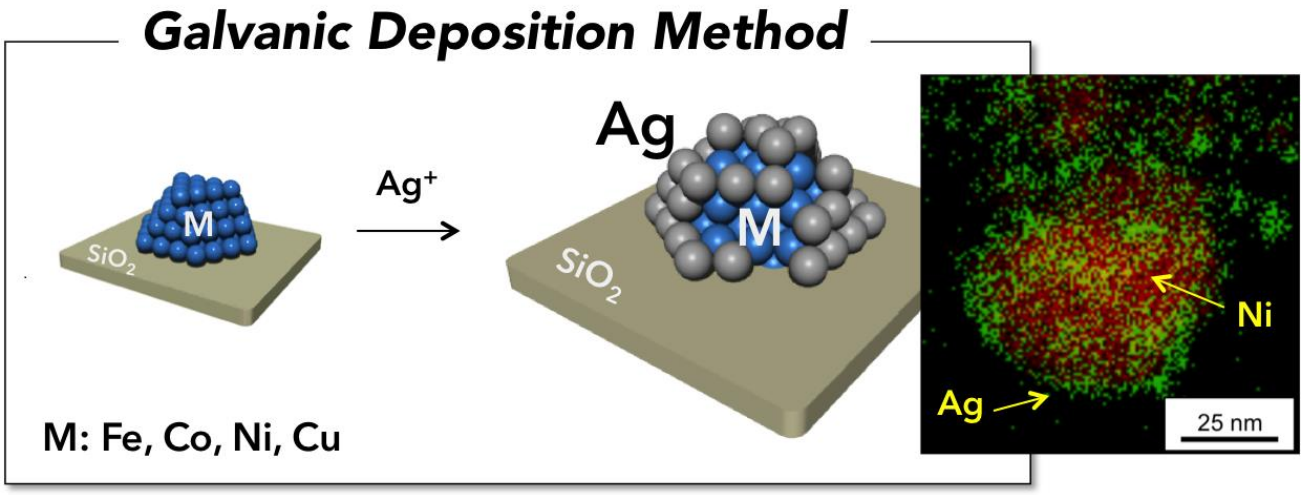

Ag-M (M: Fe, Co, Ni, Cu) bimetal catalysts supported on SiO_2 were prepared by galvanic deposition (GD) method. HAADF-STEM observation and EDX elemental mapping showed that Ag was successfully introduced on Fe, Co, Ni, and Cu particles using the GD method. Ag-Fe, Ag-Co, and Ag-Cu catalysts showed Janus structure that is Ag nanoparticles (NPs) on the 3d metals. On the other hand, Ag-Ni catalyst showed core-shell like structure composed of small Ag NPs (<10 nm) or thin layer on Ni particles. The catalytic activities of Ag-M bimetal catalysts were evaluated by CO oxidation reaction. All Ag-M bimetal catalysts showed higher catalytic activities than Fe, Co, Ni, Cu, and Ag mono-metal catalysts. In particular, Ag-Ni bimetal catalyst having core-shell like structure showed remarkable enhancement of the catalytic activity.

Contents

2-1. Introduction

Platinum-group metals (PGMs) are essential components of catalysts for various industrial processes including petroleum chemistry, synthesis of fine chemicals, and purification of exhaust gases from plant and automobile.[1-3] However, PGMs are expensive and scarce resources. Therefore, alternatives to PGM catalysts are increasingly required.

To design PGM-free catalysts, the d-band theory by Nørskov et al. is useful, because the theory provides a correlation between the d-band center of transition metal surfaces and its catalytic activity.[4,5] For example, catalytic activity for oxygen reduction reaction shows a volcano-type dependency on the d-band-center of the metal catalysts.[6] Thus, the first step to design the PGM-free catalysts as alternatives of the PGM ones is to investigate the correlation between the catalytic activity of the PGM-free catalysts and their modification which will cause the shift of the d-band center. Bimetallization is one of the strategies to control the d-band-center of catalyst surface.[5,7-9] It has been reported that the d-band-center of bimetal catalysts could be changed by the ligand effect and strain effect.[8,10,11] In general, d-bands of coinage metals such as Ag reside below the Fermi level in a bulk state,[12] and their bulk metals are usually catalytically poor (except for ethylene oxidation in the case of Ag [13]). On the other hand, d-bands of 3d transition metals such as Fe, Co, Ni, and Cu reside above the Fermi level and the position of their d-band center is in order.[5] The combination of the coinage metals with the above 3d metals may lead to the gradual shift of the d-band center and change the catalytic activity according to their shift.

Preparation methods of bimetal catalysts have been developed.[14] A galvanic deposition (GD) method is one of the preparation methods of bimetal catalysts.[15-17] In a GD process, a supported metal X is replaced by another metal Y precursor having lower ionization tendency through galvanic reaction. Recently, we have prepared SiO_2 supported Ag-Ni bimetal catalysts using a GD method.[18] The AgNi catalysts showed higher catalytic activity for CO oxidation than Ag and AgNi catalysts prepared by a conventional impregnation method. In the present study, bimetal catalysts of Ag and various 3d transition metals (Fe, Co, Ni, and Cu) were prepared by a GD method, and their catalytic activity for CO oxidation reaction was evaluated to investigate the effect of bimetallization of Ag and 3d transition metals.

2-2. Experimental

Catalysts preparation

$AgNO_3$, $Ni(NO_3)_2{\cdot}6H_2O$, $Co(NO_3)_2{\cdot}6H_2O$, $Fe(NO_3)_3{\cdot}9H_2O$, $Cu(NO_3)_2{\cdot}3H_2O$ as the metal precursor were purchased by Kishida Chemicals (99.8%, pure). SiO_2 (JRC-SIO-5) as a support was supplied from the Catalysis Society of Japan.

Ni/SiO_2 with 5 wt% of Ni loading was prepared by a conventional impregnation method. Silica as a support was added to aqueous solution of $Ni(NO_3)_2$, and the mixture was stirred. After evaporating and drying overnight at 80 ˚C, the resulting solid was calcined at 500 ˚C for 3 h. Fe/SiO_2, Co/SiO_2, and Cu/SiO_2 (5 wt% of metal loading) were also prepared in a similar manner (denoted as Fe-**I**, Co-**I**,

Ni-**I**, Cu-**I**, respectively).

Galvanic deposition (GD) method was carried as reported previously.[18] We added Ni/SiO_2 to two-neck round-bottom flask, and capped by a septum. Ni/SiO_2 was reduced under a flow of H_2 at 400 ˚C for 30 min. After N_2 substitution, the two-neck round-bottom flask with Ni catalyst was cooled with dry ice below −60 ˚C. We added ethanol into the flask, and dropped the aqueous $AgNO_3$ solution in ethanol into the flask for 1 h. The obtained solid was centrifuged and dried overnight at 80 ˚C. The obtained AgNi bimetal catalyst was denoted as AgNi-**GD**. AgFe, AgCo, and AgCu bimetal catalysts were similarly prepared by GD method (denoted as AgFe-**GD**, AgCo-**GD**, and AgCu-**GD**, respectively). Fe/SiO_2, Co/SiO_2, and Cu/SiO_2 were reduced at 600 ˚C, 500 ˚C, and 300 ˚C, at which the reduction of 3d transition metals to zero-valent was completed. Metal loadings of these catalysts were determined by inductively coupled plasma (ICP) analysis of the filtrate obtained during the centrifugation. All catalysts were listed in Table 1.

Table 1. The features of catalysts prepared. All catalysts supported on SiO_2.

Catalyst	Preparation method	Reduction temperature for GD method[a]	Metal loadings (wt%)[b]
Fe-**I**	Impregnation method	-	Fe=5.0
Co-**I**	Impregnation method	-	Co=5.0
Ni-**I**	Impregnation method	-	Ni=5.0
Cu-**I**	Impregnation method	-	Cu=5.0
AgFe-**GD**	GD method	600	Ag=1.5, Fe=4.7[b]
AgCo-**GD**	GD method	500	Ag=2.9, Co=4.4[b]
AgNi-**GD**	GD method	400	Ag=0.3, Ni=3.0[b]
AgCu-**GD**	GD method	300	Ag=2.3, Cu=4.9[b]

a Reduction temperature at which 3d transition elements are completely reduced to metal state was decided using H_2-TPR.

b metal loading was measured by ICP analysis.

Characterization

ICP analysis was carried out to determine metal loading of bimetal catalysts prepared by GD method using IRIS-AP (Thermo Fisher scientific).

High angle annular dark field scanning transmission electron microscopy (HAADF-STEM) and energy dispersive X-ray spectroscopy (EDX) analyses were performed on JEM-2100F (JEOL, Japan) operated at 200 kV accelerating voltage. Samples for TEM observations were directly supported on a Mo mesh with a carbon microgrid after CO oxidation reaction.

The Ag K-edge (25514 eV) X-ray absorption fine structure (XAFS) measurement was carried out at BL01B1 of SPring-8 (Hyogo, Japan). The XAFS spectra at Ag K-edge were measured using a Si(111) double-crystal monochromator in transmission mode. The catalysts after using CO oxidation

were measured without exposure to air. A typical data reduction (e.g., background removal, or normalization) was carried out with the Athena included in the Demeter package. The curve-fitting analysis of the EXAFS spectra was performed for the inverse Fourier transforms on the Ag-Ag shell using theoretical parameters calculated by FEFF6. The Ag K-edge EXAFS data were fitted between 3 and 12 $Å^{-1}$ in *k* space and 1-3 Å in *R* space including the first Ag-Ag shell.

Catalytic activity test

CO oxidation was performed using a conventional flow reactor at atmospheric pressure. The catalysts were fixed in a Pyrex tube with internal diameter of 4 mm. Before the catalytic run, a catalyst was oxidized in a flow of 10% O_2/N_2 for 10 min and then reduced in a flow of 3% H_2/N_2 for 10 min at 500 ˚C. The reaction gas of CO oxidation was 0.4% CO/10% O_2/N_2, and total gas flow was 100 mL/min at a space velocity of 600,000 mL h^{-1} g^{-1}. The effluent gas was analyzed by nondispersive infrared CO/CO_2 analyzer (Horiba VIA510, Japan). The concentrations of CO and CO_2 were measured during stepwise increase in the reaction temperature from 25 ˚C to 250 ˚C, and the steady state CO conversion was measured after 30 min for each temperature. T_{50} was defined as the temperature of 50% conversion for CO oxidation.

Density functional theory (DFT) calculation

Spin-polarized DFT calculations were performed using the plane-wave pseudopotential approach in the PWscf code of Quantum Espresso (QE) package.[19] GGA-PBE approximation was adopted. The energy cutoff of 30 Ry and Monkhorst-Pack mesh of 2×2×1 k-points were used. Ni(111) and Ag(111) surfaces were modeled using (5×5) or (6×6) unit cells consisting of three atomic layers, and the structures of Ag/Ni(111) were calculated by placing Ag adlayer on Ni(111) and Ag(111), respectively. A vacuum gap was set to ~ 13 Å. In these calculations, the most bottom layer was fixed and the coordinates of other atoms were relaxed.

2-3. Results and Discussions

HAADF-STEM and EDX analysis

HAADF-STEM images and EDX elements mapping for the catalysts prepared by the GD method were shown in Figure 1. AgNPs were observed adjacent to Fe, Co, Ni, and Cu particles, indicating that Ag NPs were successfully introduced on the 3d metal particles by the GD method. The metal loadings were confirmed by ICP analysis as shown in Table 1. The loadings of Fe, Co, Ni, and Cu on Ag-M bimetal catalysts were less than 5 wt% of M/SiO_2. The decrease in the 3d transition metals and the deposition of Ag suggested that the replacement between 3d transition metals and Ag was occurred through galvanic reaction.

On AgCo-**GD**, Ag NPs with the diameter of 50-100 nm were present on Co particles (Figure 1(a)). In the case of AgFe-**GD** and AgCu-**GD**, Ag NPs having diameter about 50 nm were dispersed on Fe and Cu particles (Figure 1(b), (c)). As for AgNi-**GD**, the diameters of Ag NPs were 5-10 nm,

which were the smallest among Ag NPs of Ag-M bimetal catalysts (Figure 1(d)). Therefore, the size of Ag NPs increased in the order of AgNi-**GD** < AgCu-**GD** < AgFe-**GD** < AgCo-**GD**.

The magnified HAADF-STEM image and EDX elements mapping of AgNi-**GD** were shown in Figure 1(e). Interestingly, Ag formed thin shell structures over Ni particles. On the other hand, AgFe-**GD**, AgCo-**GD**, and AgCu-**GD** did not have Ag thin shell structure on the 3d metals. The morphology of AgCu, AgCo, and AgNi have been theoretically studied. [20-22] These studies indicated that the structural property of nanoalloys of weakly miscible metals is expected to present phase-separated arrangements of their components, such as core-shell and Janus arrangement. Our experimental results agree with these theoretical studies.

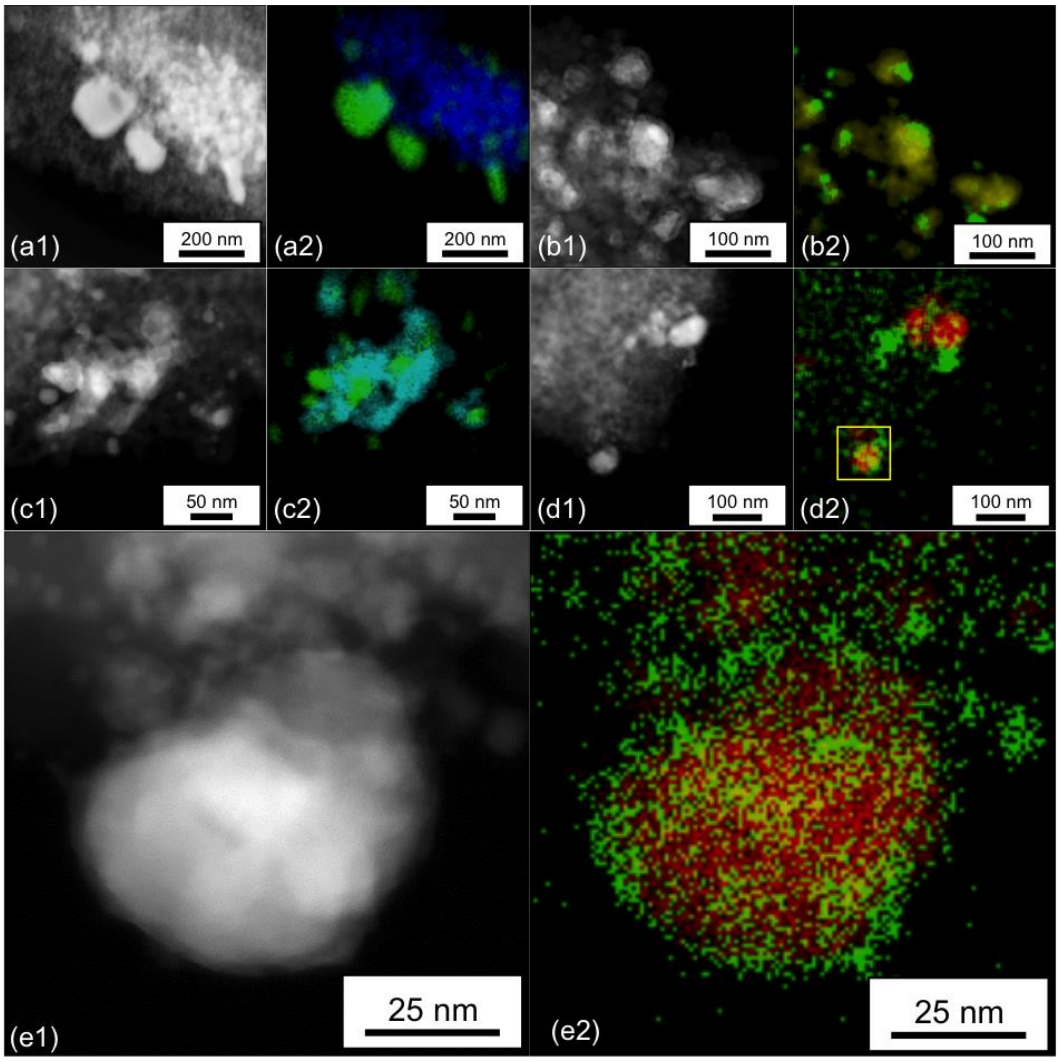

Figure 1. HAADF-STEM image and EDX elements mapping of AgCo-**GD** (a1, a2), AgFe-**GD** (b1, b2), AgCu-**GD** (c1, c2) and AgNi-**GD** (d1, d2). (e1, e2) are enlarged images of yellow square of (d2). The green, blue, yellow, cyan, and red colors in EDX mapping correspond to Ag, Co, Fe, Cu, and Ni elements respectively.

XAFS spectroscopy

The k^3-weighted Ag K-edge EXAFS spectra of AgFe-**GD**, AgCo-**GD**, AgNi-**GD**, AgCu-**GD** and Ag foil as a reference sample were shown in Figure 2(A). Since the Ag K-edge EXAFS oscillation patterns of all bimetal catalysts are well consistent with that of Ag foil, Ag specie is considered to be in metallic state without Ag-M alloying. This is in accordance with the report that AgFe, AgCo, AgNi, and AgCu alloys are usually immiscible in the bulk phase due to the large lattice mismatch as well as difference in surface energies and cohesions between the metals. [22,23]

The Fourier transformed k^3-weighted Ag K-edge EXAFS for Ag-M bimetal catalysts were shown in Figure 2(B). To evaluate the structural parameters of Ag, the curve-fitting analysis on the Ag K-edge EXAFS spectra was carried out. The results were shown in Table 2. From the Ag-Ag *C. N.*, the particle size was calculated assuming that all Ag species form cuboctahedral structure. The particle size increased in the order of AgNi-**GD** < AgCu-**GD** < AgFe-**GD** < AgCo-**GD**, which agrees with that of the STEM observation. (The difference of the size of Ag NPs between the EXAFS analysis and STEM observation may be due to the difference between the primary particles (EXAFS analysis) and the secondary particles (the STEM observation).) In the case of AgNi-**GD**, the STEM observation indicated that the Ag species also exist as thin shell (Figure 1(e)) on Ni particles. Since the ideal Ag monolayer and bilayer should have 6 and 9 of Ag-Ag *C.N.*, respectively, the Ag-Ag *C.N.* of AgNi-**GD** (6.9 ± 0.5) suggests that AgNi-**GD** have Ag mono-/bi-layer structure when we assume that all Ag species form thin shell. Therefore, we concluded that AgNi-**GD** has small Ag NPs (1.4 nm) or mono-/bi-layer on Ni particles.

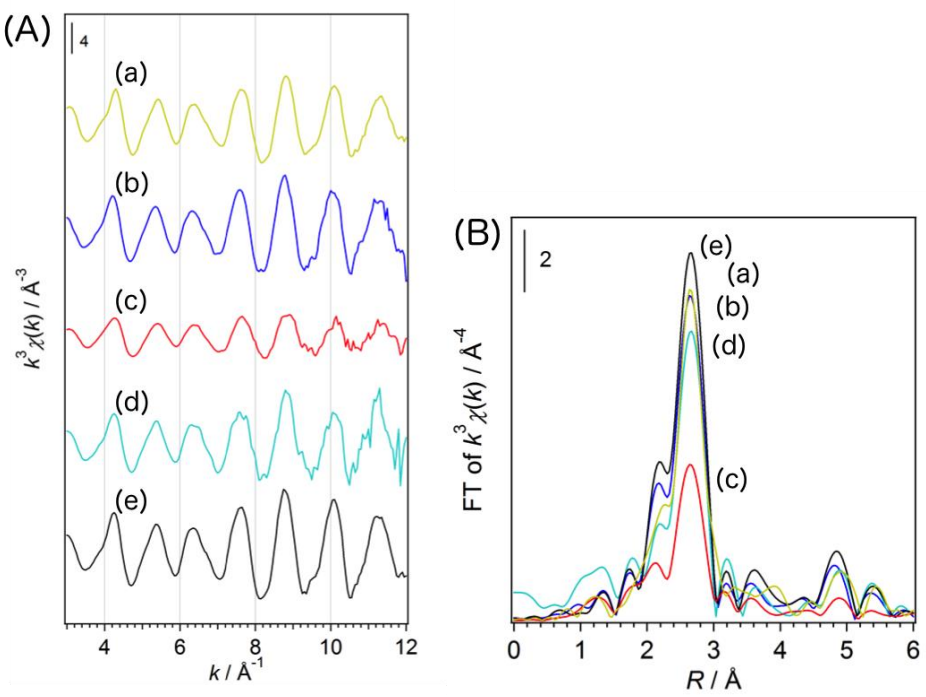

Figure 2. k^3-weighted Ag K-edge EXAFS spectra (left) and k^3-weighted Fourier transformed EXAFS spectra (right) for AgFe-**GD** (a, yellow), AgCo-**GD** (b, blue), AgNi-**GD** (c, red), AgCu-**GD** (d, cyan),

and Ag foil as a reference (e, black).

Table 2. Single scattering curve-fitting result of the Ag K-edge EXAFS spectra of Ag-M (M: Fe, Co, Ni, Cu) bimetal catalysts.

Catalyst	Shell	*C. N.*	*R*/ Å	$\sigma^2\times10^4$/ Å^2	ΔE_0/ eV	R_f/ %
AgNi-**GD**	Ag–Ag	6.9(5)	2.85	119(5)	−0.05	0.1
AgCu-**GD**	Ag–Ag	9.8(17)	2.89	100(11)	0.84	0.5
AgFe-**GD**	Ag–Ag	10.6(7)	2.86	103(4)	−0.04	0.1
AgCo-**GD**	Ag–Ag	11.1(7)	2.87	98(4)	−0.03	0.1

Catalytic activity

Figure 3 shows the results of catalytic test over the bimetal catalysts prepared by the GD method, together with those over the 3d mono-metal catalysts. The apparent catalytic activity of Ag-M bimetal catalysts was higher than the 3d metal catalysts. For comparison, the results of CO oxidation over Ag/SiO_2 with various Ag loadings are also shown in Figure 3. The catalytic activity of Ag mono-metal catalysts was higher than those of the 3d mono-metal catalysts. The result suggests that the Ag species on Ag-M bimetal catalysts mainly contributes to the CO oxidation. The apparent catalytic activity of Ag-M bimetal catalysts were compared to Ag/SiO_2 with similar Ag loading (cf. Table 1). As a result, AgNi-**GD** (0.3wt% Ag loading) presented much higher catalytic activity than 0.3 wt% Ag/SiO_2. On the other hand, AgCo-**GD**, AgCu-**GD**, and AgFe-**GD** (1.5-2.9 wt% Ag loadings) showed comparable or lower apparent catalytic activity than 1 and 5 wt% Ag/SiO_2.

To investigate the effect of the 3d metals on the catalytic activity of Ag in more detail, we evaluated turnover frequency (TOF) of CO oxidation over the bimetal catalysts. The TOF was calculated from the surface Ag atoms and the CO conversion at 125 °C where the contribution of the CO oxidation over the 3d metal surface is small (Figure 3): TOF = [(moles of CO reacted per hour)/(moles of surface Ag atom)]. The amount of surface Ag atoms was evaluated using Ag-Ag *C. N.*, assuming that the all Ag atoms formed NPs or mono-/bi-layer. Table 3 lists the TOFs of Ag-M catalysts and 1 wt% Ag/SiO_2 as a reference. All Ag-M catalysts showed higher TOFs than 1 wt% Ag/SiO_2, and AgNi-**GD** was especially high TOF even if we assumed Ag mono-/bi-layer. The results suggest that the catalytic activity of Ag is enhanced by contact with the 3d metals, in particular with Ni.

It has been suggested that the d-band-center of clean Ag surface shift by neighboring 3d transition metals such as Fe, Co, Ni, and Cu. The shift of the Ag d-band can change the adsorption energies of the reactants, and enhance the catalytic activity. It has been also reported that such change of electronic state mainly occurs at junction of two metal species. On the basis of these literature,[7,8] Ag monolayer or the perimeter of Ag NPs on a 3d metal can have different electronic state from a Ag mono-metal catalyst. As above, AgNi-**GD** showed small Ag NPs having large perimeter or mono-/bi-layer structure. Therefore, it is likely that the modification of Ag d-band is the reason for the enhanced

TOF of AgNi-**GD**.

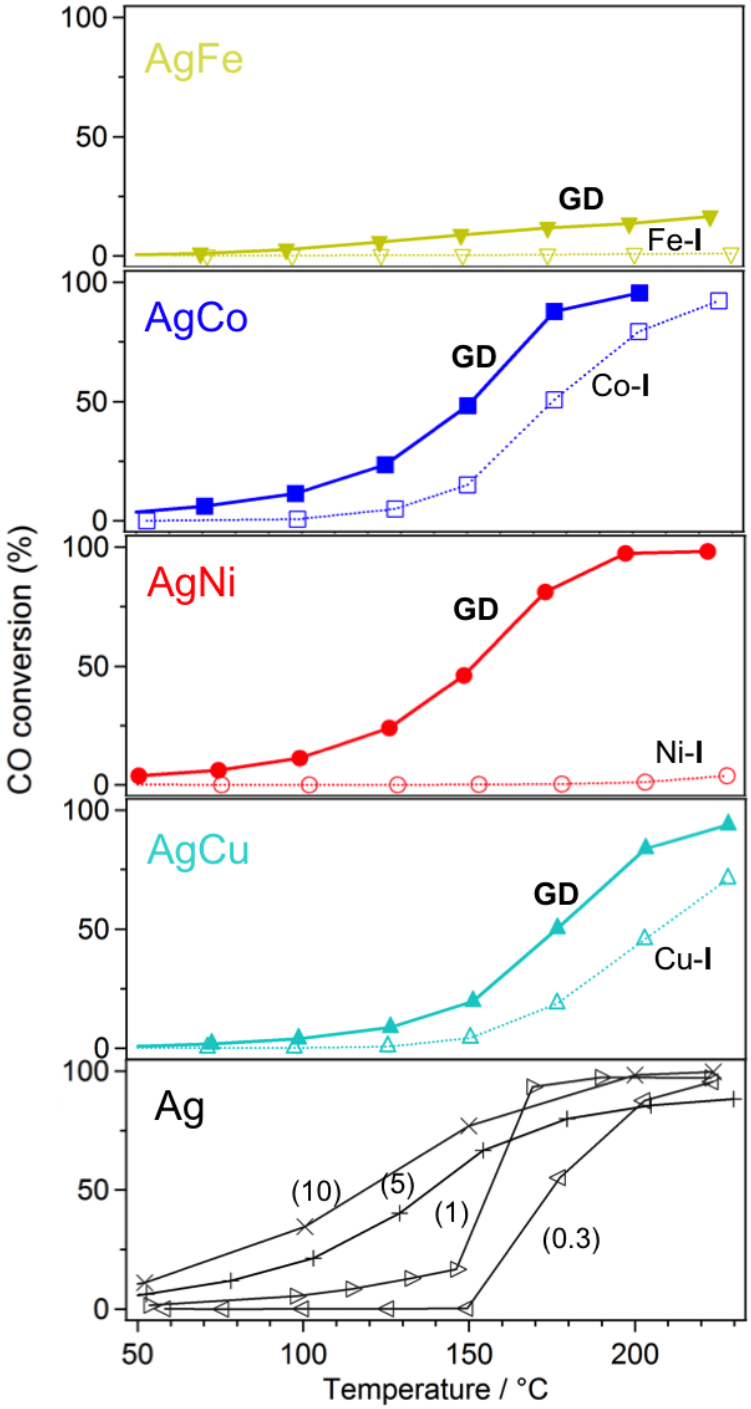

Figure 3. Results of catalytic activity for CO oxidation reaction using AgFe-**GD** (▼, yellow solid line), Fe-**I** (▽, yellow dotted line), AgCo-**GD** (■, blue solid line), Co-**I** (□, blue dotted line), AgNi-**GD** (●, red solid line), Ni-**I** (○, red dotted line), AgCu-**GD** (▲, cyan solid line), Cu-**I** (△, cyan dotted line), 0.3wt% Ag/SiO_2 (◁, black solid), 1wt% Ag/SiO_2 (▷, black solid), 5wt% Ag/SiO_2 (+, black solid), and 10wt% Ag/SiO_2 (╳, black solid).

Table 3. TOF value (h^{-1}) for Ag-M bimetal catalysts evaluated from Ag–Ag *C. N.* and reaction rate of CO oxidation.

Catalyst	*C. N.*	Morphology of Ag	$d_{Ag\text{-}C.N.}$ [a]/ nm	surface Ag atoms $\times 10^7$/ mol	CO conversion at 125 °C/ %	TOF[b]/ h^{-1}
		Two layers	-	1.4		1811
AgNi-**GD**	6.9±0.5	One layer	-	2.8	23.5	905
		NPs	1.4	2.0		1259
AgCu-**GD**	9.8±1.7	NPs	3.7	7.7	8.6	120
AgFe-**GD**	10.6±0.7	NPs	5.0	3.9	5.9	161
AgCo-**GD**	11.1±0.7	NPs	7.8	5.1	23.5	493
1 wt% Ag/SiO_2	2.6±0.5	NPs	0.7	8.8	11.1	135

a Evaluated from Ag–Ag shell coordination number assuming that all Ag NPs formed cuboctahedral structure.

b (Reaction rate of CO oxidation)/(moles of surface Ag atom).

DFT calculation

To make sure the influence of the bimetal effect between Ag ad Ni, DFT calculations wer carried out. Since the (111) plain is the most stable surface on Ni nanoparticle, Ni(111) slab was chosen as a model. To examine an adlayer structure of Ag/Ni(111), the possible structures of AgNi were calculated. Figure 4 shows a two-dimensional (2D) island, an atomic layer, and a 3D cluster with a Ag coverage of 0.25 ML using (5×5) Ni(111) unit cells. The stabilization energy per a Ag atom (E_{stab}) was calculated by

$$E_{stab} = \frac{E_{ads.system} - (E_{surf} + n \cdot E_{Ag\ atom})}{n}$$

where $E_{ads.system}$ is the energy of each optimized structure of the Ag_4/Ni(111); E_{surf} is the energy of Ni(111); $E_{Ag\ atom}$ is the energy of the isolated Ag atom; and n is the number of Ag. The calculated E_{stab} was listed in Table 4. Since the 2D island was the most stable for the adlayer structure and the energy difference is more than RT (~ 30 meV at 80 °C), Ag prefer to form a 2D layer structure.

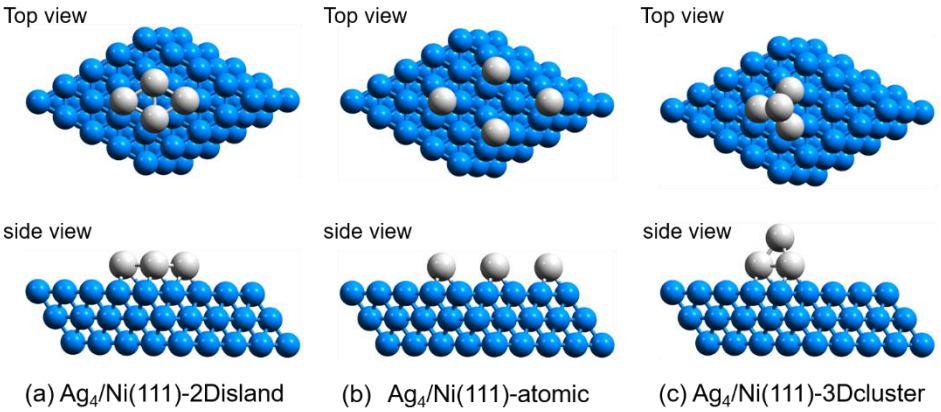

Figure 4. Optimized structure of the (a) 2D island, (b) atomic layer (c) 3D cluster Ag_4/Ni(111) (color scheme: blue-Ni; white-Ag).

Table 4. The stabilization energy of the series of Ag/Ni(111).

Structure	E_{stab} (eV)
Ag_4/Ni(111)-2Disland	−2.64
Ag_4/Ni(111)-atomic	−2.46
Ag_4/Ni(111)-3Dcluster	−2.48

Through above results, we calculated the 2D island Ag_{16} on (6×6) Ni(111) which is bigger than Ag_4/Ni(111). Figure 5 shows optimized structure of Ag_{16}/Ni(111) and Ag_{16}/Ag(111); the latter is a reference as Ag mono-metal surface. Density of states of d-band of surface Ag regarding Ag_{16}/Ni(111) and Ag_{16}/Ag(111) are displayed in Figure 6. The position and shape of d-bands were clearly different between Ag_{16}/Ni(111) and Ag_{16}/Ag(111). It is noted that there is a new band between −3 and −1 eV, which is close to Fermi level. Thus, d-band of Ag is modified by core-shell bimetallization. Estimated d-band centers (E_d) of Ag_{16}/Ni(111) and Ag_{16}/Ag(111) are listed in Table 5. E_d of Ag_{16}/Ni(111) is −3.94 eV, which is more close to Fermi level than E_d of Ag_{16}/Ag(111). The adsorption energy of the simple molecule adsorbed on the transition metal surface is predicted by the d-band center theory.[5,8] This theory suggests that if the d-band center of surface metal shifts to Fermi level, the adsorption of molecule is stronger. We calculated the adsorption energy of CO and O_2 on both surface of Ag_{16}/Ni(111) and Ag_{16}/Ag(111). The adsorption energy of CO (E_{CO}) and O_2 (E_{O_2}) were difined by

$$E_{CO} = E_{CO+surf} - (E_{CO\ mol.} + E_{surf})$$

$$E_{O_2} = E_{O_2+surf} - (E_{O_2\ mol.} + E_{surf})$$

where $E_{CO+surf}$ and E_{O_2+surf} are the energy of each surface after adsorption of CO and O_2; $E_{CO\ mol.}$ and $E_{O_2\ mol.}$ are the energy of CO and O_2 molecules; E_{surf} is the energy of each surface. The calculated E_{CO} and E_{O_2} are listed in Table 5. The absolute values of adsorption energy for

Ag_{16}/Ni(111) were larger than those for Ag_{16}/Ag(111) in the both case of CO and O_2. These results suggest the adsorption of molecule is increased by the modification of d-band of Ag.

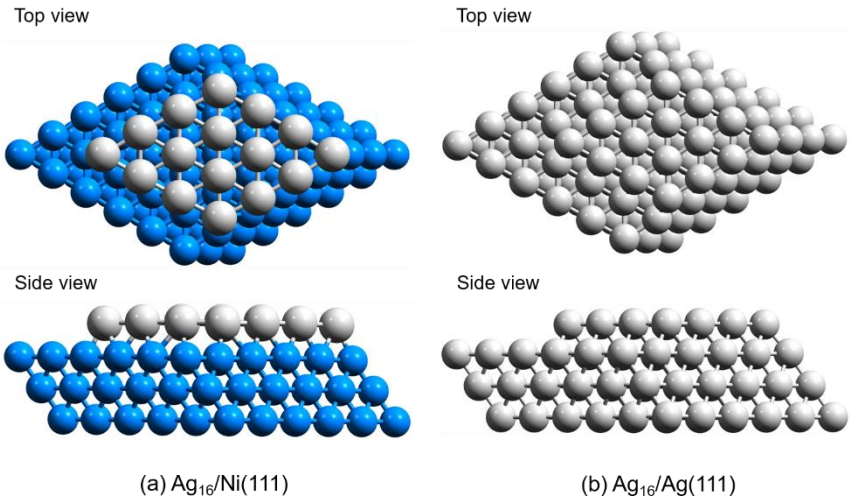

Figure 5. Optimized structure of the (a) Ag_{16}/Ni(111) and (b) Ag_{16}/Ag(111) (color scheme: blue-Ni; white-Ag).

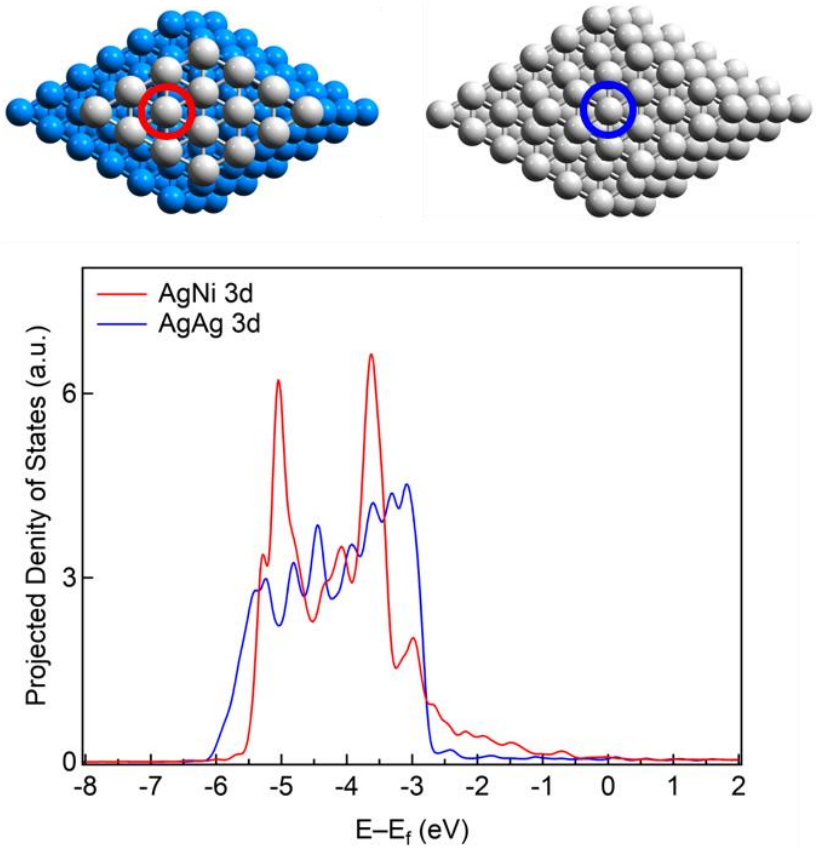

Figure 6. Projected density of states for Ag 4d on Ag_{16}/Ni(111) (red) and (b) Ag_{16}/Ag(111) (blue).

Table 5. The d-band center (E_d) of the surface Ag atom, the adsorption energy of CO and O_2 on surface Ag for Ag_{16}/Ni(111) and Ag_{16}/Ag(111).

Structure	E_d (eV)	E_{CO} (eV)	E_{O_2} (eV)
Ag_{16}/Ni(111)	−3.82	−0.32	−0.24
Ag_{16}/Ag(111)	−3.92	−0.14	−0.14

2-4. Conclusion

Ag and 3d transition metals (Fe, Co, Ni, Cu) bimetal catalysts were prepared using the galvanic deposition method. The HAADF-STEM observation and EDX elements mapping showed that Ag was completely introduced on 3d transition metals using the GD method. In particular, AgNi-**GD** formed Ni-Ag core-shell like structure with small Ag NPs (1.4 nm) or Ag mono-/bi-layer. The Ag-M bimetal catalysts exhibited higher catalytic activity for CO oxidation compared to the Ag, Fe, Co, Ni, and Cu mono-metal catalysts. AgNi-**GD** showed especially excellent activity and TOF. DFT calculation revealed that density of states of Ag were shifted to Fermi level by contact with Ni(111). These results suggest that small Ag NPs or thin Ag shell structure on 3d transition metals strongly enhances adsorption of molecule, likely due to the modification of Ag electronic state by adjacent 3d metals.

2-5. References

1 Bhasin, M., McCain, J., Vora, B., Imai, T. & Pujado, P. *Appl. Catal., A* **221**, 397-419, (2001).

2 Blaser, H. U. *et al. Adv. Synth. Catal.* **345**, 103-151, (2003).

3 Gandhi, H. S., Graham, G. W. & McCabe, R. W. *J. Catal.* **216**, 433-442, (2003).

4 Pallassana, V., Neurock, M., Hansen, L. B., Hammer, B. & Nørskov, J. K. *Phys. Rev. B* **60**, 6146, (1999).

5 Hammer, B. & Nørskov, J. K. *Adv. Catal.* **45**, 71-129, (2000).

6 Lima, F. *et al. J. Phys. Chem. C* **111**, 404-410, (2007).

7 Ruban, A., Hammer, B., Stoltze, P., Skriver, H. L. & Nørskov, J. K. *J. Mol. Catal. A: Chem.* **115**, 421-429, (1997).

8 Greeley, J. & Nørskov, J. K. *Surf. Sci.* **592**, 104-111, (2005).

9 Zhang, J., Jin, H., Sullivan, M. B., Lim, F. C. & Wu, P. *Phys. Chem. Chem. Phys.* **11**, 1441-1446, (2009).

10 Ferrando, R., Jellinek, J. & Johnston, R. L. *Chem. Rev.* **108**, 845-910, (2008).

11 Xu, J. *et al. J. Am. Chem. Soc.* **132**, 10398-10406, (2010).

12 Peterson, A. A. *et al. Top. Catal.* **55**, 1276-1282, (2012).

13 Sharma, V. K., Yngard, R. A. & Lin, Y. *Adv. Colloid Interface Sci.* **145**, 83-96, (2009).

14 Torimoto, T. *et al. J. Mater. Chem. A* **3**, 6177-6186, (2015).

15 Zhang, H. *et al. J. Am. Chem. Soc.* **133**, 6078-6089, (2011).

16 Kim, K. W., Kim, S. M., Choi, S., Kim, J. & Lee, I. S. *ACS Nano* **6**, 5122-5129, (2012).

17 Pan, X., Zhang, Y., Miao, Z. & Yang, X. *J. Energy Chem.* **22**, 610-616, (2013).

18 Mahara, Y. *et al. Chem. Lett.* **43**, 910-912, (2014).

19 Giannozzi, P. *et al. Journal of physics: Condensed matter* **21**, 395502, (2009).

20 Langlois, C. *et al. Nanoscale* **4**, 3381-3388, (2012).

21 Bochicchio, D. & Ferrando, R. *Phys. Rev. B* **87**, (2013).

22 Ferrando, R. *J. Phys. Condens. Matter.* **27**, 013003, (2015).

23 Rapallo, A. *et al. J. Chem. Phys.* **122**, (2005).

Part II

Enhancement of the Reducibility of Metals for Oxidation Catalysts by Metal–Metal Oxide Interaction

Chapter 3
Enhanced activity for methane combustion over a $Pd/Co/Al_2O_3$ catalyst prepared by a galvanic deposition method

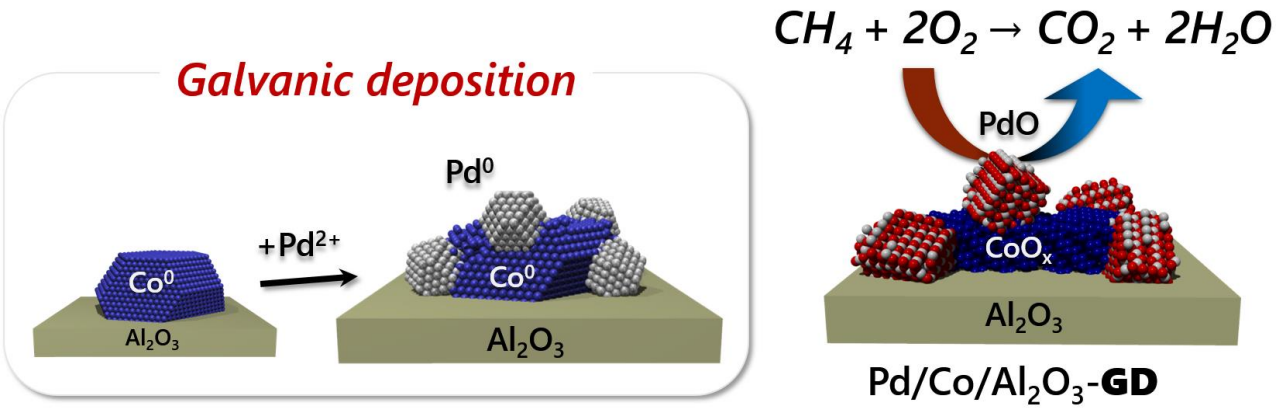

A $Pd/Co/Al_2O_3$ catalyst prepared by a galvanic deposition method exhibited notable catalytic activity for methane combustion, due to the higher reducibility of PdO nanoparticles on CoO_x.

Contents

3-1. Introduction

Methane combustion has become increasingly important as a method for emission reduction of automotive exhaust gases.[1-3] It is well-known that methane has a global warming potential 23 times higher than that of CO_2, therefore unburned methane should be oxidized to CO_2 and H_2O.

Supported palladium (Pd) catalysts are recently utilized for methane combustion.[4-30] In particular, alumina-supported Pd (Pd/Al_2O_3) catalyst has received special attention due to its high catalytic activity and thermal stability. However, their catalytic activities are still insufficient at lower temperature. To obtain catalysts with higher activity, the additive effect into Pd/Al_2O_3 has been investigated. *Widjaja* and co-workers examined MOx (M=Co, Cr, Cu, Fe, Mn and Ni) promoted Pd/Al_2O_3 catalysts and reported that Ni and Co were effective for promotion of methane combustion.[8] Liu and co-worker investigated the effect of metal oxides on Pd/Al_2O_3 catalysts and the formation of the $NiAl_2O_4$ and $MgAl_2O_4$ spinel phase would be beneficial for the methane catalytic performance.[31,32] Recently, *Cargnello et al.* reported that Pd core and CeO_2 shell deposited onto modified hydrophobic alumina displayed high methane combustion activity due to an increase of metal-support interface.[20] To improve the catalytic performance of Pd/Al_2O_3, it is crucial to precisely control the interface between metal (Pd) and metal oxide (MO_x) on $Pd/MO_x/Al_2O_3$.

We previously reported that galvanic deposition method has a potential to control an interface of two metal components.[33,34] This method is based on galvanic replacement due to the difference ionization tendency between two metal components. In these papers, we demonstrated that Ni core and Ag shell bimetal catalyst prepared by galvanic deposition method displayed a notable catalytic activity for CO oxidation. *Pan et al.* have also reported that $PdNi/Al_2O_3$ catalyst prepared by galvanic deposition method exhibited remarkable activity for methane combustion.[23] Galvanic deposition method has much potential to lead the special interface of two metal components.

According to our previous report on the preparation effect of $PdCo/Al_2O_3$, the interface between Pd and Co promoted the reduction-oxidation properties of Pd, leading to a higher catalytic activity.[29] However, the conventional preparation method was not effective for formation of Pd-Co interface. In this study, the use of galvanic deposition method to prepare $Pd/Co/Al_2O_3$ catalyst and the activity enhancement for methane combustion over $Pd/Co/Al_2O_3$ have been accomplished.

3-2. Experimental

Catalysts preparation

$Pd/Co/Al_2O_3$ was prepared by galvanic deposition (GD) method. First, Co supported on alumina catalyst was prepared by conventional impregnation method (denoted as Co/Al_2O_3-**I**). Next, Co/Al_2O_3-**I** was treated by H_2 at 600°C. Then, Co species were reduced to Co^0. The existence of Co^0 was confirmed by H_2-temperature programmed reduction (H_2-TPR) and X-ray absorption fine structure (XAFS) spectroscopy as shown as Fig. 1. After that, the degassed water and $Pd(NO_3)_2$ aqueous were dropped into the reduced Co/Al_2O_3-**I**. In this process, Pd deposits onto metallic Co due to the difference of ionization tendency between Pd and Co according to the following equation:

$$3Pd^{2+}_{(aq)} + 2Co^{0}_{(s)} \rightarrow 3Pd^{0}_{(s)} + 2Co^{3+}_{(aq)} \quad (1)$$

The obtained solid was centrifuged, washed with water, and dried at 80°C to obtain a Pd/Co/Al_2O_3 catalyst (denoted as Pd/Co/Al_2O_3-**GD**). The detailed scheme of GD method is displayed in Scheme 1.[33] As reference samples, Pd or Co supported on Al_2O_3 catalysts were prepared by conventional impregnation method, and Pd supported on Co/Al_2O_3 catalyst was prepared by a sequential impregnation method (denoted as Pd/Al_2O_3-**I**, Co/Al_2O_3-**I** and Pd/Co/Al_2O_3-**SI**, respectively).

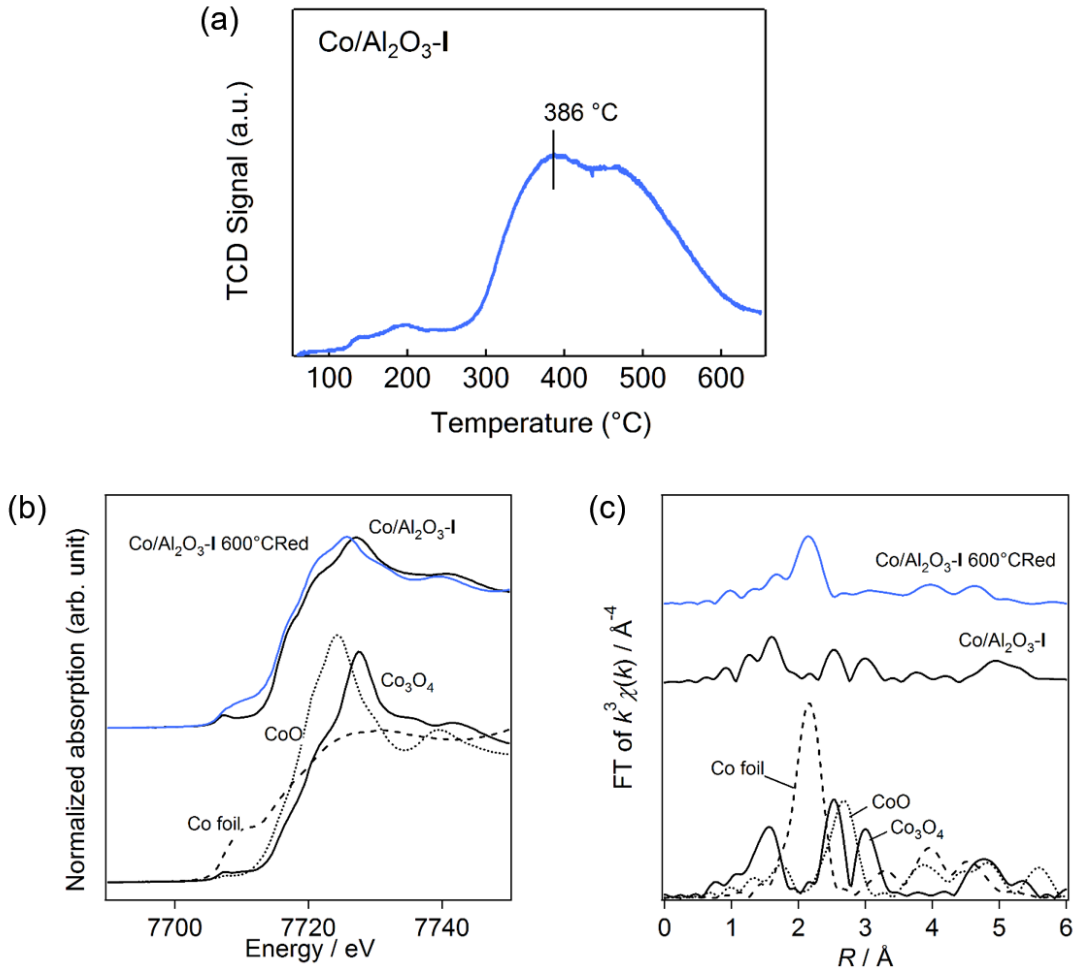

Figure 1. (a) H_2-temperature programmed reduction of Co/Al_2O_3-**I**. (b) Co K-edge X-ray absorption near edge structure (XANES) spectra of Co/Al_2O_3-I reduced by H_2 at 600 °C (blue). (c) FT of k^3-weighted Co K-edge extended XAFS (EXAFS) of Co/Al_2O_3-I reduced by H_2 at 600 °C (blue).

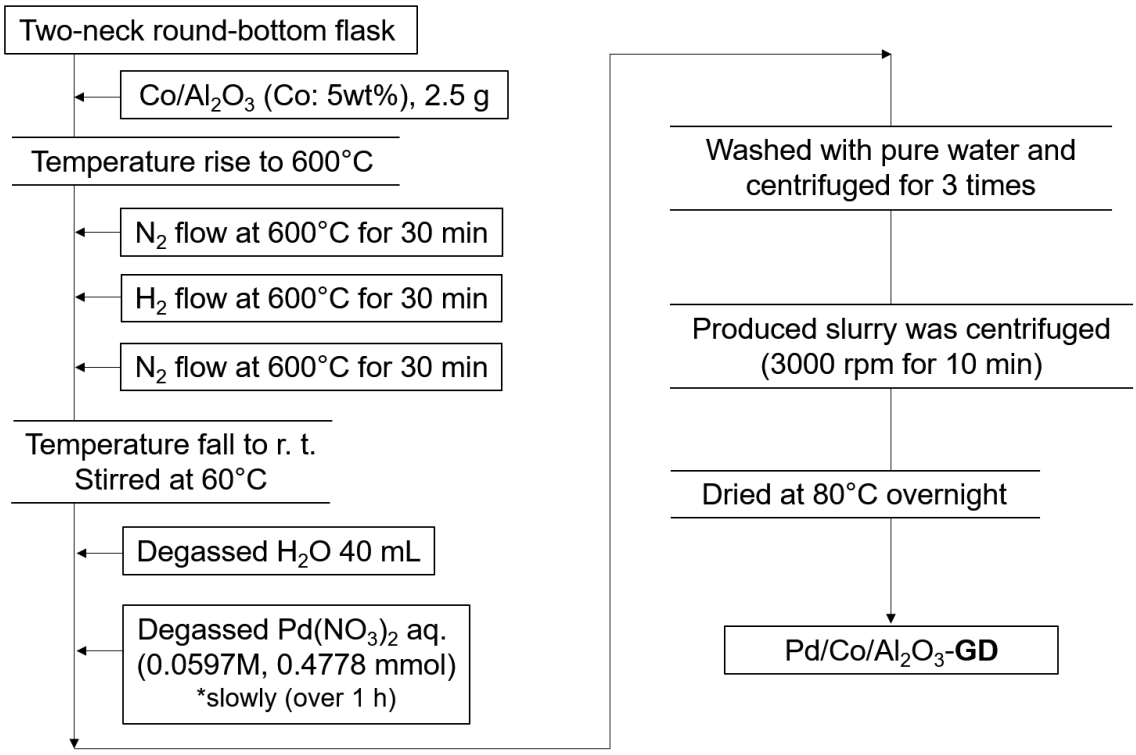

Scheme 1. Preparation scheme of Pd/Co/Al_2O_3-**GD**.

Catalytic activity test

The catalytic activity was evaluated by methane combustion using a conventional fixed-bed flow reactor at atmospheric pressure with a 20 mg of catalyst in a Pyrex glass tube with internal diameter of 4 mm. The catalytic run was carried out under a flow of 0.4% CH_4/10% O_2/He balance at a rate of 100 cm^3/min. The gas hourly space velocity was 300,000 mL/(h·g_{cat}). The effluent gas was analyzed by nondispersive infrared (NDIR) CO/CO_2 analyzer (Horiba VIA510) during stepwise increase in the reaction temperature. The steady state CH_4 conversion was measured after 20 min for each temperature.

Characterization method

The catalysts were characterized by X-ray diffraction (XRD), inductively coupled plasma (ICP), CO chemisorption, the high-angle annular dark-field scanning transmission electron microscopy (HAADF-STEM), energy-dispersive X-ray spectroscopy (EDX), XAFS spectroscopy, and O_2-temperature programmed desorption (O_2-TPD).

XRD analysis was carried out using Rigaku MiniFlex II/AP diffractometer with Cu Kα radiation. Metal loading of the catalysts were determined by ICP spectroscopy of the filtrate obtained during the centrifugation using Thermo Scientific iCAP7400Duo. CO chemisorption was carried out with BELCAT (Bel Japan Inc.) after oxidation pretreatment by O_2 at 500°C and reduction by H_2 at 50°C. HAADF-STEM images and EDX images were collected using a JEOL JEM-2100F at 200 kV. As the TEM samples, the catalysts used in methane combustion reaction were dispersed in methanol and

dropped onto a Cu mesh with a carbon microgrid. The XAFS measurements at the Pd K and Co K-edge were carried out on the BL01B1 beamline at the SPring-8 synchrotron radiation facility (8 GeV, 100mA) of the Japan Synchrotron Radiation Research Institute (JASRI) in Hyogo, Japan. The catalysts after used in methane combustion were measured without exposure to air. Data analysis was performed using Athena and Artemis including in the Demeter package. The curve-fitting analysis of the EXAFS spectra was performed for inverse Fourier transforms on the single scattering using theoretical parameters calculated by FEFF6. The Pd K-edge and Co K-edge EXAFS data were fitted among 3–12 $Å^{-1}$ and *k* space and 1–3 Å in *R* space. O_2-TPD was carried out with BELCAT (Bel Japan Inc.) after oxidation pretreatment by O_2 at 500°C and reduction by H_2 at 50°C.

3-3. Results and Discussion

Figure 2 shows the catalytic activity of methane combustion over the prepared catalysts. Methane combustion over Pd/Co/Al_2O_3-**GD** proceeded at a temperature about 50°C lower than that over Pd/Al_2O_3-**I**. On the other hand, ignition temperature of Pd/Co/Al_2O_3-**SI** was about 50°C higher than that of Pd/Al_2O_3-**I**. Co/Al_2O_3-**I** had no catalytic activity below 500°C, which suggests Pd species is the active site.

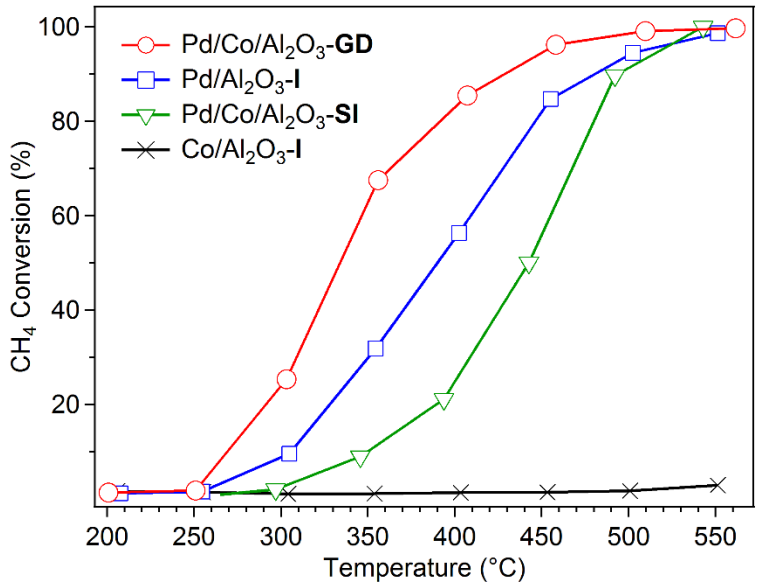

Figure 2. Methane combustion over (○) Pd/Co/Al_2O_3-**GD**, (□) Pd/Al_2O_3-**I**, (▽) Pd/Co/Al_2O_3-**SI** and (X) Co/Al_2O_3-**I**. Conditions: 20 mg catalysts, 300,000 mL/(h·g_{cat}), 4.1 kPa CH_4, 101 kPa O_2, helium balance, 100 mL/min.

To investigate the reason for the high catalytic activity of Pd/Co/Al_2O_3-**GD**, Pd particle size of the prepared catalysts was evaluated by CO chemisorption as shown in Table 1. The average Pd particle size of Pd/Co/Al_2O_3-**GD** was 8.2 nm, which is larger than that of Pd/Co/Al_2O_3-**SI** and Pd/Al_2O_3-**I** (i.

e. d_{Pd}=3.5 nm and 3.8 nm, respectively). According to the previous work, a catalyst having larger size of Pd exhibits higher turnover frequency (TOF) for methane combustion.[24] A Pd/Al_2O_3 catalyst was also prepared with Pd particle size similar to that of $Pd/Co/Al_2O_3$-**GD** (d_{Pd}= 7.7nm) by calcination of Pd/Al_2O_3-**I** at 850°C for 10 h. As a result, $Pd/Co/Al_2O_3$-**GD** showed higher activity than the Pd/Al_2O_3 having similar Pd particle size (Fig. 3). Therefore, the high activity of $Pd/Co/Al_2O_3$-**GD** is derived not only from the appropriate Pd particle size but also other factors.

Table 1. Summary of preparation method, Pd and Co loading, CO uptake for CO chemisorption and Pd average diameter ($d_{Pd\ MPs}$)

Catalyst	Preparation method	Pd loading (wt%)			Co loading (wt%)			CO uptake	$d_{Pd\ NPs}$
		Int.	ICP[c]	XAS[d]	Int.	ICP[c]	XAS[d]	(μmol/g)[d]	(nm)[e]
$Pd/Co/Al_2O_3$-**GD**	Galvanic deposition	0–2[b]	1.99	1.9	4.9–3.9[b]	3.7	4.8	26	8.2
$Pd/Co/Al_2O_3$-**SI**	Sequential impregnation	2[a]	-	1.9	4.9[a]	-	5.6	64	3.5
Pd/Al_2O_3-**I**	Impregnation	2[a]	-	1.9	-	-	-	58	3.8
Co/Al_2O_3-**I**	Impregnation	-	-	-	5[a]	-	4.8	-	-

a. Introduction amount.
b. Metal loading considered theoretically.
c. Estimated from ICP analysis for a filtrate which we can get by the galvanic deposition method.
d. Estimated from X-ray absorption amount using X-ray absorption spectroscopy (XAS).
CO uptake was measured by using CO chemisorption after oxidation pretreatment by O_2 at 500°C and reduction by H_2 at 50°C.
e. The particle size of Pd NPs was estimated by assuming a CO to surface metal atom ratio of 1:1.

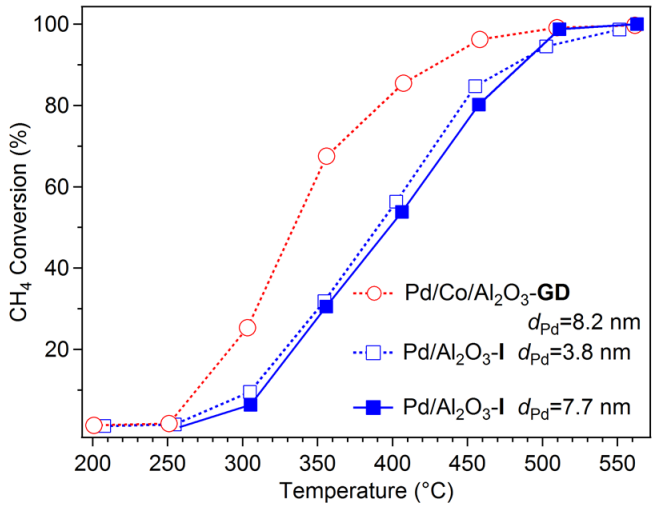

Figure 3. Methane combustion over Pd/Al_2O_3 with the Pd particle size equal to that of $Pd/Co/Al_2O_3$-**GD** (blue solid line).

Figure 4(a) and (b) show HAADF-STEM images with EDX analysis for Pd/Co/Al_2O_3-**GD** and Pd/Co/Al_2O_3-**SI**. On Pd/Co/Al_2O_3-**GD** (Fig. 4(a)), Co species are uniformly dispersed on solid catalyst, and Pd nanoparticles (NPs) are moderately dispersed with their size of 5–10 nm. As a result, the most of Pd particles are overlapping with Co species. Considering the mechanism of galvanic deposition which proceeds substitution of Co metal to Pd metal, Pd NPs should be deposited on Co species with rich Pd-Co interfaces on Pd/Co/Al_2O_3-**GD**. The high catalytic activity of Pd/Co/Al_2O_3-**GD** was derived from the rich Pd-Co interfaces. In the case of Pd/Co/Al_2O_3-**SI**, Co particles with the size about 50 nm were observed, and Pd were highly dispersed than that of Pd/Co/Al_2O_3-**GD** and Pd/Al_2O_3-**I** (Fig. 4(b)). The very small Pd species in Pd/Co/Al_2O_3-**SI** is responsible for the lower catalytic activity than Pd/Co/Al_2O_3-**GD** and Pd/Al_2O_3-**I**, even if Pd exists on Co species.

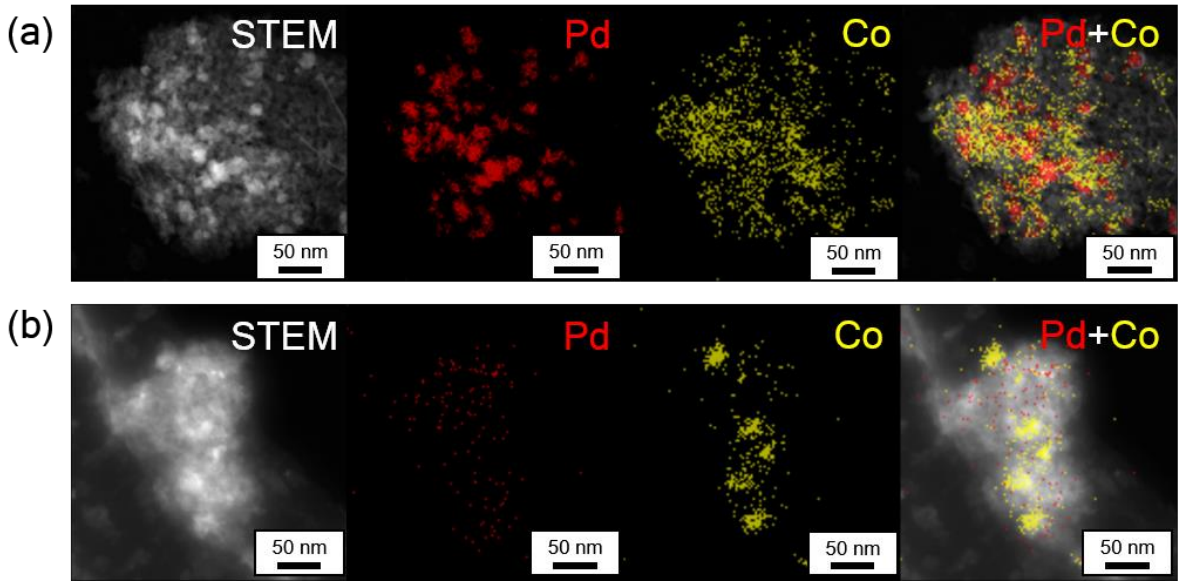

Figure 4. HAADF-STEM image and EDX elements mapping of (a) Pd/Co/Al_2O_3-**GD** and (b) Pd/Co/Al_2O_3-**SI**. The red and yellow color in EDX mapping correspond to Pd and Co, respectively. The catalysts were observed after activity tests.

Figure 5 shows the Fourier-transformed (FT) of the k^3-weighted Pd K-edge EXAFS spectra of Pd/Co/Al_2O_3-**GD**, Pd/Co/Al_2O_3-**SI** and Pd/Al_2O_3-**I**, together with Pd foil and PdO reference samples. The curve-fitting results are displayed in Table 2. All catalysts exhibit a peak at 1.60 Å due to Pd–O scattering in PdO. In addition, Pd K-edge XANES and k^3-weighted EXAFS spectra suggested the existence of PdO as shown in Fig. 6. For Pd/Co/Al_2O_3-**GD** and Pd/Al_2O_3-**I**, the peaks derived from Pd-O-Pd scatterings in PdO were observed clearly at 2.76 Å and 3.13 Å (Fig. 5). However, the peaks of Pd-O-Pd scatterings were not found for Pd/Co/Al_2O_3-**SI**, indicating highly dispersed PdO. The EXAFS results are consistent with EDX and XRD results (Fig.4 and Fig. 7). It should also be noted that Pd-Co alloy was not observed in Pd-K and Co-K EXAFS spectra in all catalysts (see Fig. 5, 6 and 8).

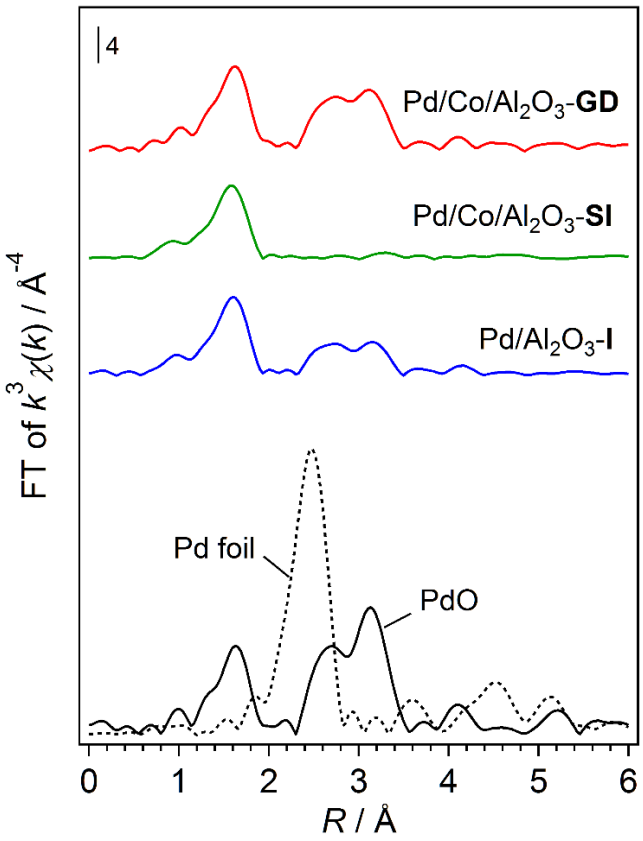

Figure 5. FT of k^3-weighted Pd K-edge EXAFS spectra of Pd/Co/Al_2O_3-**GD**, Pd/Co/Al_2O_3-**SI** and Pd/Al_2O_3-**I**. The catalysts were measured after activity tests.

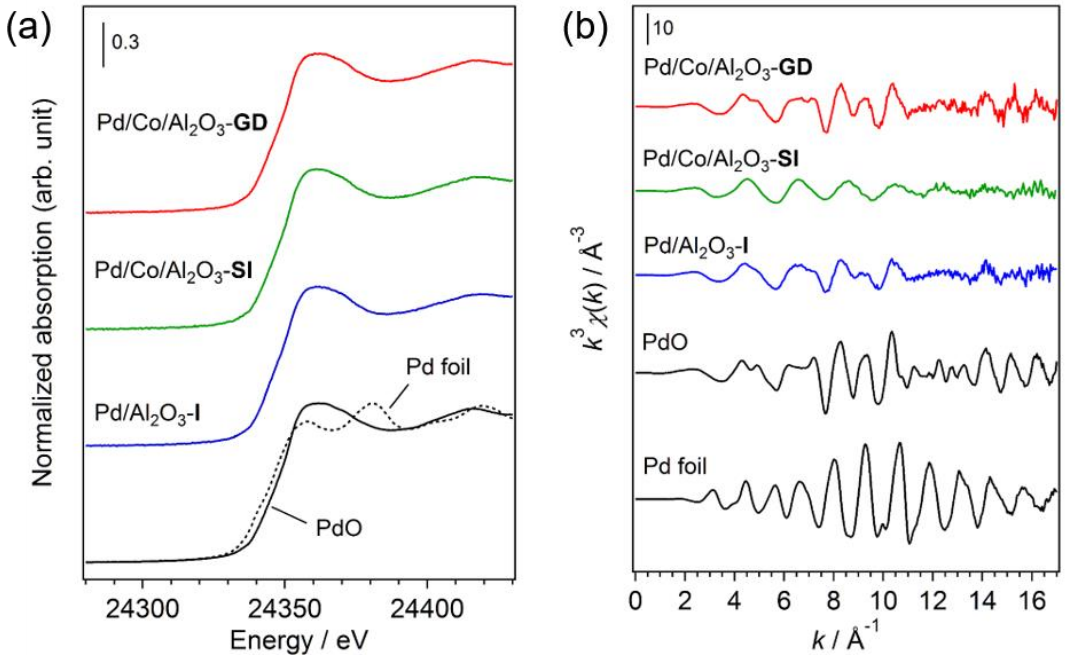

Figure 6. (a) Pd K-edge XANES and (b) k^3-weighted Pd K-edge EXAFS of the series of catalysts. The catalysts were measured after activity tests.

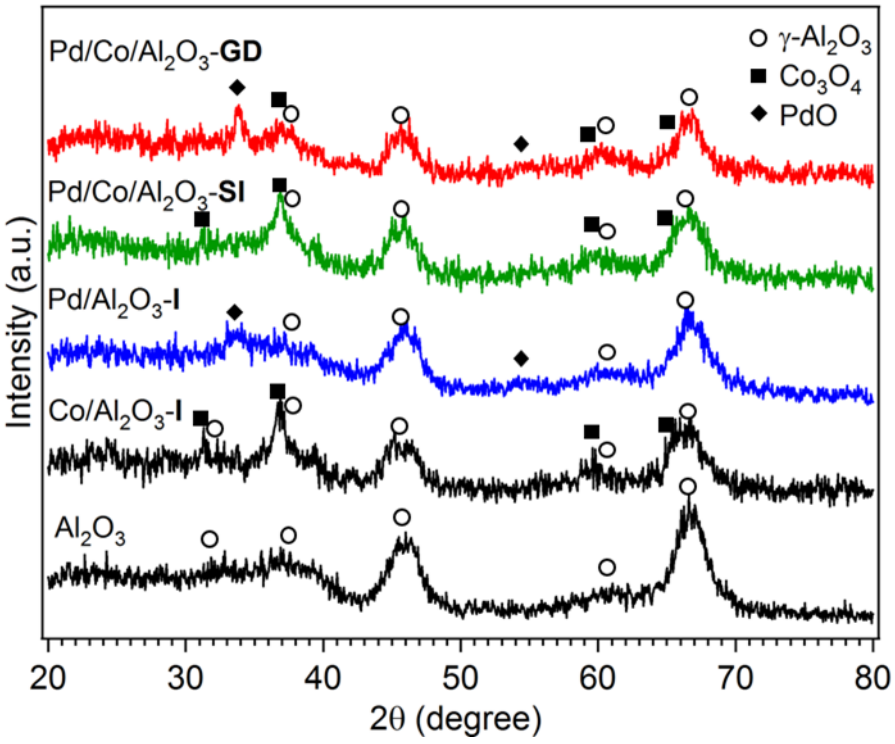

Figure 7. XRD spectra of prepared catalysts and Al_2O_3 as a support.

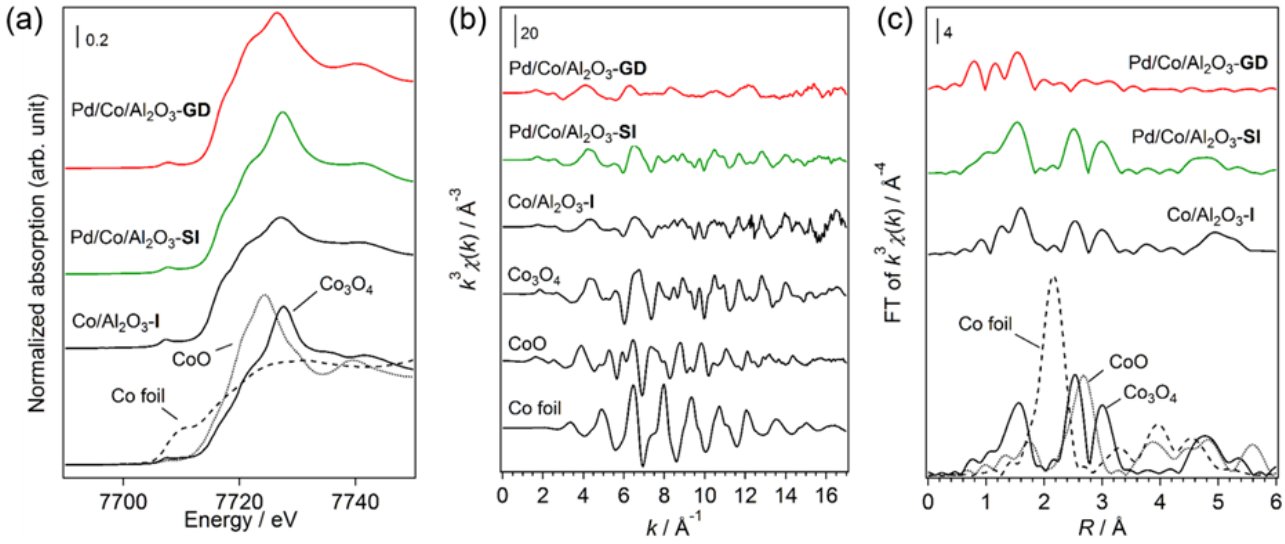

Figure 8. (a) Co K-edge XANES, (b) k^3-weighted Co K-edge EXAFS, and (c) FT of the k^3-weighted Co K-edge EXAFS of the series of catalysts. The catalysts were measured after activity tests.

Table 2. Curve-fitting result of the Pd K-edge EXAFS spectra of prepared catalysts, Pd foil and PdO as a reference.

Catalyst	Shell	C.N.	*R*/Å	$\sigma^2\times10^4$/Å^2	R_f/%
Pd/Co/Al_2O_3-**GD**	Pd–O	3.9±0.3	2.02±0.01	30±5	0.7
	Pd–Pd1	3.2±0.9	3.05±0.01	58±12	
	Pd–Pd2	4.3±1.2	3.43±0.01	58±12	
Pd/Co/Al_2O_3-**SI**	Pd–O	3.8±0.3	2.02±0.01	40±5	2.9
Pd/Al_2O_3-**I**	Pd–O	3.9±0.3	2.02±0.01	35±5	1.3
	Pd–Pd1	1.5±0.5	3.05±0.01	47±14	
	Pd–Pd2	2.1±0.8	3.43±0.01	53±15	
Pd foil	Pd–Pd	12*	2.74	60±3	0.1
PdO	Pd–O	4*	2.01	28±5	1.2
	Pd–Pd1	4*	3.05	49±4	
	Pd–Pd2	8*	3.43	49±4	

It has been reported that the rate-determining step of methane combustion over Pd-based catalysts is C–H bond activation of methane accompanied by the reduction of PdO.[27,35,36] Accordingly, the reducibility of PdO was investigated by O_2-temperature programmed desorption (O_2-TPD) after the oxidation of catalysts in a flow of O_2 at 500°C for 30 min as shown in Fig. 9. The peaks between 650°C and 800°C were attributed to oxygen desorption from PdO.[23] The peak of Pd/Co/Al_2O_3-**GD** was observed at 677°C, which is a lower temperature than that of Pd/Al_2O_3-**I** and Pd/Co/Al_2O_3-**SI**. The result indicates that PdO of Pd/Co/Al_2O_3-**GD** have higher reducibility than the other catalysts. The high reducibility of PdO species leads to a higher catalytic activity for Pd/Co/Al_2O_3-**GD**.

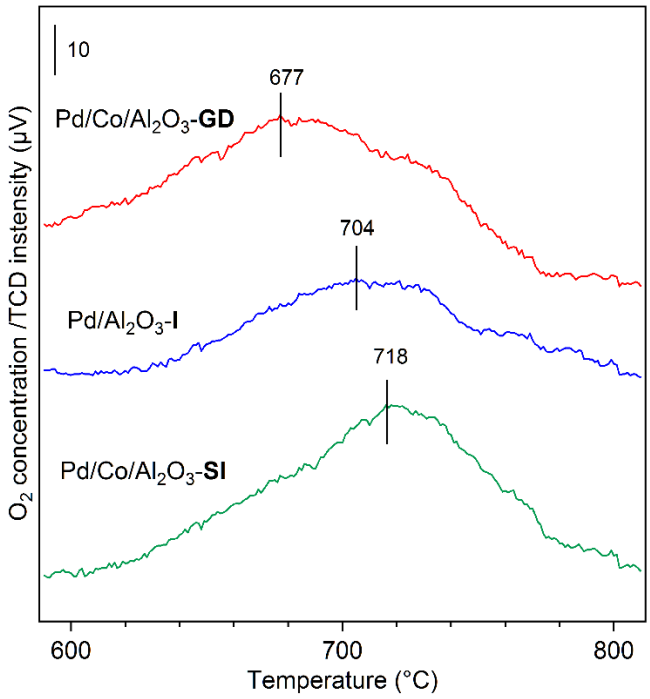

Figure 9. O_2-TPD of Pd/Co/Al_2O_3-**GD**, Pd/Co/Al_2O_3-**SI**, and Pd/Al_2O_3-**I**.

3-4. Conclusion

Pd/Co/Al_2O_3 catalyst was successfully prepared by galvanic deposition method (Pd/Co/Al_2O_3-**GD**). Galvanic deposition method provided rich interfaces between PdO and CoO_x as well as appropriate PdO particle size. Pd/Co/Al_2O_3-**GD** exhibited a notable catalytic activity for methane combustion. The high catalytic performance can be attributed to the higher reducibility of PdO NPs on CoO_x species.

3-5. References

1 Choudhary, T., Banerjee, S. & Choudhary, V. *Appl. Catal., A* **234**, 1-23, (2002).

2 Gélin, P. & Primet, M. *Appl. Catal., B* **39**, 1-37, (2002).

3 Farrauto, R. J. *Science* **337**, 659-660, (2012).

4 Briot, P. & Primet, M. *Applied catalysis* **68**, 301-314, (1991).

5 Farrauto, R. J., Hobson, M., Kennelly, T. & Waterman, E. *Appl. Catal., A* **81**, 227-237, (1992).

6 Burch, R. & Loader, P. *Appl. Catal., B* **5**, 149-164, (1994).

7 Lampert, J. K., Kazi, M. S. & Farrauto, R. J. *Appl. Catal., B* **14**, 211-223, (1997).

8 Widjaja, H., Sekizawa, K., Eguchi, K. & Arai, H. *Catal. Today* **35**, 197-202, (1997).

9 Sekizawa, K., Widjaja, H., Maeda, S., Ozawa, Y. & Eguchi, K. *Appl. Catal., A* **200**, 211-217, (2000).

10 Eguchi, K. & Arai, H. *Appl. Catal., A* **222**, 359-367, (2001).

11 Demoulin, O. *et al. Phys. Chem. Chem. Phys.* **5**, 4394-4401, (2003).

12 Zhu, G., Han, J., Zemlyanov, D. Y. & Ribeiro, F. H. *J. Am. Chem. Soc.* **126**, 9896-9897, (2004).

13 Persson, K., Ersson, A., Jansson, K., Iverlund, N. & Jaras, S. *J. Catal.* **231**, 139-150, (2005).
14 Persson, K., Ersson, A., Jansson, K., Fierro, J. & Jaras, S. *J. Catal.* **243**, 14-24, (2006).
15 Grunwaldt, J. D., van Vegten, N. & Baiker, A. *Chem. Commun. (Camb)*, 4635-4637, (2007).
16 Yoshida, H., Nakajima, T., Yazawa, Y. & Hattori, T. *Appl. Catal., B* **71**, 70-79, (2007).
17 Di Carlo, G. *et al. Chem. Commun. (Camb)* **46**, 6317-6319, (2010).
18 Kinnunen, N. M., Hirvi, J. T., Suvanto, M. & Pakkanen, T. A. *J. Phys. Chem. C* **115**, 19197-19202, (2011).
19 Mayernick, A. D. & Janik, M. J. *J. Catal.* **278**, 16-25, (2011).
20 Cargnello, M. *et al. Science* **337**, 713-717, (2012).
21 Kinnunen, N. M., Hirvi, J. T., Suvanto, M. & Pakkanen, T. A. *J. Mol. Catal. A: Chem.* **356**, 20-28, (2012).
22 Antony, A., Asthagiri, A. & Weaver, J. F. *J. Chem. Phys.* **139**, 104702, (2013).
23 Pan, X., Zhang, Y., Miao, Z. & Yang, X. *J. Energy Chem.* **22**, 610-616, (2013).
24 Stakheev, A. Y. *et al. Top. Catal.* **56**, 306-310, (2013).
25 Chen, C. *et al. ACS Catal.* **4**, 3902-3909, (2014).
26 Guo, G., Lian, K., Gu, F., Han, D. & Wang, Z. *Chem. Commun. (Camb)* **50**, 13575-13577, (2014).
27 Miller, J. B. & Malatpure, M. *Appl. Catal., A* **495**, 54-62, (2015).
28 Nilsson, J. *et al. ACS Catal.* **5**, 2481-2489, (2015).
29 Satsuma, A. *et al. Catal. Today* **242**, 308-314, (2015).
30 Stefanov, P. *et al. Chem. Eng. J.* **266**, 329-338, (2015).
31 Liu, Y. *et al. Appl. Catal., B* **119-120**, 321-328, (2012).
32 Liu, Y. *et al. Fuel Process. Technol.* **111**, 55-61, (2013).
33 Mahara, Y. *et al. Chem. Lett.* **43**, 910-912, (2014).
34 Mahara, Y., Ishikawa, H., Ohyama, J., Sawabe, K. & Satsuma, A. *Catal. Today* **265**, 2-6, (2016).
35 Giakoumelou, I., Fountzoula, C., Kordulis, C. & Boghosian, S. *J. Catal.* **239**, 1-12, (2006).
36 Chin, Y. H., Buda, C., Neurock, M. & Iglesia, E. *J. Am. Chem. Soc.* **135**, 15425-15442, (2013).

Chapter 4
Methane combustion over $Pd/CoAl_2O_4/Al_2O_3$ catalysts prepared by galvanic deposition

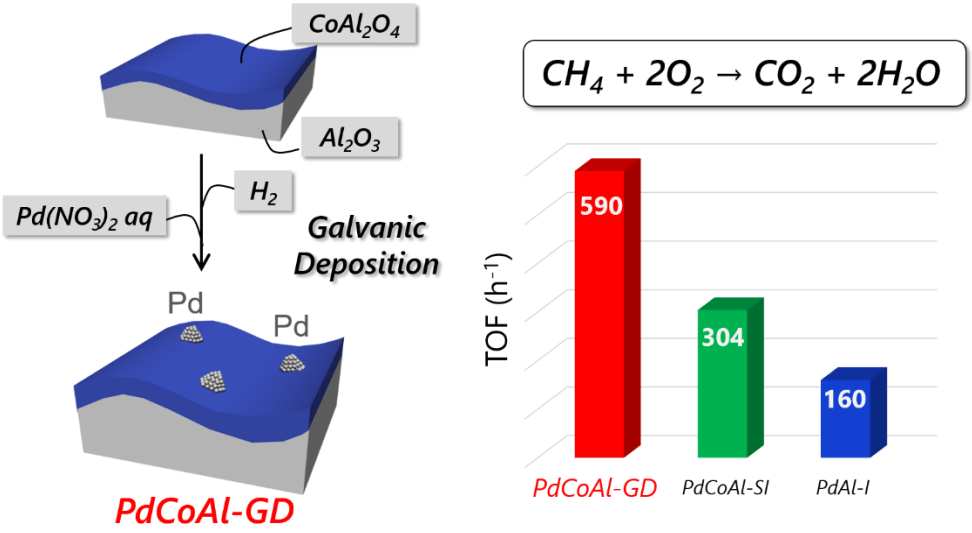

$Pd/CoAl_2O_4/Al_2O_3$ methane combustion catalysts were synthesized using a galvanic deposition (GD) method (PdCoAl-GD). This PdCoAl-GD catalyst showed higher activities and turnover frequencies (TOFs) than conventional Pd/Al_2O_3. According to X-ray diffraction (XRD), X-ray absorption fine structure (XAFS) and scanning transmission electron microscopy (STEM) measurements, PdCoAl-GD was comprised of a $CoAl_2O_4$ phase supported on γ-Al_2O_3 and dispersed Pd nanoparticles of 2–7 nm in size on $CoAl_2O_4$. Operando Pd K-edge XAFS measurements indicated that Pd in PdCoAl-GD was oxidized to highly active methane combustion PdO species at low temperatures. PdCoAl-GD also showed high activity (light-off tests) when PdO was initially present on the catalysts. Methane temperature-programmed reaction (CH_4-TPR) measurements on PdCoAl-GD revealed that PdO was reduced by CH_4 at low temperatures. The GD method used herein achieved PdO species that were effective for C–H activation.

Contents

4-1. Introduction

Natural gas vehicles are becoming widely used because of their cleaner exhaust gas characteristics as compared to conventional fossil fuel-based automobiles. However, unburned methane emissions are hazardous and have a high greenhouse effect coefficient, which is 21 times higher than that of carbon dioxide. Complete oxidation of methane using supported heterogeneous catalysts has become increasingly important for the emission reduction of unburned methane.[1-3] Supported Pd catalysts have been used because of their high activity in methane combustion,[4-37] and alumina-supported Pd catalysts (Pd/Al_2O_3) are used, especially, due to their high activity and thermal stability. However, the methane combustion activity at low temperatures is still insufficient, and the development of a highly active catalyst at low temperatures is strongly desired.

With the aim to design catalysts with higher activity, it is important to control the Pd–metal oxide interaction. Cargnello *et al.* synthesized $Pd@CeO_2$ catalysts that have attracted attention because of their exceptional methane combustion activities,[16] and the influence of the Pd–CeO_2 interfaces on the high methane combustion activity has been experimentally and theoretically studied.[14,38,39] Zou *et al.* prepared alumina-supported core–shell NiO@PdO catalysts with higher Pd utilization efficiencies than Pd/CeO_2. However, these catalysts were prepared by a complex method (i.e., multi-step reactions and protective agents); thus, a simpler preparation method is desired. The addition of transition metal (e.g., Ni or Co) oxides to Pd/Al_2O_3 catalysts has been reported to improve their methane combustion activity.[6,18,19,26,27,32,37] However, in order to improve the activity, Pd is required to be in good contact with the additional element species. In this sense, we used a galvanic deposition (GD) method to enhance the interaction between Pd and CoO_x species.[31] The GD method allowed to support a metal over a second metal having higher ionization tendency. Thus, different metals were deposited upon contact between the two metals, thereby enhancing their interfacial interaction. $Pd\text{-}Co/Al_2O_3$ catalysts prepared by a GD method showed significantly higher methane combustion activities than Pd/Al_2O_3 and $Pd\text{-}Co/Al_2O_3$ prepared by a conventional impregnation method. However, this improvement in activity was insufficient because of the poor contact between Pd and the relatively large Co particles. The interfacial contact between Pd and Co is expected to improve by precipitating Pd with a GD method after dispersion Co by a solid solution in Al_2O_3.

In this study, we synthesized highly active $Pd/CoAl_2O_4/Al_2O_3$ methane combustion catalysts with enhanced interfacial contact between Pd and $CoAl_2O_4$ using a GD method. The oxidation state of Pd during the reaction was observed in situ by operando X-ray absorption fine structure (XAFS) spectroscopy.

4-2. Experimental section

Catalyst preparation

$Co(NO_3)_2{\cdot}6H_2O$ (98%) was purchased from Kishida Chemical. A 4.5 wt% $Pd(NO_3)_2$ aqueous solution and high purity Al_2O_3 (99%) were supplied from Cataler Corporation and SASOL, respectively.

$CoAl_2O_4/Al_2O_3$ (5 wt% Co loading) was prepared by an impregnation method. An aqueous suspension containing boehmite and $Co(NO_3)_2 \cdot 2H_2O$ was stirred for 1 h. After evaporation and overnight drying at 80 °C, the resulting solid was calcined at 900 °C for 3 h. The solid was denoted as CoAl900.

$Pd/CoAl_2O_4/Al_2O_3$ was prepared with CoAl900 and $Pd(NO_3)_2$ by a GD method as described in previous reports (Scheme 1). [31,40-42] 2.5 g of CoAl900 were added to a two-neck round-bottom flask which was capped with a septum. CoAl900 was reduced under flowing H_2 at 600 °C for 30 min. After switching to N_2, the two-neck round-bottom flask containing CoAl900 was kept at 60 °C. 40 mL of degassed H_2O was added to a two-neck round-bottom flask under stirring and 0.478 mmol of aqueous $Pd(NO_3)_2$ were subsequently injected. The slurry was stirred for 1 h, centrifuged and dried overnight. The resulting material was denoted as PdCoAl-GD. Inductively coupled plasma analysis revealed a Pd loading of 1.9 wt% on PdCoAl-GD, which was equal to the nominal loading. The Co loading was lower than that of CoAl900 (4.7 vs. 5.0 wt%), thereby revealing that a fraction of Co was dissolved into water during deposition of Pd.

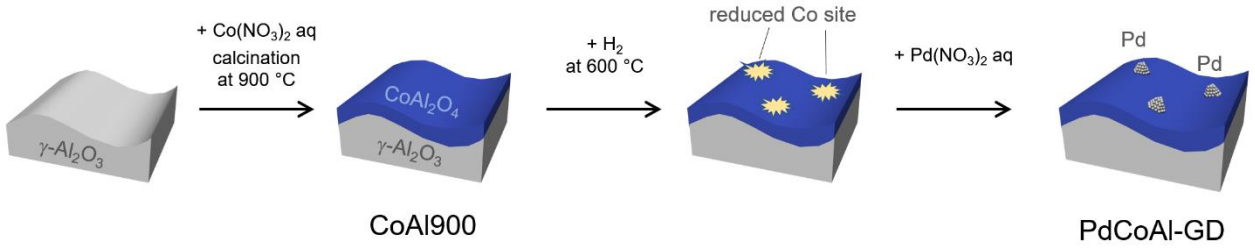

Scheme 1. Synthetic procedure for $Pd/CoAl_2O_4/Al_2O_3$ using galvanic deposition method.

As a reference catalyst, Pd/Al_2O_3 was prepared by a conventional impregnation method using a $Pd(NO_3)_2$ solution and Al_2O_3. The mixture was dried and calcined in air at 500 ºC for 3 h (denoted as PdAl-I). A $Pd/CoAl_2O_4/Al_2O_3$ catalyst was also prepared by a sequential impregnation method using a $Pd(NO_3)_2$ solution and CoAl900. The mixture was dried and calcined in air at 500 ºC for 3 h (denoted as PdCoAl-SI). The Pd and Co loadings of the catalysts were adjusted to 2 and 4.9 wt%, respectively.

Catalytic Tests

Light-off methane combustion tests were conducted using a conventional fixed-bed flow reactor at atmospheric pressure with 20 mg of catalyst loaded in a Pyrex glass tube with an internal diameter of 4 mm. In this study, we performed catalytic tests under two pretreatment conditions: (i) O_2 at 500 °C for 10 min, followed by a H_2 treatment at 500 °C for 10 min (initial state of Pd: Pd^0); and (ii) O_2 treatment at 500 °C for 10 min (initial state of Pd: PdO). The catalytic tests were performed under flowing (100 mL/min) 0.4% CH_4/10% O_2/He balance. The reaction temperature ranged from 200 to 600 °C, and the heating rate was 5 °C/min. The gas hourly space velocity was 300,000 mL/(h·g_{cat}). The effluent gas was analyzed by a nondispersive infrared (NDIR) CO/CO_2 analyzer (Horiba VIA510) while stepwise increasing the reaction temperature.

Catalyst Characterization

The prepared catalysts were characterized by X-ray diffraction (XRD), XAFS, high-angle annular dark-field scanning transmission electron microscopy (HAADF-STEM), CO adsorption, as well as methane temperature-programmed reductions (CH_4-TPR).

The XRD patterns of the catalysts were recorded on a Rigaku MiniFlex II/AP diffractometer with a Cu Kα radiation. All samples were measured after preparation without performing any pretreatment.

The Co K-edge XAFS spectra were obtained on the BL01B1 beamline at the SPring-8 synchrotron radiation facility (8 GeV, 100 mA) of the Japan Synchrotron Radiation Research Institute (JASRI) in Hyogo, Japan. The XAFS measurements (transmission mode) were performed ex situ. The samples were pelletized (7 mm in diameter). PdCoAl-GD and PdCoAl-SI were ex situ measured after methane combustion tests at 600 °C, while CoAl900 was measured after no pretreatment. The data analysis was performed using the Athena and Artemis softwares including in the Demeter package. The curve-fitting analysis of the EXAFS spectra was performed for the inverse Fourier transforms assuming single scattering using the theoretical parameters calculated by FEFF6. The Co K-edge EXAFS data were fitted between 3–12 Å in *k* space and 1–3 Å in *R* space.

HAADF-STEM and energy dispersive X-ray (EDX) images were collected using a JEOL JEM-2100F microscope operating at 200 kV. For TEM analysis, the spent catalysts were dispersed in methanol and dropped onto a Cu mesh provided with a carbon microgrid.

CO chemisorption was carried out on a BELCAT (Bel Japan Inc.) apparatus, while CH_4-TPR was carried out using a NDIR CO/CO_2 analyzer (Horiba VIA510). CO chemisorption was performed after oxidation (O_2 at 500 °C) and reduction (H_2 at 50 °C) pretreatments. For the CH_4-TPR measurements, 50 mg of the sample were heated from 200 to 600 °C at a rate of 5 °C/min under flowing 0.4% CH_4 in N_2 (50 mL/min) after a pretreatment with flowing O_2 at 500°C.

Operando Pd K-edge XAFS Spectroscopy

Operando Pd K-edge XAFS measurements were performed at BL01B1, SPring-8, Japan. The samples were pelletized (7 mm in diameter) and set in a quartz glass XAFS cell. The measurement sequence was carried out at the same conditions employed for the methane combustion catalytic tests. Thus, after a pretreatment with flowing O_2 (500 °C) and H_2 (500 °C), the catalyst was contacted with flowing 0.4% CH_4/10% O_2/He (reaction mixture) and heated at a rate of 5 °C/min from 200 to 500 °C. During this heating, quick Pd K-edge XAFS spectra were obtained in a transmission mode. In addition, the composition (i.e., CH_4, CO, CO_2, H_2O, O_2, etc.) of the outlet gas was analyzed by mass spectrometry (MS).

4-3. Results and discussion

Catalytic Activity

We carried out methane combustion tests on the prepared catalysts. The catalysts were H_2

pretreated at 500 °C to reduce the Pd species to a metallic phase. Figure 1(a) shows the light-off methane combustion curves for PdCoAl-GD, PdCoAl-SI, PdAl-I and CoAl900. T_{10} was defined as the temperature at which methane conversion reached 10%. As shown in Table 1, PdCoAl-GD showed the best low-temperature combustion activity since its T_{10} (266 °C) was ca. 20 °C lower than those of PdAl-I and PdCoAl-SI. T_{10} of PdCoAl-SI was slightly lower than that of PdAl-I. Compared with the catalysts previously reported, PdCoAl-GD showed comparable high activity (Figure 2).[14,16,20,24,30,33,36,37,43] The apparent activity followed a different trend PdAl-I > PdCoAl-SI at high temperatures. CoAl900 showed no catalytic activity below 400 °C, thereby suggesting that Pd species were the active sites in this reaction. The turnover frequencies (TOFs) for prepared catalysts were estimated by the following equation:

$$\mathrm{TOF} = \frac{\text{Reaction rate at 300 °C [mol}\cdot h^{-1}\text{]}}{\text{Number of surface Pd [mol]}}$$

The number of surface Pd atoms was estimated from the CO chemisorption data. The diameter of the Pd particles obtained by CO chemisorption was also confirmed by the particle size distribution obtained from the HAADF-STEM images. The CO uptake, Pd particle size and TOF values at 300 °C for the catalysts are summarized in Figure 1(b) and Table 1. The TOF at 300 °C for methane combustion followed the trend PdCoAl-GD > PdCoAl-SI > PdAl-I. The TOF of PdCoAl-GD (590 h^{-1}) was twice that of PdCoAl-SI (304 h^{-1}), and four times higher than that of PdAl-I (160 h^{-1}). PdCoAl-GD, PdCoAl-SI and PdAl-I were estimated to have average Pd particle sizes of 4.3, 6.3 and 3.8 nm, respectively. According to a previous work, catalysts having large sized Pd particles exhibited higher TOFs for methane combustion.[21] Therefore, we prepared several Pd/Al_2O_3 and $Pd/Co/Al_2O_3$ catalysts with varying Pd particle sizes, and we measured the TOF values of these catalysts (Table 2). PdCoAl-GD showed a noticeably high TOF even considering the Pd size effects (Figure 3). Considering the above data, PdCoAl-GD was particularly active toward the methane combustion reaction in the low-temperature range.

Table 1. Catalytic test, CO uptake, Pd particle size, and TOF results.

Catalysts	T_{10} (°C)	CO uptake (10^{-6} mol g^{-1})[a]	$d_{\text{Pd-CO}}$ (nm)[b]	$d_{\text{Pd-TEM}}$ (nm)	TOF at 300°C (h^{-1})
PdCoAl-GD	266	48.5	4.3	4.2	590
PdCoAl-SI	285	33.5	6.3	6.2	304
PdAl-I	288	57.6	3.8	4.2	160

[a] CO uptake was measured by CO chemisorption after an oxidation pretreatment with O_2 at 500 °C and reduction with H_2 at 50 °C. [b] The Pd particle size was estimated by assuming a CO to surface metal atom ratio of 1:1.

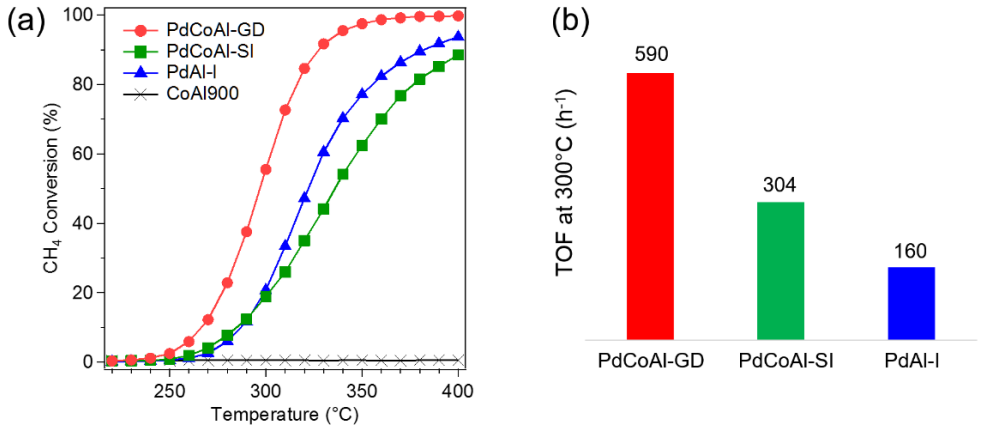

Figure 1. (a) Methane combustion light-off curves of PdCoAl-GD, PdCoAl-SI, PdAl-I and CoAl900. Pretreatment: flowing O_2 at 500 °C followed by flowing H_2 at 500 °C. (b) Methane combustion TOF at 300 °C over PdCoAl-GD, PdCoAl-SI and PdAl-I.

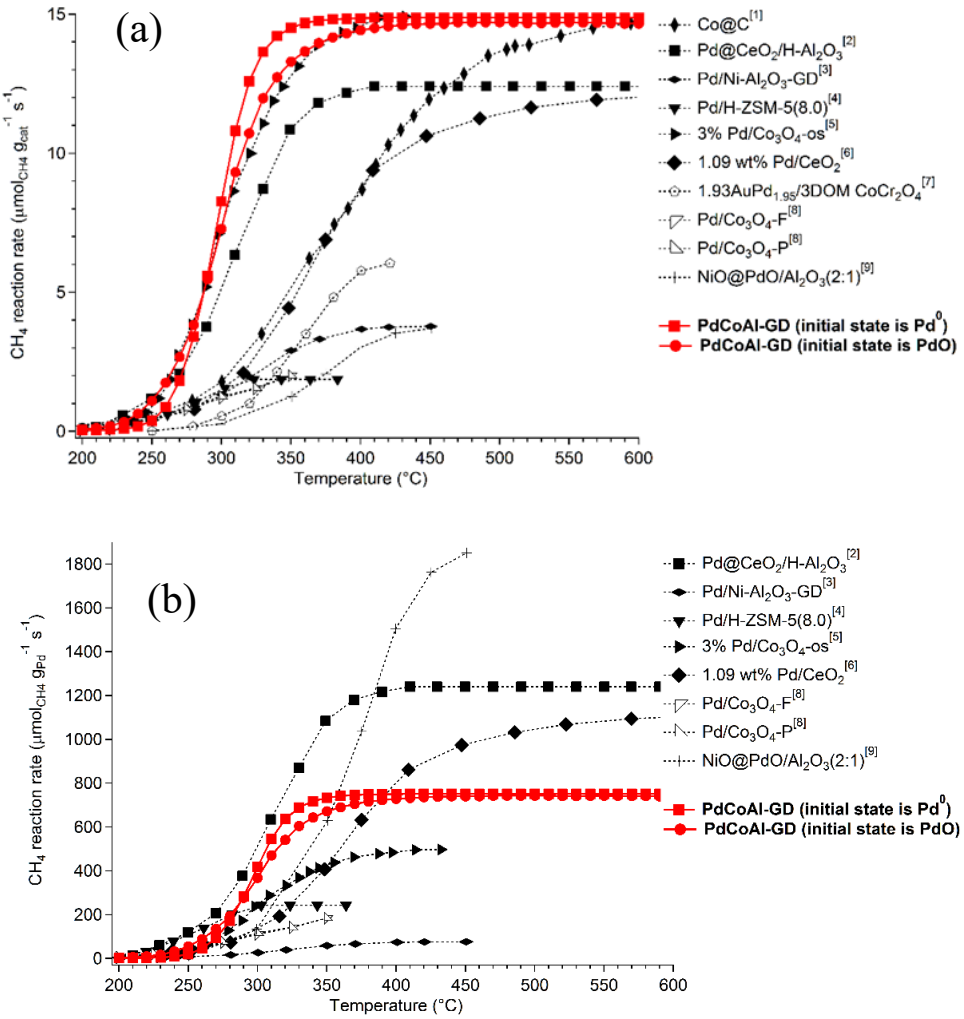

Figure 2. Methane combustion activities for representative catalysts. (a) Methane reaction rate per amount of catalyst. (b) Methane reaction rate per amount of Pd.

Table 2. List of PdCoAl-SI and PdAL-I catalysts with different Pd particle sizes.

Catalysts	Support	preparation method	Calcination	Pd loading (wt%)	Co loading (wt%)	d_{Pd-CO} (nm)	TOF at 300°C (h^{-1})[c]
Series of PdCoAl-SI	Al_2O_3(sasol)	Sequential Impregnation	500°C for 3 h	0.5[a]	5[a]	3	63
	Al_2O_3(sasol)	Sequential Impregnation	500°C for 3 h	1[a]	5[a]	3.7	71
	Al_2O_3(sasol)	Sequential Impregnation	500°C for 3 h	2[a]	5[a]	6.3	304
	Al_2O_3(sasol)	Sequential Impregnation	900°C for 10 h	2[a]	5[a]	23.1	407
Series of PdAl-I	Al_2O_3(sasol)	Impregnation	500°C for 3 h	1[a]	-	1.9	17
	Al_2O_3(sasol)	Impregnation	500°C for 3 h	2[a]	-	3.7	160
	Al_2O_3(sasol)	Impregnation	800°C for 10 h	2[a]	-	5.4	164
	Al_2O_3(sasol)	Impregnation	850°C for 10 h	2[a]	-	7.7	197
	Al_2O_3(sasol)	Impregnation	900°C for 10 h	2[a]	-	19.1	290

[a] Nominal value.

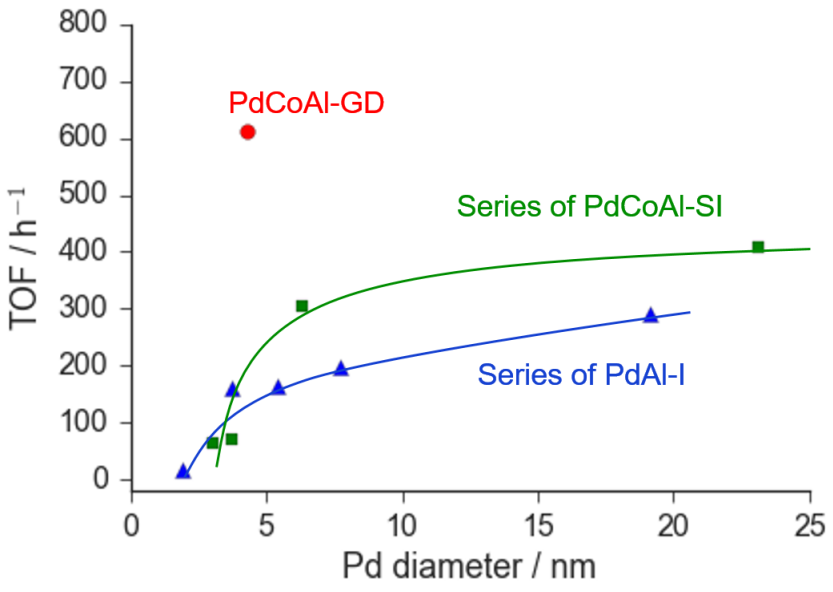

Figure 3. Effect of the Pd particle diameter on the methane combustion TOF at 300 °C.

Catalyst Structure

The catalyst structure was characterized by XRD, XAFS spectroscopy and HAADF-STEM observations.

Figure 4 shows the XRD patterns of the prepared catalysts. The diffraction patterns confirmed the presence of a γ-Al_2O_3 phase in all cases. Since the diffraction lines originated from Pd were hardly observed, we assumed that Pd was in the form of highly dispersed nanoparticles. The samples containing Co showed XRD patterns characteristics of Co_3O_4 or $CoAl_2O_4$ phases, although we could not discriminate between these structures. Therefore, to investigate the surrounding structure of Co in more detail, XAFS measurements were carried out. Figure 5 shows the normalized Co K-edge X-ray absorption near-edge spectroscopy (XANES) spectra for PdCoAl-GD, PdCoAl-SI, CoAl900, and reference materials. All the prepared catalysts showed XANES spectra similar to that of $CoAl_2O_4$. Figure 6 shows the k^3-weighted Co K-edge EXAFS spectra of CoAl900, PdCoAl-GD, PdCoAl-SI, and reference materials. CoAl900, PdCoAl-GD and PdCoAl-SI showed EXAFS spectra similar to that of $CoAl_2O_4$ (and not Co_3O_4). The curve-fitting results of PdCoAl-GD are shown in Table 3. The spectra of PdCoAl-GD showed a first peak at 1.6 Å originated by the Co–O shell and a second peak at 3.0 Å ascribed to the Co–Al, Co–O and Co–Co shells of $CoAl_2O_4$ (Table 3). CoAl900 and PdCoAl-SI also showed spectra similar to that of $CoAl_2O_4$. These results indicated that Co in CoAl900 was almost completely dissolved into the γ-Al_2O_3 phase upon calcination at 900 °C forming a $CoAl_2O_4$ phase. Additionally, we obtained the Co 2p X-ray photoelectron spectroscopy (XPS) spectra of all the samples (Figure 7). Therefore, $CoAl_2O_4$ species were considered to be present near the surface of γ-Al_2O_3.

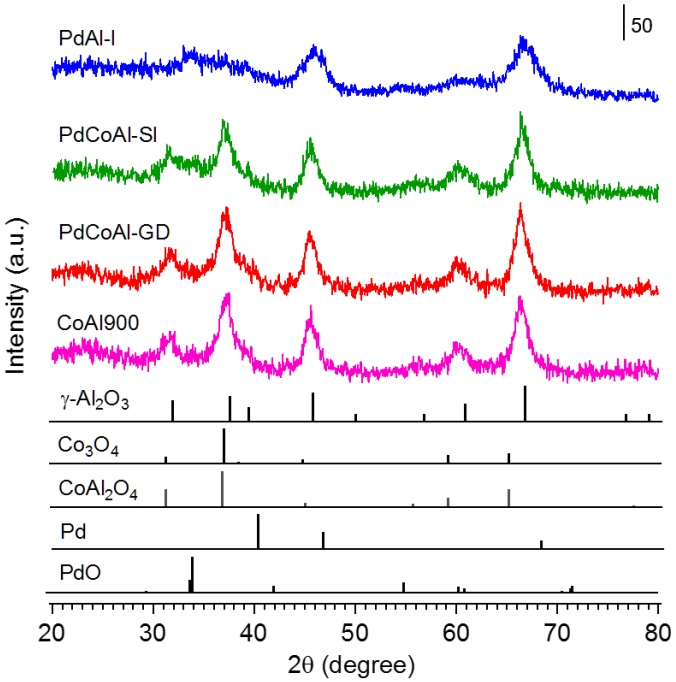

Figure 4. X-ray diffraction patterns of: PdCoAl-GD, PdCoAl-SI, PdAl-I and CoAl900. The bottom peaks indicate the position of the reference materials.

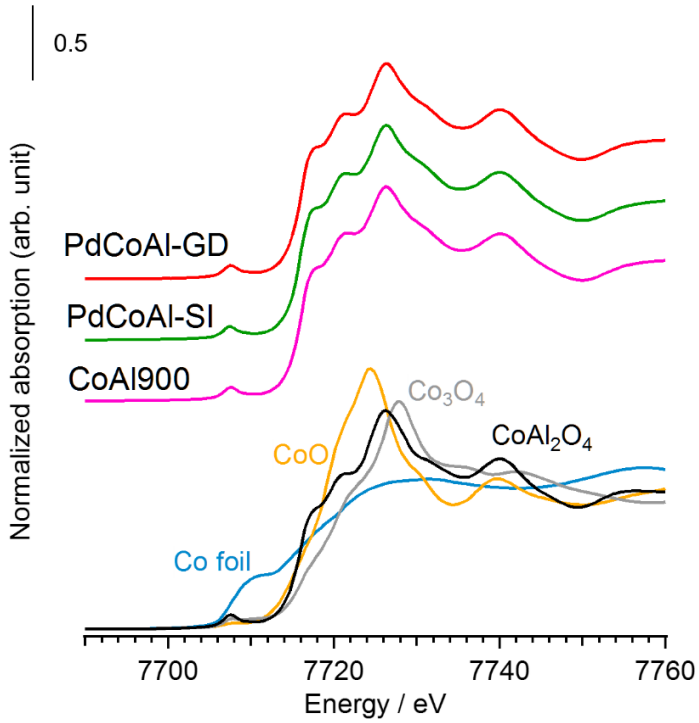

Figure 5. Normalized absorption spectra at the Co K-edge for PdCoAl-GD (red), PdCoAl-SI (green), CoAl900 (pink) and references (Co foil: royal blue, CoO: orange, Co_3O_4: gray and $CoAl_2O_4$: black).

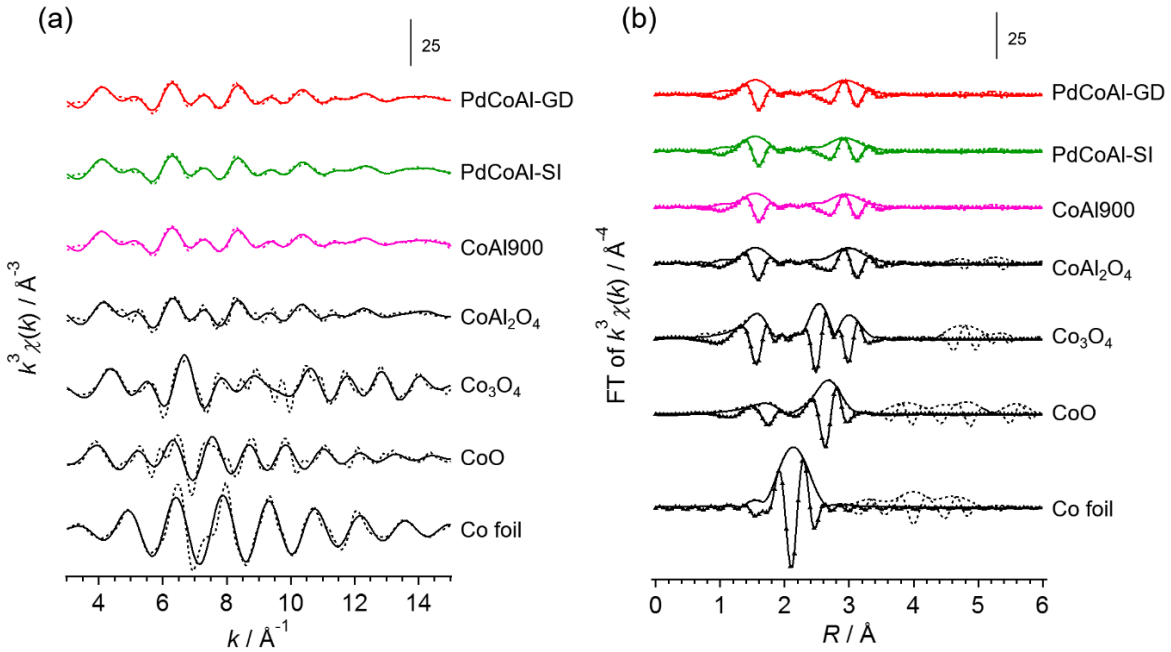

Figure 6. (a) k^3-weighted Co K-edge EXAFS spectra and (b) Fourier transform of PdCoAl-GD (red), PdCoAl-SI (green), CoAl900 (pink) and references (black). Dotted lines: raw data; solid line: fitting data; marked: imaginary part of the Fourier transform.

Table 3. Curve-fitting results of the k^3-weighted Co K-edge EXAFS data for PdCoAl-GD.

Sample	Shell	CN	R / Å	σ^2 / 10^4 nm^2
PdCoAl-GD*	Co–O	3.8 ± 0.9	1.96 ± 0.01	0.37±0.19
	Co–Al	7.7 ± 2.0	3.37 ± 0.08	0.89±2.80
	Co–O	7.7 ± 2.0	3.40 ± 0.08	0.39±2.43
	Co–Co	2.6 ± 0.7	3.51 ± 0.08	0.63±1.31

*ΔE = 1.99 eV, R_{factor}=4%.

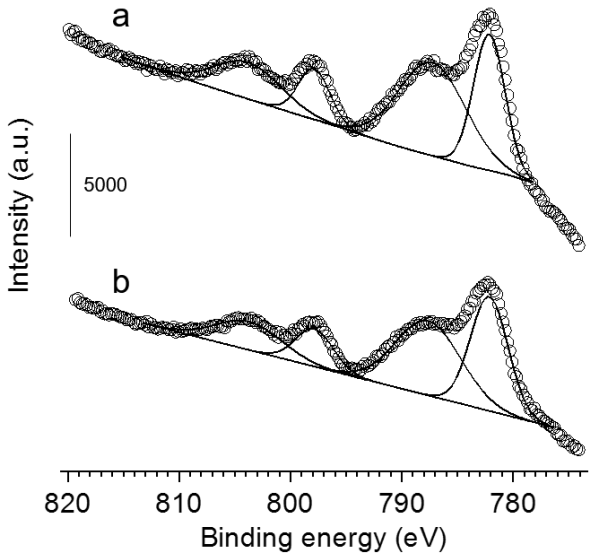

Figure 7. Ex situ Co 2p XPS spectra of: (a) PdCoAl-GD and (b) PdCoAl-SI after methane combustion at 600 °C.

Figure 8 shows HAADF-STEM and EDX elemental mapping images of PdCoAl-GD, PdCoAl-SI and PdAl-I. The white contrast in the HAADF-STEM images was produced by the Pd nanoparticles, while the green, yellow and red regions in the EDX elemental mapping were ascribed to Al, Co and Pd, respectively. In the case of PdCoAl-GD and PdCoAl-SI, the Co species were mainly overlapped with those of Al. According to the Co K-edge XAFS spectra, PdCoAl-GD and PdCoAl-SI possessed a $CoAl_2O_4$ phase dispersed overγ-Al_2O_3. In the case of PdCoAl-GD, Pd species with a size of 2–7 nm were detected overlapping with Al and Co species. Since GD proceeds upon contact between a Pd precursor and reduced Co species, Pd nanoparticles were deposited onto $CoAl_2O_4$ species. The Pd size distributions were obtained by analyzing the HAADF-STEM images (Figure 8). The average Pd particle size calculated by STEM was in rough agreement with that estimated by CO chemisorption (Table 1) However, the enhanced activity cannot be explained only by characterizing the catalyst before methane combustion. A detailed analysis of the state of Pd during reaction is necessary.

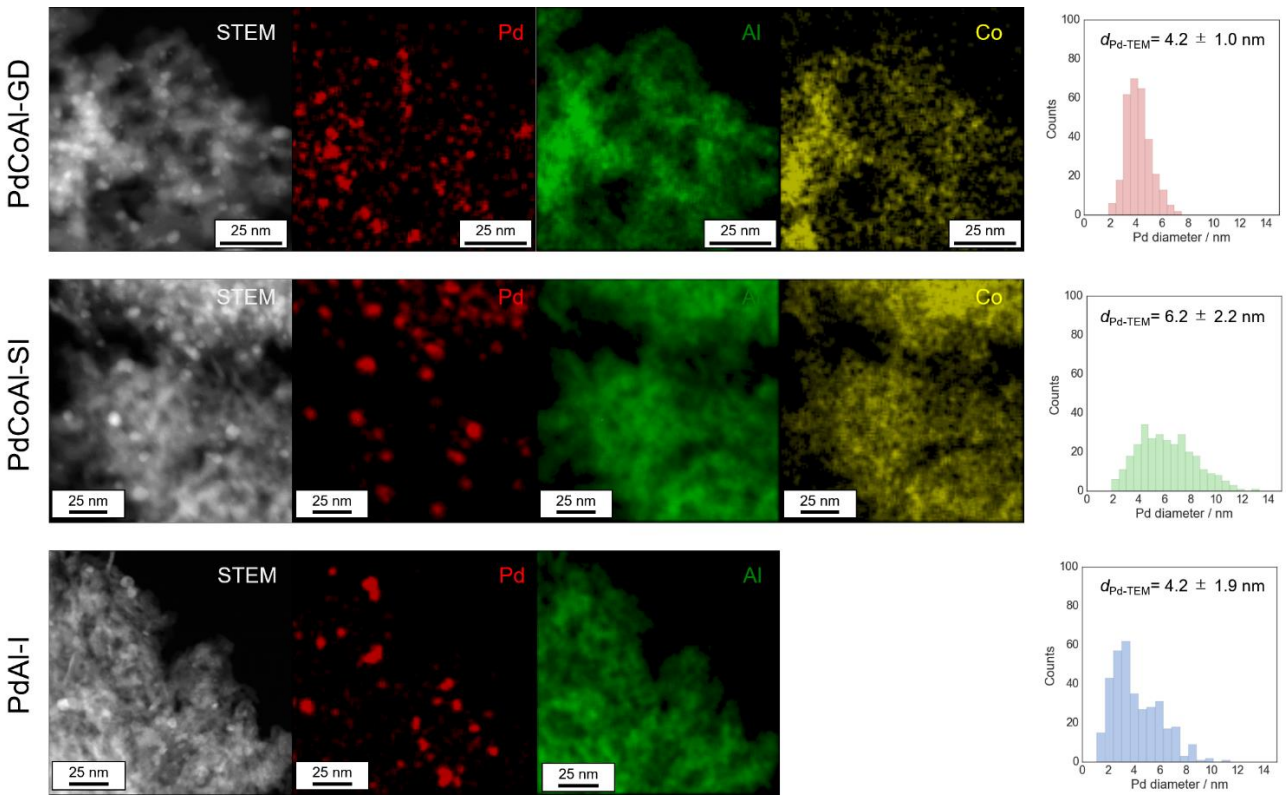

Figure 8. HAADF-STEM images, EDX element mapping, and Pd particle size histograms for PdCoAl-GD, PdCoAl-SI, and PdAl-I.

Operando Pd K-edge XAFS Measurements

We performed operando Pd K-edge XAFS measurements to clarify the Pd oxidation state during methane combustion. The samples were analyzed at the same conditions used for the catalytic tests including a H_2 pretreatment (see Figure 1). Figure 9 shows a series of normalized Pd K-edge XANES spectra of PdCoAl-GD. First, after the oxidation pretreatment, Pd was in form of PdO (Figure 9(b)). Pd was subsequently reduced to Pd^0 after the H_2 pretreatment (Figure 9(c)). Pd was slightly oxidized when contacted with flowing reaction gases at 200 °C (Figure 9(d)). The fraction of PdO gradually increased with temperature until complete oxidation of Pd. Similar operando XAFS measurements were conducted for PdCoAl-SI and PdAl-I (Figure 10, 11). All Pd K-edge XANES spectra were described with a linear combination fitting (LCF) of two XANES spectra (i.e., the one obtained after oxidation at 500 °C (Figure 9(b)), and that obtained after reduction at 500 °C (Figure 9(c)). The amount of PdO (PdO ratio) in the catalysts was estimated using LCF. During the XAFS measurements, the outlet gases were analyzed by MS, and the CH_4 conversion was calculated with the reaction temperature. Figures 10(a)–(c) show the PdO ratio and CH_4 conversion values under reaction for PdCoAl-GD, PdCoAl-SI and PdAl-I. In the case of PdCoAl-GD, the CH_4 conversion increased with the PdO ratio (900 s, reaction temperature: 275 °C). A similar trend was found for PdCoAl-SI and PdAl-I, although CH_4 conversion and PdO formation were observed at higher temperatures. Moreover,

we performed operando XAFS studies for several Pd/Al_2O_3 catalysts having different catalytic activities (Table 4 and Figure 12). As shown in Figure 13(d), the relationship between T_{10} and the PdO ratio at 310 °C was roughly linear for all the catalysts. The catalysts with higher PdO contents showed lower T_{10} values. Considering the operando XAFS measurements above described, PdO was the main active species. Thus, the low light-off temperature of PdCoAl-GD can be ascribed to the oxidation of Pd^0 to PdO at low temperatures.

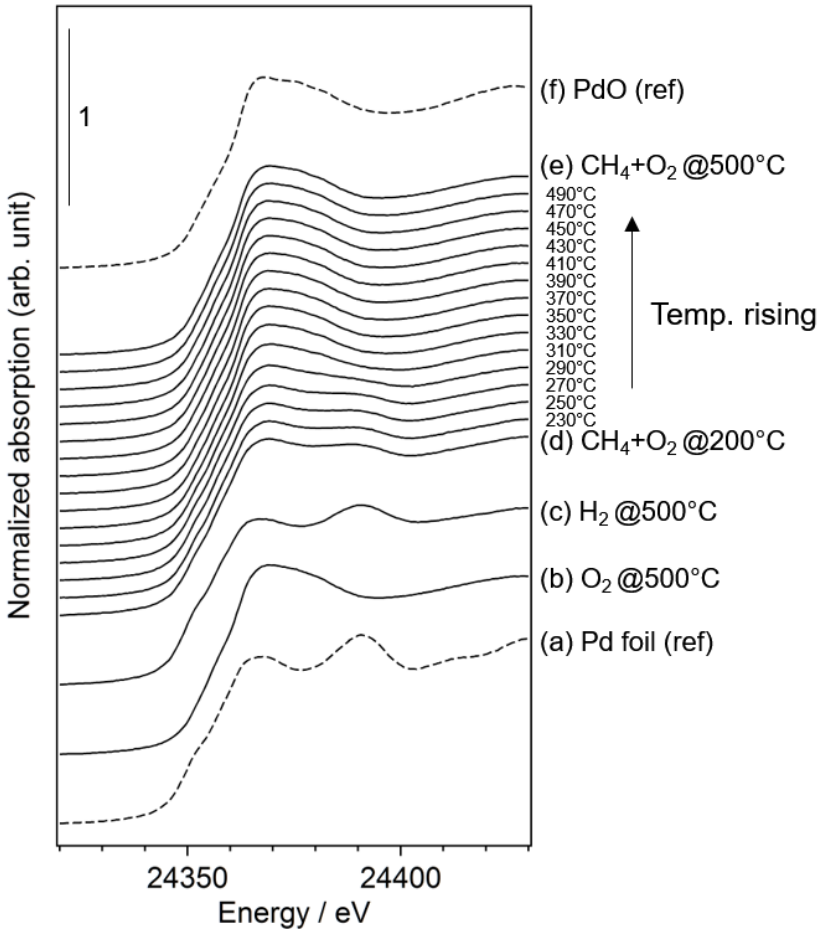

Figure 9. Normalized Pd K-edge XANES spectra of: (a) Pd foil as a reference; (b–e) results for PdCoAl-GD under operando XAFS measurements; (f) PdO as a reference.

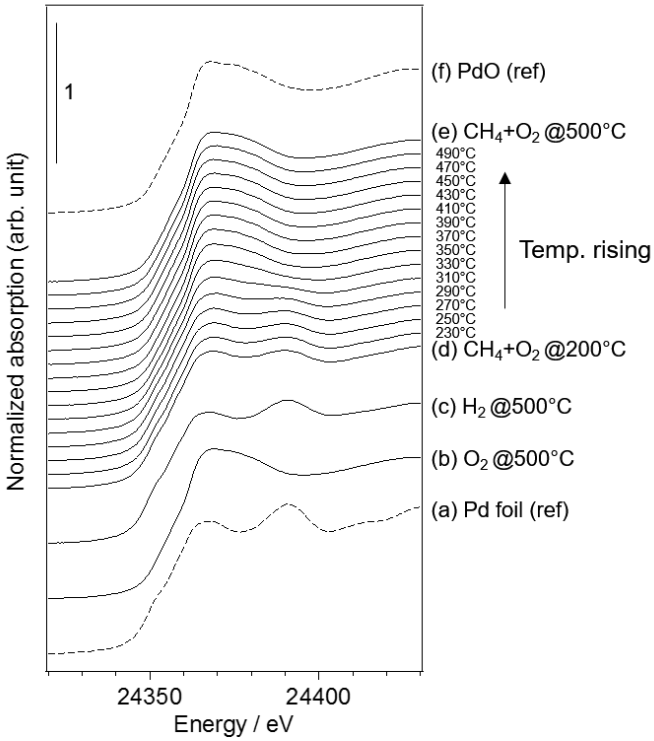

Figure 10. Normalized Pd K-edge XANES spectra of PdCoAl-SI during operando XAFS measurements.

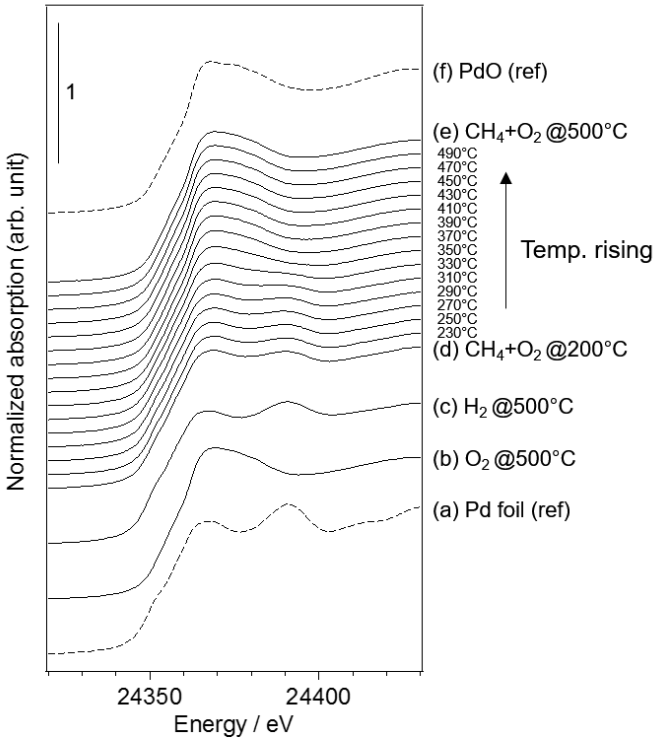

Figure 11. Normalized Pd K-edge XANES spectra of PdAl-I during operando XAFS measurements.

Table 4. List of Pd/Al_2O_3 and $Pd/Co/Al_2O_3$ catalysts with different supports.

Catalysts	Support	preparation method	Calcination	Pd loading (wt%)	Co loading (wt%)	$d_{Pd\text{-}CO}$ (nm)
Pd/ALO2	JRC-ALO-2	Impregnation	500°C for 3 h	2[a]	-	2.7
Pd/ALO5	JRC-ALO-5	Impregnation	500°C for 3 h	2[a]	-	2.8
Pd/ALO8	JRC-ALO-8	Impregnation	500°C for 3 h	2[a]	-	4.7
Pd/ALO8-800A	JRC-ALO-8	Impregnation	800°C for 10 h	2[a]	-	7.1
$Pd/Co_3O_4/Al_2O_3$	Al_2O_3(sasol)	Sequential Impregnation	500°C for 3 h	2[a]	5[a]	3.7

[a] Nominal value.

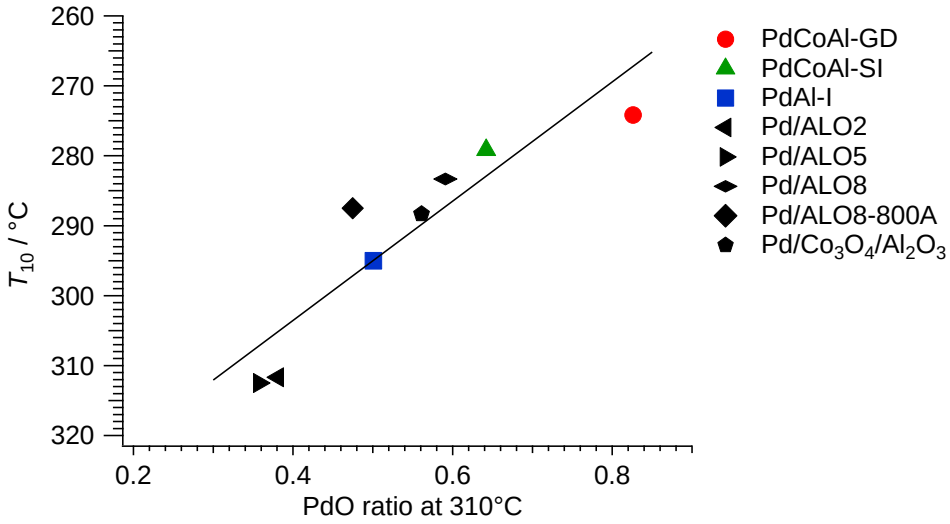

Figure 12. Correlation between T_{10} and the PdO ratio for Pd-based catalysts. The catalysts are listed in Table 4.

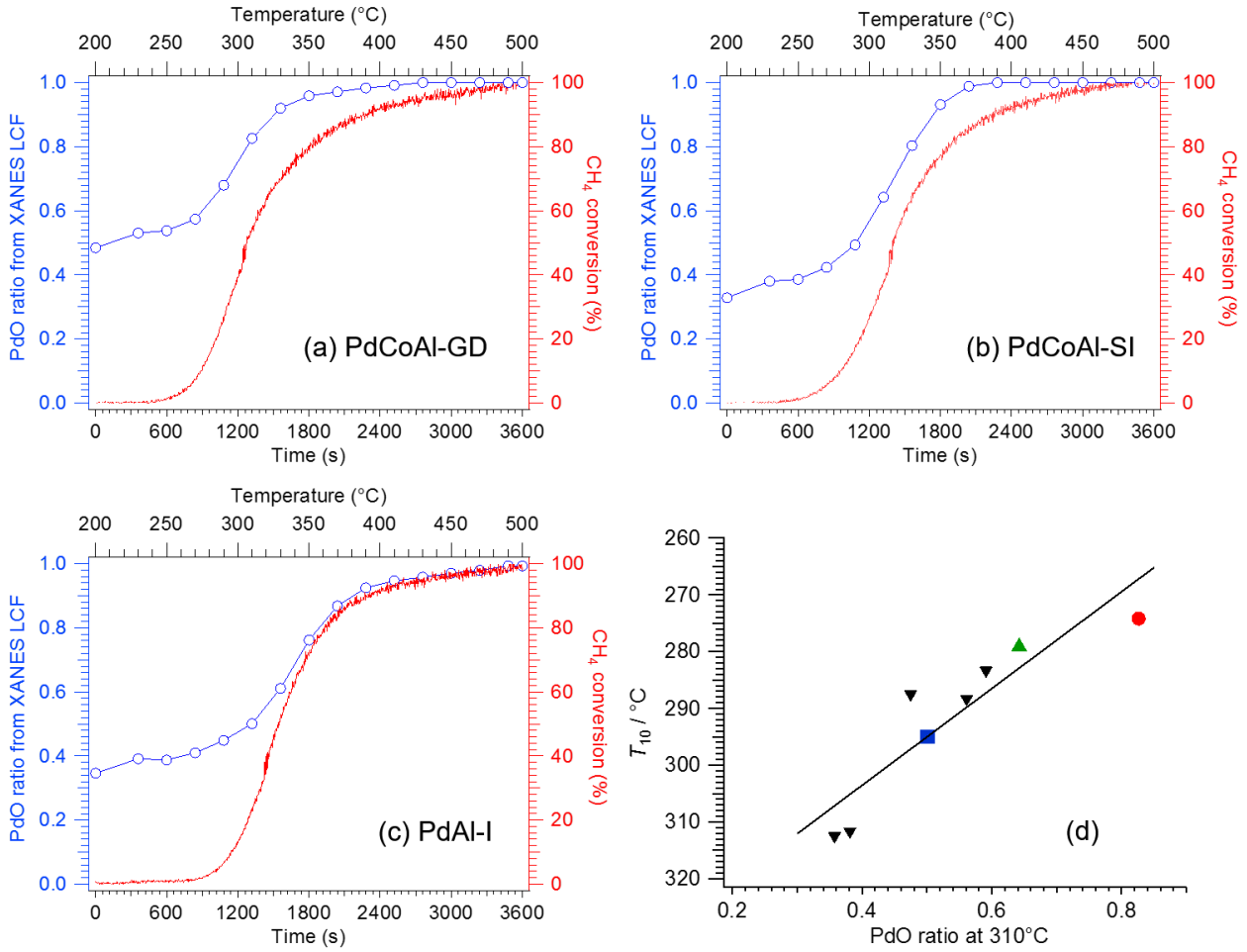

Figure 13. PdO ratio and CH_4 conversion as a function of time for: (a) PdCoAl-GD, (b) PdCoAl-SI and (c) PdAl-I during operando XAFS measurements. (d) Correlation between T_{10} and the PdO ratio at 310 °C over Pd-based catalysts. Red circle: PdCoAl-GD; green triangle: PdCoAl-SI; blue square: PdAl-I; black down-pointing triangle; series of Pd/Al_2O_3 (see Table 4).

Methane Combustion over PdO State Catalysts

As indicated in the previous section, the main active species for this reaction is PdO. This result led us to make the following question: What would happen if Pd was initially in form of PdO? Would the catalysts show similar catalytic activities?

Figure 14 shows the methane combustion results of the catalysts previously treated with O_2 with the aim to oxidized Pd to PdO. Although Pd was initially as PdO, PdCoAl-GD showed the highest activity among all the catalysts tested. When Pd was initially as Pd^0, PdCoAl-SI and PdAl-I showed different trends above 300 °C (Figure 1) in virtue of their Pd particle size (6.3 vs. 3.8 nm, respectively). Pd was gradually oxidized during the catalytic tests such that PdO was main active species in this reaction. Since the Pd surface area of PdCoAl-SI was lower than that of PdAl-I, the former material was considered to have lower Pd oxidation rates. As indicated in Figure 14, the activity of the catalysts

having PdO as the initial phase followed the trend PdCoAl-GD > PdCoAl-SI > PdAl-I in all the temperature ranges.

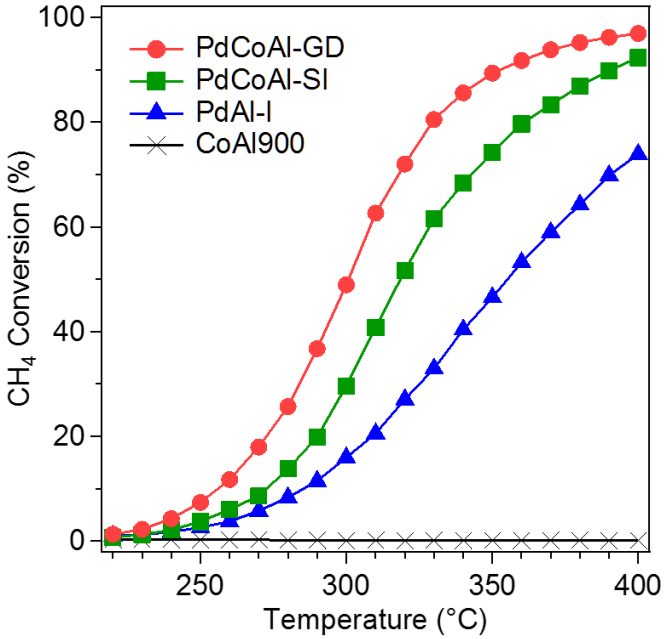

Figure 14. (a) Methane combustion light-off curves of: PdCoAl-GD, PdCoAl-SI, PdAl-I and CoAl900. Pretreatment: flowing O_2 at 500 °C.

The rate-limiting step for methane combustion on PdO is the activation of the C–H bond in CH_4 that takes place at the beginning of the reaction.[44,45] In this step, the PdO surface is partially reduced by the CH_4 molecule. Thus, to investigate the reducibility of PdO, CH_4-TPR measurement was conducted shown as Figure 15. The PdO nanoparticles of PdCoAl-GD were reduced by CH_4 at a lower temperature as compared to PdCoAl-SI and PdAl-I (by 14 and 23 °C, respectively). This trend was similar to that of the catalytic activities (Figure 14). The CH_4-TPR results indicated the activity of PdO toward the activation of the C–H bond was improved in PdCoAl-GD as compared to PdCoAl-SI and PdAl-I. This enhancement can be explained as follows. According to the Pd 3d XPS results, the signal corresponding to PdO species in PdCoAl-GD was shifted to lower binding energies as compared to PdCoAl-SI and PdAl-I (see Figure 16 and Table 5). Thus, the contact of PdO and $CoAl_2O_4$ can alter the electron states of PdO, resulting in enhanced C–H activation.

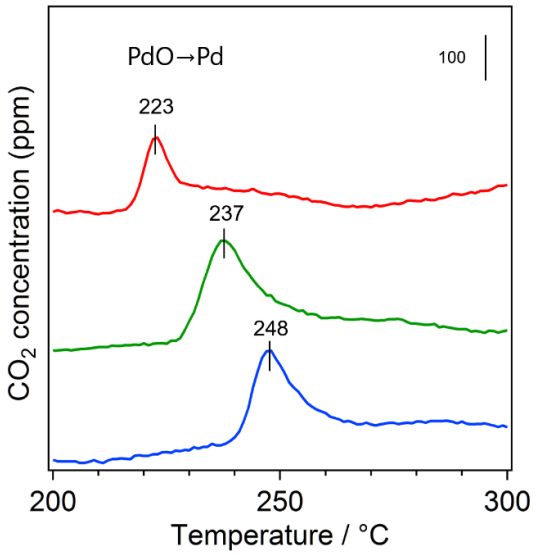

Figure 15. CH_4-TPR results for: PdCoAl-GD (red), PdCoAl-SI (green) and PdAl-I (blue).

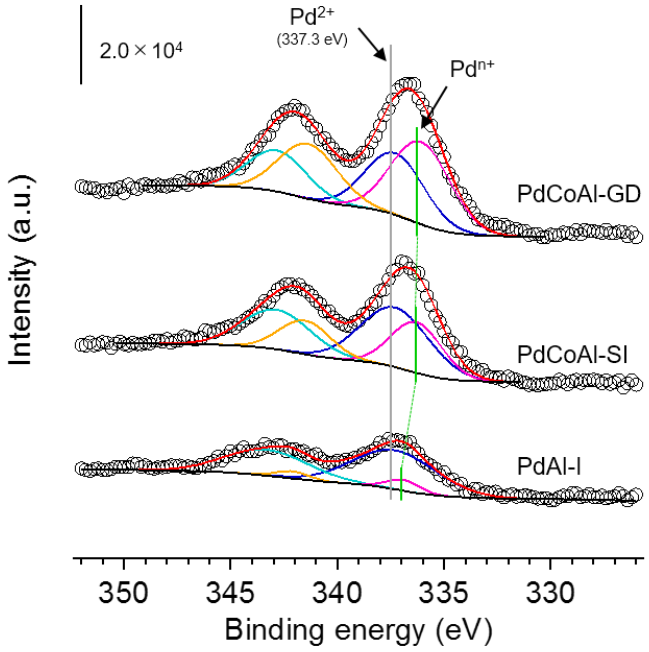

Figure 16. Pd 3d XPS spectra of PdCoAl-GD, PdCoAl-SI, and PdAl-I.

Table 5. Pd^{n+} $3d_{5/2}$ binding energies for the catalysts.

Samples	Pd^{n+} $3d_{5/2}$ B.E. (eV)
PdCoAl-GD	336.1
PdCoAl-SI	336.3
PdAl-I	336.9

4-4. Conclusion

$Pd/CoAl_2O_4/Al_2O_3$ catalysts prepared by a GD method (PdCoAl-GD) showed high activity toward the methane combustion reaction. PdCoAl-GD was comprised of a $CoAl_2O_4$ phase on γ-Al_2O_3 and dispersed Pd nanoparticles of 2–7 nm in size on a $CoAl_2O_4$ phase. Operando XAFS measurements revealed that the light-off temperature decreased for the PdO phase (i.e., the main active species) generated at lower temperatures. Furthermore, PdCoAl-GD showed the highest methane combustion activity among the catalysts tested herein even when PdO was initially present on the catalysts. As revealed by CH_4-TPR, PdO in PdCoAl-GD was reduced at low temperatures by CH_4. PdO species of the catalyst prepared by GD method were effective in activating the C–H bond of CH_4. GD is a simple preparation method comparable to conventional impregnation approaches. Thus, further research on the industrial applications of GD catalysts and mechanism elucidation should be carried out.

4-5. References

1 Choudhary, T., Banerjee, S. & Choudhary, V. *Appl. Catal., A* **234**, 1-23, (2002).

2 Gélin, P. & Primet, M. *Appl. Catal., B* **39**, 1-37, (2002).

3 Farrauto, R. J. *Science* **337**, 659-660, (2012).

4 Farrauto, R. J., Hobson, M., Kennelly, T. & Waterman, E. *Appl. Catal., A* **81**, 227-237, (1992).

5 Burch, R. & Loader, P. *Appl. Catal., B* **5**, 149-164, (1994).

6 Widjaja, H., Sekizawa, K., Eguchi, K. & Arai, H. *Catal. Today* **35**, 197-202, (1997).

7 Lyubovsky, M. & Pfefferle, L. *Appl. Catal., A* **173**, 107-119, (1998).

8 Sekizawa, K., Widjaja, H., Maeda, S., Ozawa, Y. & Eguchi, K. *Appl. Catal., A* **200**, 211-217, (2000).

9 Pieck, C. L., Vera, C. R., Peirotti, E. M. & Yori, J. C. *Appl. Catal., A* **226**, 281-291, (2002).

10 Zhu, G., Han, J., Zemlyanov, D. Y. & Ribeiro, F. H. *J. Am. Chem. Soc.* **126**, 9896-9897, (2004).

11 Simplício, L. M. T., Brandão, S. T., Sales, E. A., Lietti, L. & Bozon-Verduraz, F. *Appl. Catal., B* **63**, 9-14, (2006).

12 Yue, B., Zhou, R., Wang, Y. & Zheng, X. *Appl. Surf. Sci.* **252**, 5820-5828, (2006).

13 Yoshida, H., Nakajima, T., Yazawa, Y. & Hattori, T. *Appl. Catal., B* **71**, 70-79, (2007).

14 Colussi, S. *et al. Angew. Chem. Int. Ed.* **48**, 8481-8484, (2009).

15 Di Carlo, G. *et al. Chem. Commun. (Camb)* **46**, 6317-6319, (2010).

16 Cargnello, M. *et al. Science* **337**, 713-717, (2012).

17 Kinnunen, N. M., Hirvi, J. T., Suvanto, M. & Pakkanen, T. A. *J. Mol. Catal. A: Chem.* **356**, 20-28, (2012).

18 Liu, Y. *et al. Appl. Catal., B* **119-120**, 321-328, (2012).

19 Liu, Y. *et al. Fuel Process. Technol.* **111**, 55-61, (2013).

20 Pan, X., Zhang, Y., Miao, Z. & Yang, X. *J. Energy Chem.* **22**, 610-616, (2013).

21 Stakheev, A. Y. *et al. Top. Catal.* **56**, 306-310, (2013).

22 Guo, G., Lian, K., Gu, F., Han, D. & Wang, Z. *Chem. Commun. (Camb)* **50**, 13575-13577,

(2014).
23 Park, J.-H. *et al. Catal. Commun.* **56**, 157-163, (2014).
24 Ercolino, G. *et al. Catal. Today* **257**, 66-71, (2015).
25 Miller, J. B. & Malatpure, M. *Appl. Catal., A* **495**, 54-62, (2015).
26 Satsuma, A. *et al. Catal. Today* **242**, 308-314, (2015).
27 Shen, J., Hayes, R. E., Wu, X. & Semagina, N. *ACS Catal.* **5**, 2916-2920, (2015).
28 Stefanov, P. *et al. Chem. Eng. J.* **266**, 329-338, (2015).
29 Wu, Z. *et al. J. Catal.* **332**, 13-24, (2015).
30 Lou, Y. *et al. ACS Catal.* **6**, 8127-8139, (2016).
31 Mahara, Y. *et al. Catal. Sci. Technol.* **6**, 4773-4776, (2016).
32 Zou, X., Rui, Z., Song, S. & Ji, H. *J. Catal.* **338**, 192-201, (2016).
33 Chen, Z. *et al. Appl. Catal., A* **532**, 95-104, (2017).
34 Monai, M. *et al. Appl. Catal., B* **202**, 72-83, (2017).
35 Nassiri, H. *et al. ChemPhysChem* **18**, 238-244, (2017).
36 Wang, Z. *et al. Catal. Today* **281**, 467-476, (2017).
37 Zou, X., Rui, Z. & Ji, H. *ACS Catal.* **7**, 1615-1625, (2017).
38 Monai, M. *et al. Appl. Catal., B* **197**, 271-279, (2016).
39 Senftle, T. P., van Duin, A. C. T. & Janik, M. J. *ACS Catal.* **7**, 327-332, (2016).
40 Mahara, Y. *et al. Chem. Lett.* **43**, 910-912, (2014).
41 Mahara, Y., Ishikawa, H., Ohyama, J., Sawabe, K. & Satsuma, A. *Catal. Today* **265**, 2-6, (2016).
42 Ohyama, J., Ishikawa, H., Mahara, Y., Nishiyama, T. & Satsuma, A. *Bull. Chem. Soc. Jpn.* **89**, 914-921, (2016).
43 Wang, H. *et al. Nat. Commun.* **6**, 7181, (2015).
44 Chin, Y. H., Buda, C., Neurock, M. & Iglesia, E. *J. Am. Chem. Soc.* **135**, 15425-15442, (2013).
45 Chin, Y.-H., García-Diéguez, M. & Iglesia, E. *J. Phys. Chem. C* **120**, 1446-1460, (2016).

Chapter 5
Time-Resolved in situ DXAFS Revealing Highly Active Species of Pd Nanoparticle Catalyst for CH_4 Oxidation

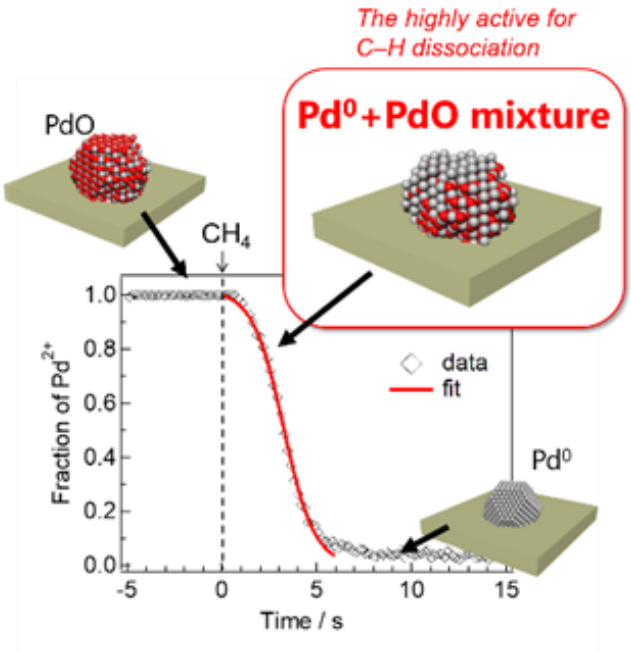

The truly active species of Pd/Al_2O_3 catalysts used for methane combustion was predicted by time-resolved in situ dispersive X-ray absorption fine structure (DXAFS) spectroscopy. By using CH_4 as a reduction agent, PdO in Pd/Al_2O_3 is reduced in 2-step model involving generation of Pd^0 nucleation and growth of Pd^0 domain in a PdO particle. Kinetic analysis of the 2-step model reduction of PdO nanoparticles leads to a suggestion that PdO-Pd^0 pair is the highly active site for methane combustion.

Contents

5-1. Introduction

Redox of supported metal nanoparticle catalysts is a key descriptor for catalytic activity, selectivity, and lifetime for oxidation reaction. To elucidate the redox behavior of nanoparticles under reaction conditions is significant for the development of a high efficiently catalyst system.

Alumina-supported Pd catalysts (Pd/Al_2O_3) have been used to reduce automotive exhaust gases by complete oxidation of methane, propane, and carbon monoxide.[1,2] Among them, methane is the most difficult to burn, and further improvement of Pd catalysts is demanded to lower temperature of methane combustion. Aiming to obtain catalyst design for enhancement of combustion activity, many efforts have been recently devoted to elucidate the reaction mechanism and highly active species on Pd/Al_2O_3. Detailed experiments using labeled ^{18}O showed that methane combustion proceeds according to the Mars and Van Krevelen mechanism.[3,4] Surface lattice oxygen of PdO nanoparticles reacts with CH_4 associating with dissociation of C–H bond, and the PdO surface is immediately re-oxidized by O_2 under reaction temperatures. The rate-determining step of methane combustion is supposed to be a dissociation of C–H bond of CH_4 on PdO surface. Actually, there is a linear relationship between a light-off temperature of methane combustion and the peak top position of CH_4 temperature programmed reduction (CH_4-TPR) for supported catalysts: The PdO species reduced by CH_4 easily is highly active for methane combustion.[5,6] Considering the oxidation state of Pd, PdO is more active species for CH_4 dissociation than metallic Pd (Pd^0).

On the other hand, some paper suggests that the presence of both Pd^0 and PdO is the key of high activity.[7-12] *Lyubovsky* and co-worker argued that partially reduced PdO containing Pd^0 exhibits high activity by compatibly achieving low activation energy on PdO and high preexponential factor due to Pd^0.[7,8] Since then, the oxidation state and catalytic structure of PdO nanoparticles during the reaction have been examined by kinetics,[13-15] transmission electron microscopy (TEM),[9,16,17] and X-ray absorption fine structure (XAFS).[11,18,19] *Miller* and co-worker also suggests that PdO-Pd* site pairs are directly linked to the catalytic activities.[12] However, the truly active species in methane combustion has yet to be specified under reaction conditions.

XAFS spectroscopy is a powerful technique for investigating oxidation state and catalytic structure of supported metal catalysts. Time-resolved XAFS technique such as dispersive XAFS (DXAFS) spectroscopy allows us to observe time course of oxidation state of supported metal catalysts under reaction conditions.[20-28] There are several studies that observed the oxidation state of Pd species in methane combustion *in-situ* under gas flow condition.[11,18,19] However, the usual in-situ XAFS experiment under gas flow conditions does not afford intrinsic redox kinetics due to gas diffusion limitation. To our knowledge, there is no studies that have revealed intrinsic redox behavior of Pd species under actual reaction temperature and atmosphere. In this study, the intrinsic reduction kinetics of supported PdO species by CH_4 was first revealed using DXAFS. The kinetics offers the methane oxidation mechanism and highly active species of Pd/Al_2O_3.

5-2. Experimental

Catalyst preparation

Alumina-supported Pd catalyst (Pd/Al_2O_3) was prepared by a conventional impregnation method using a $Pd(NO_3)_2$ solution and Al_2O_3. Pd loading was adjusted to 2 wt%. Al_2O_3 was prepared by thermal decomposition of boehmite at 500 °C for 1 h. Al_2O_3 was impregnated with a 4.5 wt% $Pd(NO_3)_2$ solution, and stirred for 1 h. After the evaporation of the mixture, the obtained solid was dried and calcined in air at 500 ºC for 3 h. 4.5 wt% $Pd(NO_3)_2$ aqueous solution and high purity boehmite (99%) were supplied from Cataler Corporation and SASOL, respectively.

Characterization

2 wt% Pd/Al_2O_3 were characterized by X-ray diffraction (XRD), CO chemisorption, high-angle annular dark-field scanning transmission electron microscopy (HAADF-STEM), and in situ dispersive X-ray absorption fine structure (DXAFS) spectroscopy.

The XRD patterns of Al_2O_3 and Pd/Al_2O_3 were measured by a Rigaku MiniFlex II/AP diffractometer with a Cu Kα radiation. All samples were measured after preparation without performing any pretreatment. CO chemisorption was carried out on a BELCAT (Bel Japan Inc.). The amount of CO chemisorption was measured by 5 % CO/He pulses after oxidation (100% O_2 at 500 °C) and reduction (100% H_2 at 50 °C) pretreatments. The Pd particle size was estimated assuming that CO was adsorbed on the surface Pd at Pd:CO=1:1 stoichiometry and reduced Pd formed a hemispherical model. HAADF-STEM images of Pd/Al_2O_3 were recorded by JEM-ARM200F Cs-corrected microscope operating at 200 kV. HAADF-STEM images and energy dispersive X-ray (EDX) images were collected using a JEOL JEM-2100F microscope operating at 200 kV. For TEM analysis, the pretreated catalysts were dispersed in methanol and dropped onto a Cu mesh provided with a carbon microgrid.

Time-resolved in situ DXAFS Measurement

In order to observe the reduction behavior of PdO nanoparticles with CH_4, the experiment using the apparatus of Fig. 1(a) was carried out by the procedure of Fig. 1(b). He, O_2, H_2, and 5 vol% CH_4/He were allowed to flow into the gas line to observe reduction behavior of PdO species in Pd/Al_2O_3 by CH_4. Here, a batch-type in situ XAFS cell with an inner volume of 200 mL was used, which allows instantaneous injection of CH_4 gas by evacuating the cell before injection of CH_4. Here, detailed procedures are shown below for the experiments I and II in Fig. 1(b) at 400 °C.

I. DXAFS measurement for completely reduced Pd/Al_2O_3 (Pd/Al_2O_3-Red) and oxidized Pd/Al_2O_3 (Pd/Al_2O_3-Ox)

100 mg of sample (2wt% Pd/Al_2O_3) was weighed and mold for 5 MPa to give a pellet with a 1 cm diameter. The sample were placed in a batch-type in situ XAFS cell. After we opened 2-way cock ①, valve controller ②, and ③, the sample was reduced by 100 % H_2 with a 50 mL/min at 400°C

for 10 min. After He purge, DXAFS measurement is performed with Pd K-edge to obtain XAFS spectrum (Pd/Al_2O_3-Red). Thereafter, 100 % O_2 with a 50 mL/min is flowed and oxidized at 600 °C for 10 min. The temperature is lowered to 400 °C, and DXAFS measurement is performed after He purge (Pd/Al_2O_3-Ox). These two XANES spectra were defined as the criteria of Pd^0 and Pd^{2+} in this sample.

II. Time-resolved DXAFS measurement for transient reduction of PdO nanoparticles by CH_4 injection

After experiment I, 2-way cock ④ were opened to evacuate the inside of XAFS cell, gas holder, and gas lines. When the pressure in the XAFS cell reached to 0.9 kPa, valve controller ②, ③, and 2-way cock ④ were closed to shut the XAFS cell. A 5 % CH_4/He with a 1.5 MPa was stored into 50 mL gas holder, and the 2-way cock ① was closed. Pd K-edge DXAFS spectra were obtained with a time resolution of 12 ms. Five second later, valve control ② was opened automatically and the sample reduced by CH_4 injection. Then, the inside pressure reached approximately 65 to 75 kPa.

The above experiment I and II was carried out from 375 °C to 475 °C.

The Pd K-edge XAFS spectra regarding Pd/Al_2O_3-Red and Pd/Al_2O_3-Ox at 375, 400, 425, 450, and 475 °C were measured. The normalization, Fourier transformation, linear combination fitting (LCF), and curve fitting of all XAFS spectra were carried out with Larch based on python. The Pd K-edge EXAFS data were fitted between 3 and 11 $Å^{-1}$ in k space and 1–4 Å in R space. In curve fitting, we have to be careful as there is a trade-off relationship between the coordination number (CN) and Debye Waller factor (σ^2). First, we determined the intrinsic loss factor (S_0^2) from the curve fitting of Pd foil and PdO bulk. Then, in order to estimate the σ^2 at each temperature, a series of standard XAFS spectra of 2 wt% Pd/Al_2O_3 (average Pd particle diameter = 14.4 nm) was analyzed. (These spectra were collected in the process of increasing the temperature under He from RT to 570 °C after H_2 reduction of 2 wt% Pd/Al_2O_3 in advance.) Using a value estimated from the relationship between the temperature and σ^2 for Pd^0, we carried out the curve fitting for EXAFS spectra of Pd/Al_2O_3-Red at 375–475 °C. The series of Pd/Al_2O_3-Ox were analyzed for using a value of σ^2 estimated from analysis for 2 wt% PdO/Al_2O_3.

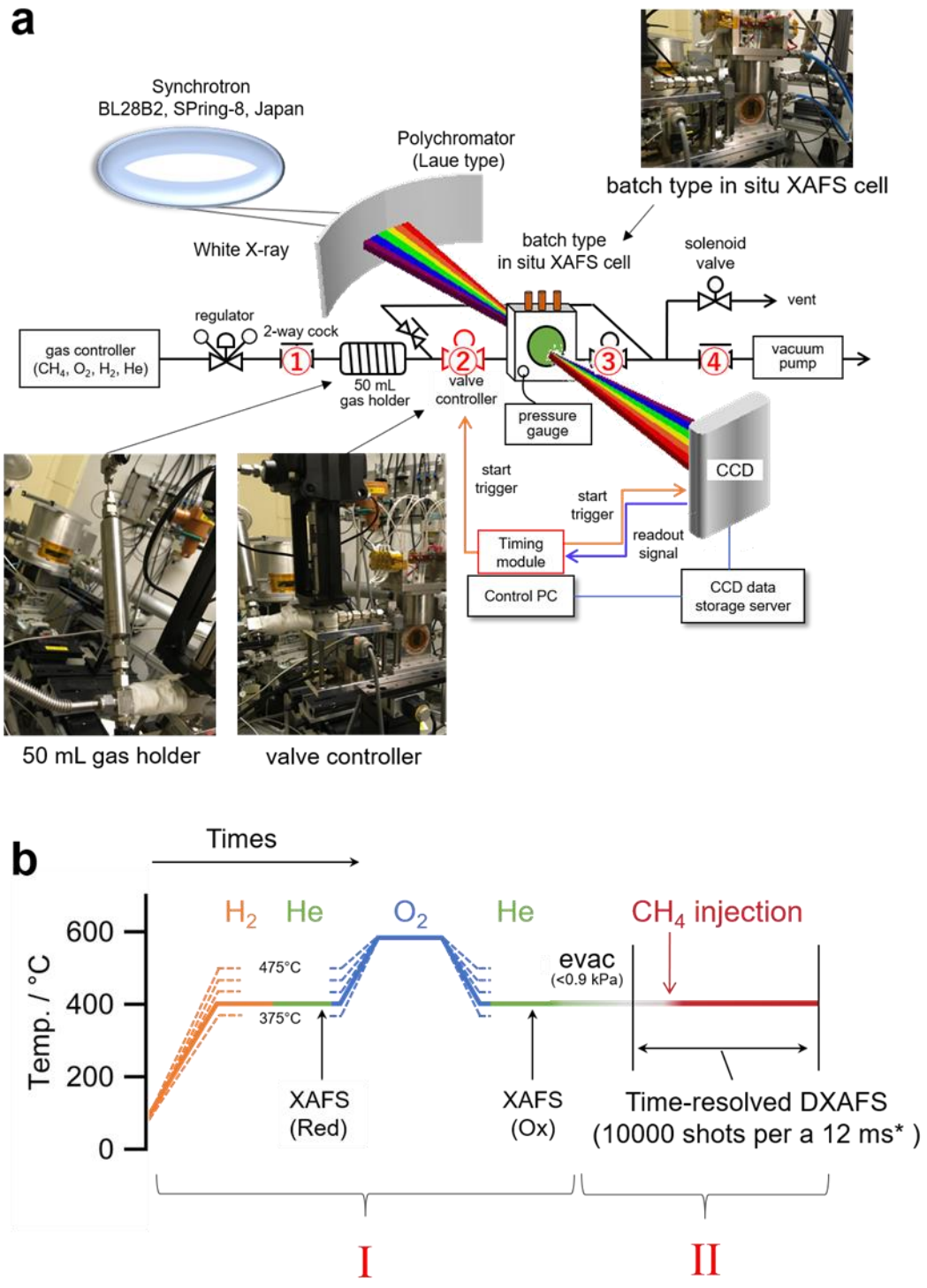

Figure 1. (a) Schematic illustration and representative pictures of experimental apparatus for DXAFS measurements. (b) Experimental procedure of DXAFS measurements for Pd/Al_2O_3 samples.

5-3. Results and Discussion

The Pd/Al_2O_3 catalyst was characterized using X-ray diffraction (Fig. 2), and CO adsorption technique. Both characterization tequnique indicated formation of Pd nanoparticles on γ-Al_2O_3. Actually, the size of Pd nanoparticles calculated from the amount of CO adsorption was 3.8 nm. When analyzed using the high-angle annular dark-field scanning transmission electron microscopy (HAADF-STEM), the Pd particle size of Pd/Al_2O_3-Red and Pd/Al_2O_3-Ox were 3.6 and 3.3 nm, respectively (Fig. 3). This means that the oxidation and reduction treatment hardly change the Pd particle size. Figure 4(a) and (b) show the Pd K-edge X-ray absorption near edge structure (XANES) and Fourier transformed k^3-weighted extended X-ray absorption fine structure (EXAFS) spectra for Pd/Al_2O_3-Red and Pd/Al_2O_3-Ox. XANES of Pd/Al_2O_3-Red almost fits to that of Pd foil, and the Pd-Pd bond was observed on Fourier transformed EXAFS. The results confirms that Pd of Pd/Al_2O_3-Red has completely reduced Pd^0 nanoparticles. On the other hand, XANES of Pd/Al_2O_3-Ox was similar to that of PdO. Only peaks derived from Pd–O and Pd–Pd of PdO nanoparticles were observed and no peak derived from Pd–Pd bond of Pd^0 nanoparticles was observed. Thus, the O_2 treatment completely oxidized Pd of Pd/Al_2O_3-Red to PdO. Here, the two XANES spectra shown in Fig. 4(a) were defined as the criteria of Pd^0 and Pd^{2+} in this sample.

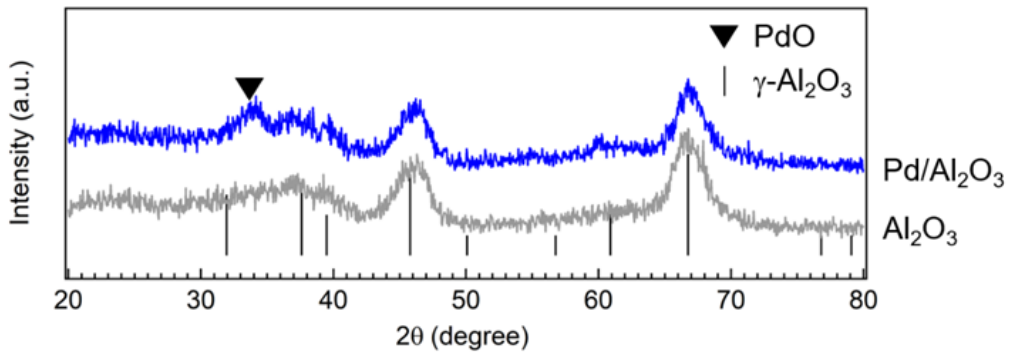

Figure 2. XRD patterns of Pd/Al_2O_3 and Al_2O_3.

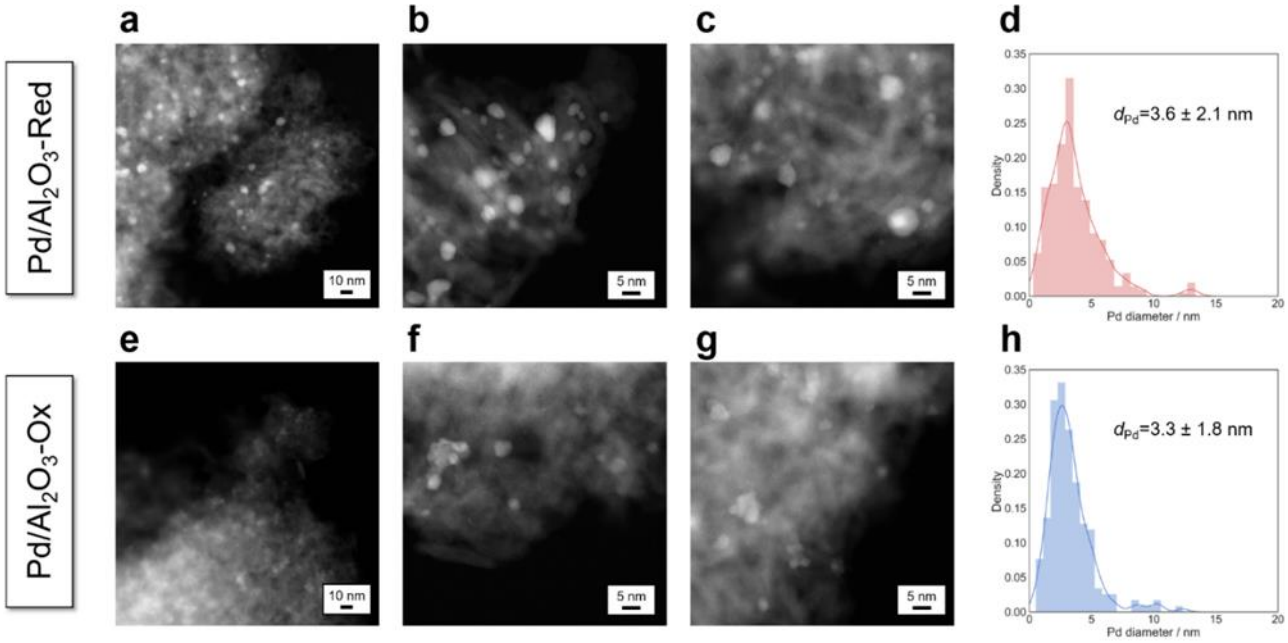

Figure 3. Representative HAADF-STEM images and Pd size distribution for (a–d) Pd/Al_2O_3-Red and (e–h) Pd/Al_2O_3-Ox.

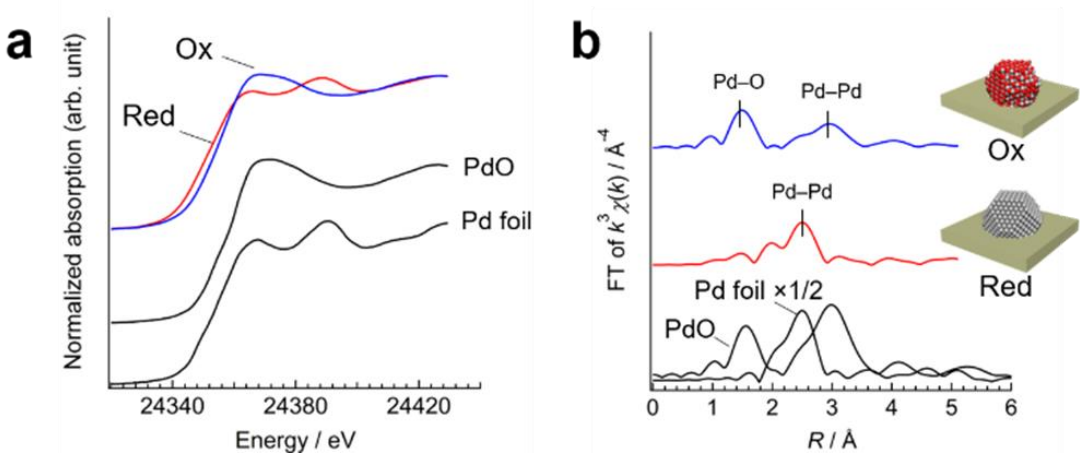

Figure 4. (a) XRD patterns of Pd/Al_2O_3 and Al_2O_3. (a) Pd K-edge XANES spectra and (b) Fourier transformed k^3-weighted Pd K-edge EXAFS spectra of Pd/Al_2O_3-Red, Pd/Al_2O_3-Ox, and references.

Figure 5(a) presents Pd K-edge XANES spectra recorded during reduction of PdO for Pd/Al_2O_3 by CH_4 at 400 °C. The time when CH_4 was instantaneously injected was defined as 0 s. Before introducing CH_4 (−5 – 0 s), the XANES spectra stayed in the same as that of Pd/Al_2O_3-Ox. After CH_4 injection, the XANES spectra of Pd/Al_2O_3-Ox rapidly changed, to that of Pd/Al_2O_3-Red. Since the series of XAFS spectra in Figure 5(a) had isosbestic points as shown in Fig. 5(b), we can express the spectra by linear combination of that of Pd/Al_2O_3-Red and Pd/Al_2O_3-Ox, and determine the fraction of Pd^{2+} and Pd^0 in the Pd/Al_2O_3 using least-squares fitting. Figure 5(c) shows the experimental time

dependence of the proportion of Pd^{2+} in Pd/Al_2O_3 calculated from linear combination fitting (LCF) of Pd K-edge DXAFS spectra. The recorded pressure and the temperature in the XAFS cell are also displayed in Figure 5(c). Before introducing CH_4, all of Pd in Pd/Al_2O_3 was in Pd^{2+} state (that is, PdO), but after CH_4 injection, the proportion of Pd^{2+} decreased. Here, it is noted that there was an induction period of about 2 s after CH_4 injection, and the graph showed sigmoidal-shaped kinetics. As shown in the pressure change of Figure 5(c), the introduction of CH_4 is complete in about 20 ms, and gas diffusion hardly affects the kinetics of Pd^{2+} reduction. After introducing of CH_4, the temperature inside the XAFS cell temporarily dropped by about 8 °C due to the *Joule-Thomson effect*, but the slight decrease of the temperature does not cause the sigmoidal kinetics. Interestingly, this sigmoidal kinetics appeared when CH_4 was used as a reducing agent, but it did not appear at all when CO was used as a reducing agent (Fig. 6). These results mean that the reduction of PdO by CH_4 does not proceed in a simple one step reaction.

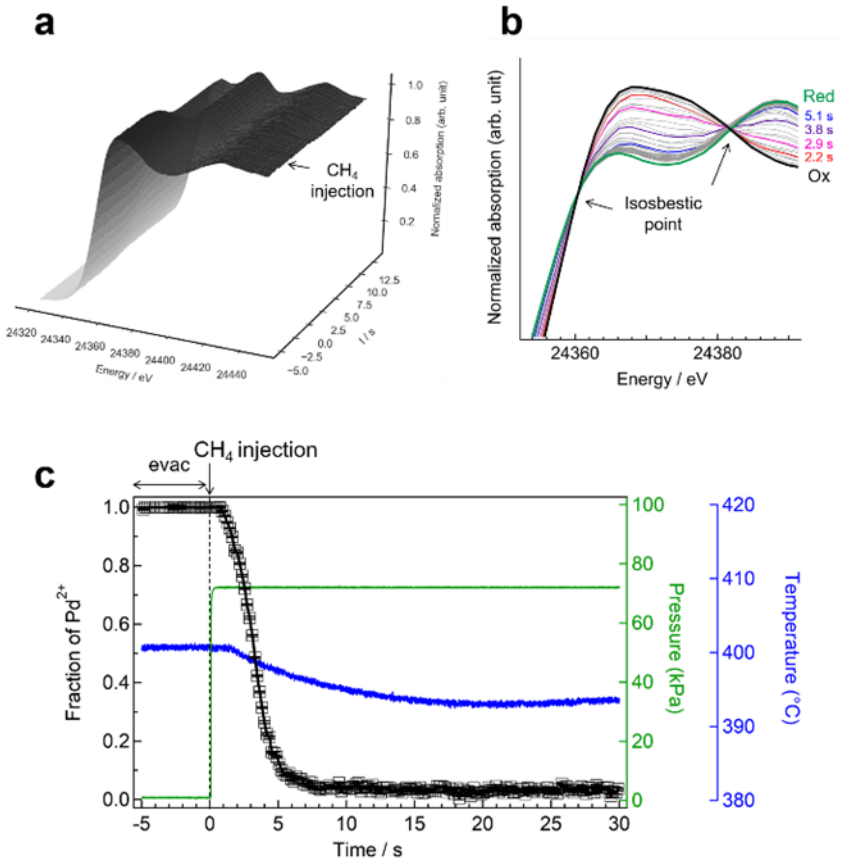

Figure 5. (a) Series of Pd K-edge XANES spectra for transient CH_4 injection into Pd/Al_2O_3. (b) The superimposed XANES spectra. (c) A fraction of Pd^{2+} calculated by using LCF for the series of Pd K-edge XANES spectra, observed pressure and temperature in the XAFS cell as a function of CH_4 exposer times.

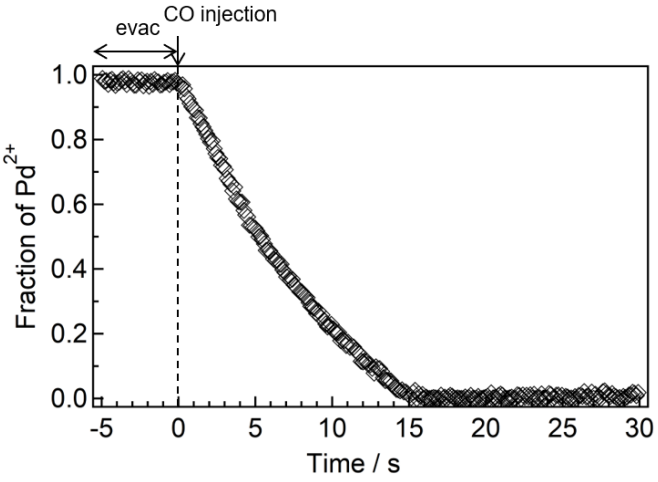

Figure 6. A fraction of Pd^{2+} calculated by using LCF for the series of Pd K-edge XANES spectra as a function of CO exposer times. In the case of PdO reduction by CO, the induction period such as Fig. 5(c) did not observed.

The sigmoidal kinetics has been found in liquid-phase formation of metal nanoparticles by reduction of metal precursors. As a pioneering work, *Watzky*, *Finke* and co-workers reported sigmoidal kinetics in the formation of Ir(0) nanoclusters with H_2 as the reducing agent.[29] The sigmoidal kinetics is also found in the formation of nanoparticles for supported heterogeneous catalysts as reported by *Mondloch* and co-worker.[30-32] In these literature, the formation process of nanoparticles is expressed by 2-step model.

$$n\mathrm{M}^{x+} \xrightarrow{k_1} \mathrm{M}^0{}_n \quad : \text{Nucleation} \tag{1}$$

$$\mathrm{M}^{x+} + \mathrm{M}^0{}_n \xrightarrow{k_2} \mathrm{M}^0{}_{n+1} \quad : \text{Particle Growth} \tag{2}$$

where, the first equation means nucleation of metal ($M^0{}_n$) by reduction of metal precursor (M^{x+}), and the second equation means the particle growth by reduction of M^{x+} on $M^0{}_n$.

This 2-step model is applied to the reduction behavior of PdO particles by CH_4. The reduction of PdO can be expressed by two elemental reactions as R1 and R2 in the following equations.

$$\mathrm{Pd}^{2+} \xrightarrow{k_1} \mathrm{Pd}^0 \quad : \text{Nucleation } (\textit{R1}) \tag{3}$$

$$\mathrm{Pd}^{2+} + \mathrm{Pd}^0 \xrightarrow{k_2} 2\mathrm{Pd}^0 \quad : \text{Particle Growth } (\textit{R2}) \tag{4}$$

Based on the 2-step model, the following eq. (5) is developed.

$$[\mathrm{Pd}^{2+}]_t = \frac{\frac{k_1}{k_2} + [\mathrm{Pd}^{2+}]_0}{1 + \frac{k_1}{k_2}[\mathrm{Pd}^{2+}]_0 e^{(k_1 + k_2[\mathrm{Pd}^{2+}]_0)t}} \quad (5)$$

We performed least squrare fitting of the kinetics in Fig. 5(c) using the eq. (5). Figure 7 shows the fitting results. The rate law for the 2-step model successfully expressed the kinetics of the reduction of PdO by CH_4. The rate constants of the first step (*R1*) and the second step (*R2*) were determined to be k_1=2.23×10^{-2} s^{-1} and k_2=1.28×10^4 L·mol^{-1}·s^{-1}, respectively.

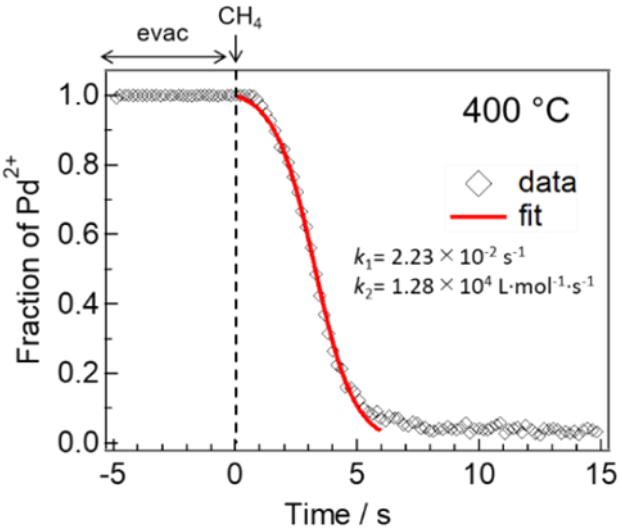

Figure 7. Sigmoidal kinetics for reduction of PdO of Pd/Al_2O_3 by CH_4 at 400 °C (◇), and the fitting result by using eq. (7) derived from 2-step model (red line).

The kinetics of the PdO reduction was analyzed at various temperatures (375–475 °C). Figure 8 showed the XANES spectra for Pd/Al_2O_3-Red and Pd/Al_2O_3-Ox at 375–475 °C. The XANES of all Pd/Al_2O_3-Ox were almost same. Similarly, there was no difference in Pd/Al_2O_3-Red at each temperature. This mean that Pd was completely reduced by H_2, and was also completely oxidized by O_2 at each temperature. Figures 9 and 10 show the results of k^3-weighted EXAFS spectra and curve fitting of Pd/Al_2O_3-Red and Pd/Al_2O_3-Ox, respectively. Table 1 and 2 shows results of fitting data. All EXAFS spectra could be fitted with Pd (*space group: Fm-3m 225*) and PdO (*space group: P4$_2$/mmc 131*) structures. In our results, the CNs of Pd–Pd and Pd–O were almost same even in several temperatures, which guarantees that all DXAFS experiments regarding CH_4 injection at each temperature were performed under the same conditions of Pd nanoparticles.

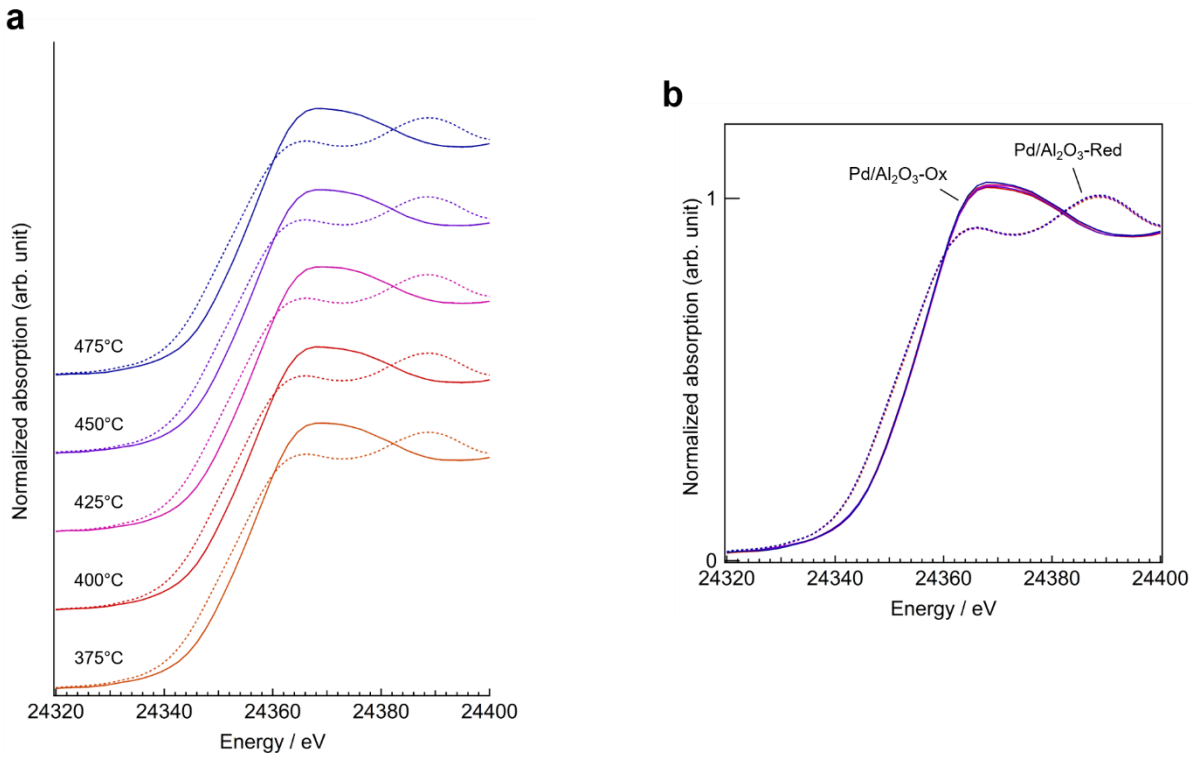

Figure 8. (a) The series of Pd K-edge XANES spectra for Pd/Al_2O_3-Red and Pd/Al_2O_3-Ox at 375–475 °C (sold line: Pd/Al_2O_3-Ox, dotted line: Pd/Al_2O_3-Red). (b) The superimposed graph.

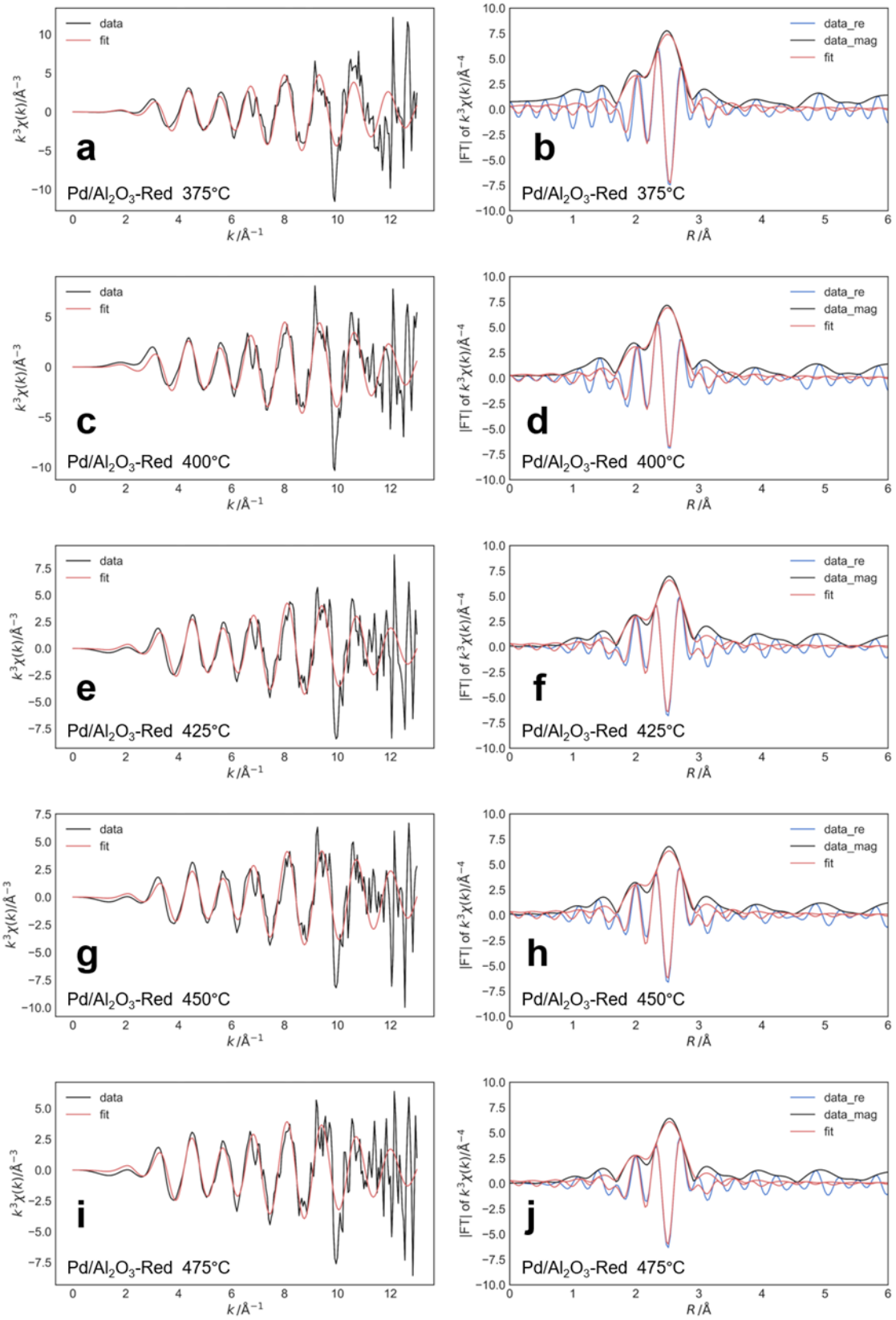

Figure 9. k^3-weighted Pd K-edge EXAFS spectra and Fourier transform for Pd/Al_2O_3-Red at (a, b) 375 °C, (c, d) 400 °C, (e, f) 425 °C, (g, h) 450 °C, and (i, j) 475 °C (black: raw data; red: fitting data; blue: real part of the Fourier transform)

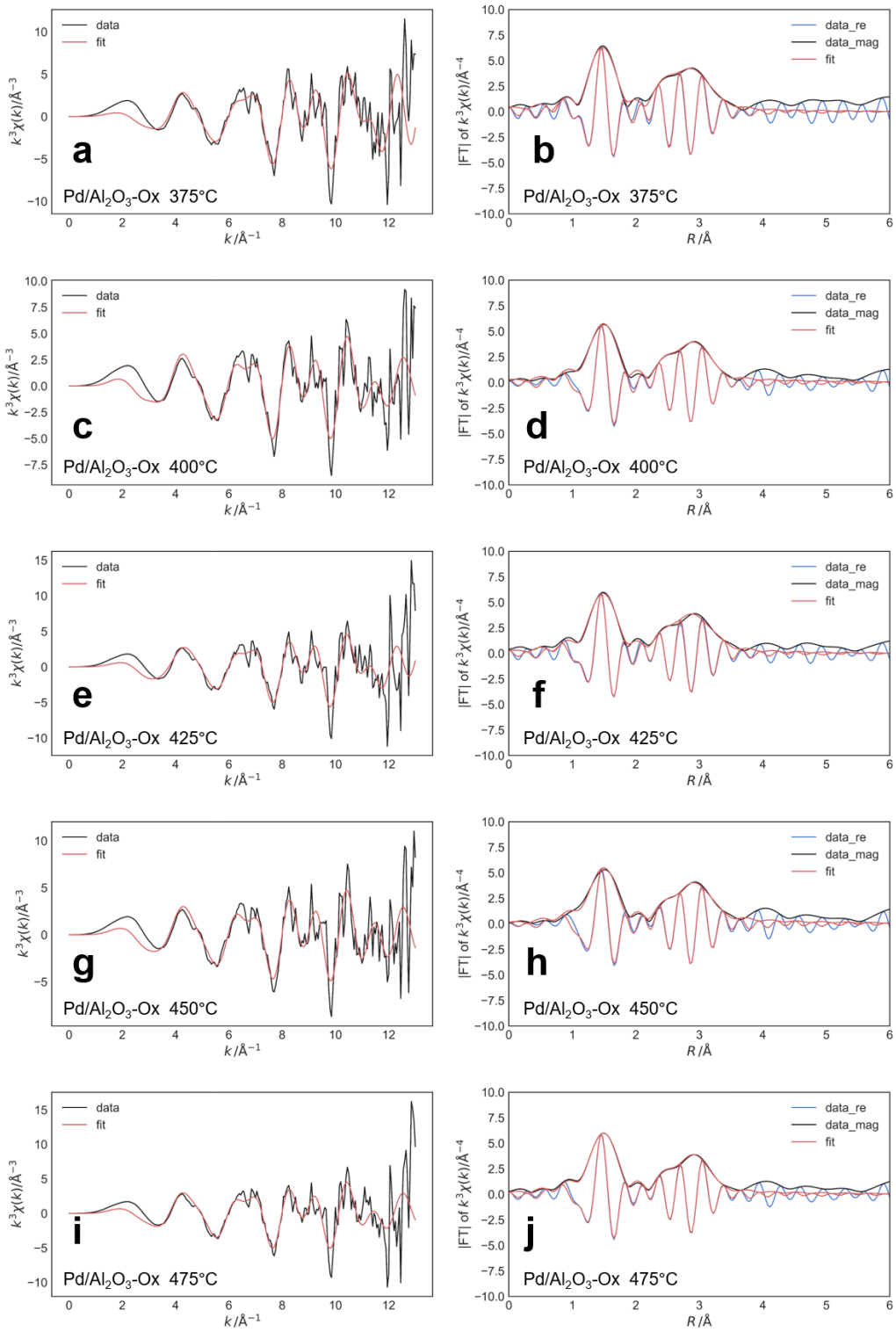

Figure 10. k^3-weighted Pd K-edge EXAFS spectra and Fourier transform for Pd/Al_2O_3-Ox at (a, b) 375 °C, (c, d) 400 °C, (e, f) 425 °C, (g, h) 450 °C, and (i, j) 475 °C (black: raw data; red: fitting data; blue: real part of the Fourier transform).

Table 1. The curve fitting results of Pd K-edge EXAFS spectra for the series of Pd/Al_2O_3-Red.

Sample	Shell	CN	*R*/Å	$\sigma^2/10^4$ nm^2	R_f/%
Pd/Al_2O_3-Red 375 °C	Pd–Pd	7.1±0.8	2.73±0.01	0.9596	4.2
Pd/Al_2O_3-Red 400 °C	Pd–Pd	6.8±0.6	2.73±0.01	0.9904	2.5
Pd/Al_2O_3-Red 425 °C	Pd–Pd	6.5±0.6	2.72±0.01	1.0211	2.8
Pd/Al_2O_3-Red 450 °C	Pd–Pd	6.8±0.7	2.72±0.01	1.0516	3.0
Pd/Al_2O_3-Red 475 °C	Pd–Pd	6.6±0.5	2.72±0.01	1.0816	1.6

Table 2. The curve fitting results of Pd K-edge EXAFS spectra for the series of Pd/Al_2O_3-Ox.

Sample	Shell	CN	*R*/Å	$\sigma^2/10^4$ nm^2	R_f/%
Pd/Al_2O_3-Ox 375 °C	Pd–O	3.1±0.2	1.97±0.01	0.2096 [b]	1.3
	Pd–Pd	1.2±0.1	2.95±0.02	0.3533 [b]	
	Pd–Pd	2.4±0.2 [a]	3.36±0.02	0.3533 [b]	
Pd/Al_2O_3-Ox 400 °C	Pd–O	2.9±0.2	1.99±0.01	0.2184 [b]	1.8
	Pd–Pd	1.1±0.1	2.98±0.03	0.3777 [b]	
	Pd–Pd	2.2±0.2 [a]	3.37±0.02	0.3777 [b]	
Pd/Al_2O_3-Ox 425 °C	Pd–O	3.0±0.1	1.98±0.01	0.2270 [b]	1.0
	Pd–Pd	1.1±0.1	3.00±0.02	0.4005 [b]	
	Pd–Pd	2.2±0.2 [a]	3.38±0.01	0.4005 [b]	
Pd/Al_2O_3-Ox 450 °C	Pd–O	2.8±0.2	1.99±0.01	0.2355 [b]	2.7
	Pd–Pd	1.1±0.1	3.03±0.03	0.4218 [b]	
	Pd–Pd	2.2±0.2 [a]	3.38±0.03	0.4218 [b]	
Pd/Al_2O_3-Ox 475 °C	Pd–O	3.1±0.1	1.99±0.01	0.2439 [b]	1.0
	Pd–Pd	1.1±0.1	3.02±0.02	0.4415 [b]	
	Pd–Pd	2.2±0.2 [a]	3.38±0.02	0.4415 [b]	

Figure 11 shows the kinetics of the PdO reduction by CH_4 at various temperatures. The induction period became shorter with rising the temperature. All recorded kinetics were consistently expressed by the rate equation for 2-step model represented by eq. (5).

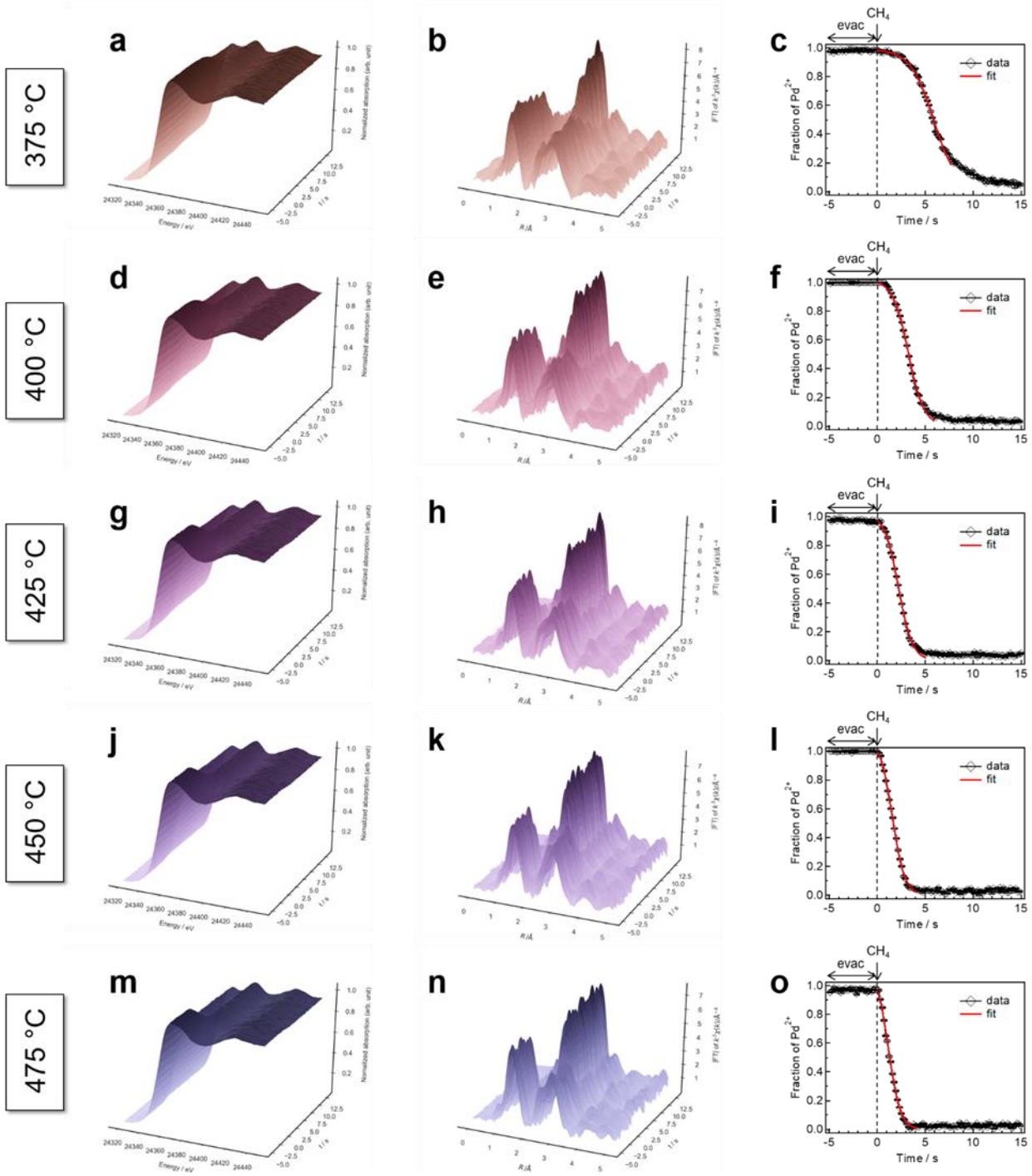

Figure 11. The series of Pd K-edge XANES spectra, Fourier transform k^3-weighted EXAFS, and kinetics for reduction of PdO by CH_4 calculated by using LCF of XANES at (a, b, c) 375 °C, (d, e, f) 400 °C, (g, h, i) 425 °C, (j, k, l) 450 °C, and (m, n, o) 475 °C. The red lines in (c, f, i, l, o) mean the fitting results by using eq. (7) derived from 2-step model.

Figure 12 show the Arrhenius plots of the two steps for PdO reduction by CH_4. The both plots show a linear relationship, and the activation energy of each step (E_{a1} and E_{a2}) is 123±6 kJ/mol and 20±8 kJ/mol, respectively. Since E_{a1} is much higher than E_{a2}, the nucleation of Pd^0 is much slower than the particle growth of Pd^0. Therefore, the reduction of PdO species involves the slow step of Pd^0 nucleation and the following fast step of Pd^0 growth.

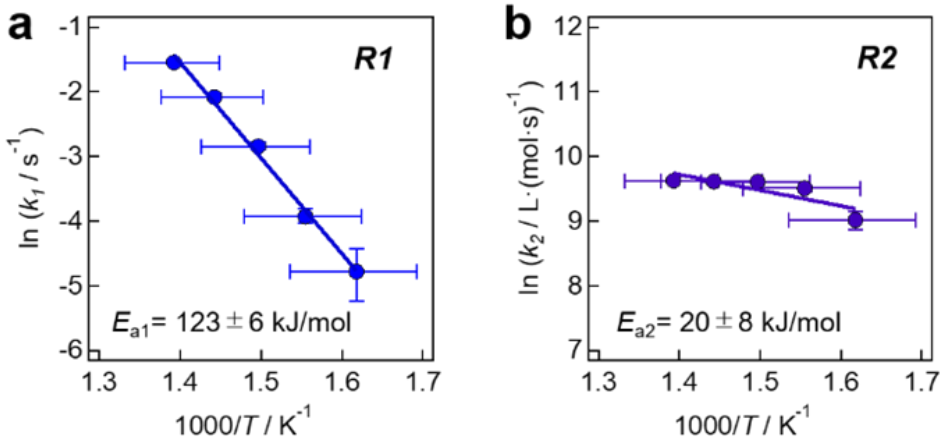

Figure 12. (a) Sigmoidal kinetics for reduction of PdO of Pd/Al_2O_3 by CH_4 at 375–475 °C (black markers and lines), together with fitted curves using the 2-step model equation (red line). (b) Arrhenius plots for the rate constants of Pd^0 nucreation (k_1) and particle growth (k_2) calculated by the fitting . E_{a1} and E_{a2} were calculated from the slope of the Arrhenius plot.

It should be noted that the particle size of PdO is hardly changed even after reduction. Accordingly, one can consider that the observed reduction is an event within a Pd nanoparticle. Please also note that the reduction of PdO accompanies oxidation of CH_4. Thus, the rate of PdO reduction by CH_4 can be related to the rate of CH_4 oxidation. Actually, the E_{a1} (123 kJ/mol) is close to the reported C–H dissociation energy of CH_4 on PdO(100) (131 kJ/mol).[14]

Figure 13 illustrates the reduction of a PdO nanoparticle accompanied by CH_4 oxidation. The reaction is slow on fully oxidized PdO nanoparticles. But, the reaction is accelerated once PdO is partially reduced and mixed with Pd^0. The results indicate that Pd^0-PdO pair sites have much higher activity for CH_4 oxidation than only PdO. Since C–H dissociation of CH_4 is the key step for CH_4 oxidation, one can consider that the Pd^0-PdO pair is highly active for the C-H dissociation.

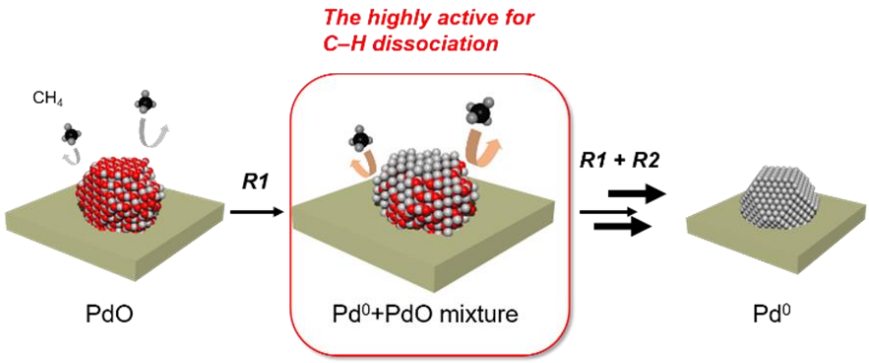

Figure13. Illustration of possible scheme regarding C–H dissociation of CH_4 on PdO nanoparticle.

5-4. Conclusion

Time-resolved in situ DXAFS measurement revealed that the highly active species of Pd Nanoparticle catalysts for methane combustion is PdO-Pd^0 pair site. The PdO nanoparticle were reduced by CH_4 as a 2-step model involving generation of Pd^0 nucleation and growth of Pd^0 domain in a PdO particle. The PdO-Pd^0 pair site accelerates the C–H dissociation associated with PdO reduction.

5-5. References

1 Maillet, T., Solleau, C., Barbier, J. & Duprez, D. *Appl. Catal., B* **14**, 85-95, (1997).

2 Gélin, P. & Primet, M. *Appl. Catal., B* **39**, 1-37, (2002).

3 Machocki, A., Rotko, M. & Stasinska, B. *Catal. Today* **137**, 312-317, (2008).

4 Müller, C. A., Maciejewski, M., Koeppel, R. A., Tschan, R. & Baiker, A. *J. Phys. Chem.* **100**, 20006-20014, (1996).

5 Yang, L.-f., Shi, C.-k., He, X.-e. & Cai, J.-x. *Appl. Catal., B* **38**, 117-125, (2002).

6 Murata, K. *et al. Angew. Chem. Int. Ed.* **56**, 1 – 6, (2017).

7 Lyubovsky, M. & Pfefferle, L. *Appl. Catal., A* **173**, 107-119, (1998).

8 Lyubovsky, M. & Pfefferle, L. *Catal. Today* **47**, 29-44, (1999).

9 Datye, A. K. *et al. Appl. Catal., A* **198**, 179-196, (2000).

10 Yang, S., Maroto-Valiente, A., Benito-Gonzalez, M., Rodriguez-Ramos, I. & Guerrero-Ruiz, A. *Appl. Catal., B* **28**, 223-233, (2000).

11 Keating, J., Sankar, G., Hyde, T. I., Kohara, S. & Ohara, K. *Phys. Chem. Chem. Phys.* **15**, 8555-8565, (2013).

12 Miller, J. B. & Malatpure, M. *Appl. Catal., A* **495**, 54-62, (2015).

13 Chin, Y.-H. & Iglesia, E. *J. Phys. Chem. C* **115**, 17845-17855, (2011).

14 Chin, Y. H., Buda, C., Neurock, M. & Iglesia, E. *J. Am. Chem. Soc.* **135**, 15425-15442, (2013).

15 Chin, Y.-H., García-Diéguez, M. & Iglesia, E. *J. Phys. Chem. C* **120**, 1446-1460, (2016).

16 Lyubovsky, M., Pfefferle, L., Datye, A., Bravo, J. & Nelson, T. *J. Catal.* **187**, 275-284, (1999).
17 Zhang, D. *et al. Nanoscale* **9**, 6327-6333, (2017).
18 Matam, S. K., Aguirre, M., Weidenkaff, A. & Ferri, D. *J. Phys. Chem. C* **114**, 9439-9443, (2010).
19 Nilsson, J. *et al. ACS Catal.* **5**, 2481-2489, (2015).
20 Yamaguchi, A. *et al. Catal. Lett.* **68**, 139-145, (2000).
21 Newton, M. A., Fiddy, S. G., Guilera, G., Jyoti, B. & Evans, J. *Chem. Commun. (Camb)*, 118-120, (2005).
22 Yamamoto, T. *et al. Angew. Chem. Int. Ed.* **46**, 9253-9256, (2007).
23 Teramura, K. *et al. J. Phys. Chem. C* **112**, 8495-8498, (2008).
24 Shishido, T. *et al. Catal. Lett.* **131**, 413-418, (2009).
25 Tada, M. *et al. Phys. Chem. Chem. Phys.* **12**, 5701-5706, (2010).
26 Asakura, H. *et al. Phys. Chem. Chem. Phys.* **14**, 2983-2990, (2012).
27 Uemura, Y. *et al. Phys. Chem. Chem. Phys.* **14**, 2152-2158, (2012).
28 Kimura, M. *et al. Materials Transactions* **54**, 246-254, (2013).
29 Watzky, M. A. & Finke, R. G. *J. Am. Chem. Soc.* **119**, 10382-10400, (1997).
30 Mondloch, J. E., Yan, X. & Finke, R. G. *J. Am. Chem. Soc.* **131**, 6389-6396, (2009).
31 Mondloch, J. E. & Finke, R. G. *J. Am. Chem. Soc.* **133**, 7744-7756, (2011).
32 Mondloch, J. E., Bayram, E. & Finke, R. G. *J. Mol. Catal. A: Chem.* **355**, 1-38, (2012).

Chapter 6

Formation of Ru Shell on Co/Al_2O_3 by Galvanic Deposition Method and Its High Catalytic Performance for Three-Way Conversion

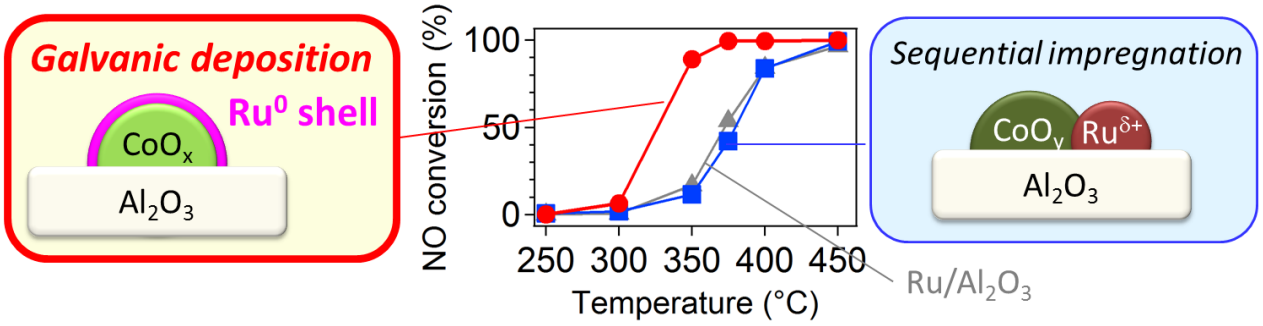

A supported Ru catalyst was prepared by a galvanic deposition (GD) of Ru on Co particles supported on Al_2O_3 (Ru/Co-GD). The structure and chemical state of Ru/Co-GD was characterized by using a pulsed CO chemisorption technique, STEM-EDS, XAFS, XPS, CO adsorption FT-IR spectroscopy, and temperature programed reduction (TPR) method. It is indicated that Ru/Co-GD forms Ru shell on Co nanoparticles. Such a unique structure was not formed on $Ru/Co/Al_2O_3$ prepared by a conventional sequential impregnation method (Ru/Co-seq). The Ru shell of Ru/Co-GD showed higher reducibility than Ru species of Ru/Co-seq as well as than Ru/Al_2O_3. Owing to the Ru shell having high reducibility, Ru/Co-GD showed enhanced catalytic activity for $NO\text{-}C_3H_6$ reaction. In addition, Co oxide on Ru/Co-GD exhibited high catalytic activity for CO and C_3H_6 oxidation. As a result, Ru/Co-GD showed superior performance for $NO\text{-}C_3H_6\text{-}CO\text{-}O_2$ reaction compared to the conventional catalysts. The Ru shell structure also contributed to the suppression of Ru vaporization.

Contents

6-1. Introduction

The platinum-group metals (PGMs) are essential in a variety of fields including catalysts, electronics, and jewelries. Among them, Pt, Pd, and Rh are the three most in-demand because they have been utilized for automobile catalysts, i.e., three-way catalysts (TWCs), which convert CO, hydrocarbon, and NO_x to CO_2 and N_2.[1] The growing automotive industry and the tightening of exhaust emission standards have led to an increasing demand for Pt, Pd, and Rh. However, they are limited in resources and their prices are high. Accordingly, there is an increasing attention to reduction of their usage in TWCs or development of the other metal catalysts with enhancement of catalytic performance.[2-5]

Morphology control of supported metal nanoparticles is one of the strategies for enhancement of their TWC performance.[6-12] It is well known that size of metal nanoparticles has large effect on catalytic activity because particle size changes the fraction of surface atoms on corner, edge, plane, and perimeter interface between metal and support, and also changes electronic state due to quantum-size effect and charge transfer between metal and support. In addition to size effect, shape of metal nanoparticles, for instance, cuboctahedron, octahedral, cube, sphere, and so on, also affects catalytic activity because surface structure of metal nanoparticles varies with particle shape.[7, 13] Recently, shell structure has been attracted intense attention.[14, 15] The shell metal on another kind of metal core or on a metal-oxide core has unique electronic state due to lattice mismatch and charge redistribution between shell metal and core metal or metal oxide.[16-20] Previously, we formed Ag thin-shell structure on Ni nanoparticles supported on SiO_2 using a galvanic deposition method. The shell structure of Ag on Ni nanoparticles enhanced the catalytic activity for CO oxidation compared to conventional Ag nanoparticles having spherical or cuboctahedral shape.[21, 22]

Some previous studies have demonstrated enhancement of catalytic activity of bimetal catalysts by preparation using a galvanic or redox method. Pan et al. reported that the Al_2O_3 supported Pd-Ni catalyst prepared by a galvanic method shows higher catalytic activity for CH_4 combustion than those prepared by conventional methods.[23] Kirichenko et al. presented that a redox method preparation of Al_2O_3 supported Au-Ru catalyst enhances the catalytic performance for preferential CO oxidation in NH_3.[24] These previous studies suggested that the galvanic or redox method leads to contact of two metal species concerning the galvanic or redox reaction. The Pd-Ni and Au-Ru systems might have unique structure such as thin-shell structure as we observed in the Ag-Ni system.

In this study, we prepared Al_2O_3 supported Ru-Co catalyst by a galvanic deposition of Ru on Co/Al_2O_3 (Ru/Co-GD), and examined its catalysis for $NO-C_3H_6$ and $NO-C_3H_6-CO-O_2$ reactions. In the practical use for the TWCs, Ru has not been utilized because of the vaporization of its oxide at high temperature above ~ 800 ˚C.[25, 26] However, Ru has high TWC performance, in particular for NO reduction to N_2, and thus, Ru has a potential to be developed as an alternative to the current PGMs (Rh, Pd, and Pt), if the Ru vaporization could be suppressed.[26-29] It should be also noted that Co species has high catalytic activity for oxidation of CO and hydrocarbons.[10] Herein, we present the formation of Ru shell structure on Ru/Co-GD, the suppressed Ru vaporization, and the enhanced catalytic activity of

Ru/Co-GD for NO-C_3H_6 and NO-CO-C_3H_6-O_2 reactions in comparison with the conventional Ru catalysts prepared by a conventional impregnation method.

6-2. Experimental

Materials

Al_2O_3 (JRC-ALO-8) was provided by the Catalysis Society of Japan. All reagents were purchased from Kishida Chemical Co., Ltd. All gases for catalyst preparation and reaction were purchased from Taiyo Nippon Sanso Corp.

Catalyst preparation

Ru was deposited on pre-reduced Co/Al_2O_3 in water to prepare Ru/Co-GD as follows. Co/Al_2O_3 with 4 wt% Co loading was prepared by a conventional impregnation method using $Co(NO_3)_2$ as a precursor. After dry at 80 ˚C overnight, the resulting $Co(NO_3)_2/Al_2O_3$ (500 mg) was reduced in a 100 mL round-bottomed flask under a 100 mL min^{-1} of H_2 flow at 400 ˚C for 30 min. After cooling the sample and gas replacement with N_2, 8 mL of water was added to the pre-reduced Co/Al_2O_3. Under vigorous stirring at 30 ˚C, 8 mL of an aqueous solution of $RuCl_3$ (6.2 mM) was introduced to the suspension. After stirring for 15 min, the suspension was separated by centrifugation and washed 3 times with 40 mL of water. The washed slurry was dried at 80 ˚C overnight to give Ru/Co-GD.

For comparison, Al_2O_3 supported RuCo bimetal catalysts (Ru: ca. 1 wt%, Co ca. 4 wt%) were prepared by a conventional sequential impregnation method (RuCo-seq). Co/Al_2O_3 prepared by calcination of $Co(NO_3)_2/Al_2O_3$ at 500 ˚C under air for 3 h was impregnated in a $RuCl_3$ aqueous solution, followed by evaporation of the water, drying at 80 ˚C, and calcined at 500 ˚C. In addition, Ru/Al_2O_3 (Ru: 1 wt%) was also prepared by an impregnation method (precursor: $RuCl_3$; dry: 80 ˚C; calcination: 500 ˚C).

Catalytic reaction

Prior to the catalytic tests, the prepared catalysts were treated with a 40 mL min^{-1} of O_2 flow at 450 ˚C for 10 min and then with a 40 mL min^{-1} of H_2 flow at 450 ˚C for 10 min. The catalytic test was performed on a conventional fixed-bed flow reactor at atmospheric pressure with 17.5 mg of catalyst inside a Pyrex glass tube under a 60 mL min^{-1} of gas flow containing 1000 ppm of NO and 111 ppm of propylene (C_3H_6) and balance Ar for NO-C_3H_6 reaction; 1000 ppm of NO, 4000 ppm of CO, 1000 ppm of C_3H_6, 6000 ppm of O_2, and balance Ar for NO-C_3H_6-CO-O_2 reaction (GHSV = 140000 h^{-1}). The outlet gas was analyzed during stepwise increase in the reaction temperature, and the concentrations of the reactants at steady state after 10min for each temperature were analyzed using NO_x and CO/CO_2 analyzer (Horiba VA3000).

Characterization

The loadings of Ru and Co of RuCo bimetal catalysts were determined by X-ray fluorescence spectroscopy (XRF, Rigaku, EDXL-300). The dispersion of Ru was evaluated by pulsed CO adsorption at 50 ˚C in a flow of He. The CO pulse measurement was performed on a BELCAT-B (MicrotracBEL) equipped with a thermal conductivity detector.

High-angle annular dark-filed scanning transmission electron microscope (HAADF STEM) and energy dispersive X-ray spectroscopy (EDS) mapping images were taken on a JEM-2100F (JEOL) operated at 200 kV accelerating voltage. The samples for STEM and EDS analysis were prepared by putting drops of a methanol solution onto a carbon-coated molybdenum grid.

Ru K-edge X-ray absorption fine structure (XAFS) spectroscopy measurements were carried out on the BL01B1 beamline of SPring-8 with a Si(311) two-crystal monochromator. All spectra were recorded in transmission mode. Ion chambers of I_0 (17 cm) and I detector (31 cm) were filled with Ar100% and Ar50% Kr50% flows, respectively. The X-ray energy was calibrated with a spectrum of Cu foil at 8980 eV. Data analysis was performed using Athena and Arthemis programs included in the Demeter package (ver. 0.9.21).[30] The k^3 weighted Ru K-edge extended XAFS (EXAFS) spectra were Fourier-transformed in the ranges of 3.0-15.0 $Å^{-1}$.

Fourier Transform Infrared (FT-IR) spectra of CO adsorbed on the catalysts were obtained on a JASCO FT/IR-6100 (JASCO Co.) with a resolution of 4 cm^{-1}. A catalyst powder (60 mg) was pressed into a wafer with a diameter of 20 mm. The catalyst was pretreated under H_2 flow (100 mL min^{-1}) at 400 ˚C for 15 min, O_2 flow (100 mL min^{-1}) for 15 min, and then H_2 flow (100 mL min^{-1}) at 150 ˚C for 15 min. The catalyst was cooled to 35 ˚C, and the background spectrum was recorded. After the catalyst was treated under 10% CO (100 mL min^{-1}) for 15 min and then Ar (100 mL min^{-1}) for 15 min, the CO adsorption FT-IR spectrum was obtained.

X-ray photoelectron spectra (XPS) of Ru 3d region were acquired on a JPS-9000MC system (JEOL Ltd.) using Al $K\alpha$ radiation, and those of Co 2p region on an ULVAC PHI 5500MT system using Mg $K\alpha$ radiation.

Temperature-programmed reduction of the samples by C_3H_6 (C_3H_6-TPR) was performed on a conventional fixed-bed flow reactor at atmospheric pressure with 30 mg of catalyst inside a Pyrex glass tube. The samples were pretreated at 450 ˚C under a 30 mL min^{-1} of 10% H_2 flow (Ar balance) for 10 min, and then under a 30 mL min^{-1} of 1% O_2 flow (Ar balance) for 30 min. After cooling the sample to 100 ˚C, the samples were heated up to 550 ˚C at 5 ˚C min^{-1} under a 30 mL min^{-1} of gas flow containing 1 % of C_3H_6 (Ar balance). The outlet gas was analyzed using CO/CO_2 analyzer (Horiba VA3000).

6-3. Results and Discussion

Catalyst characterization

The loading amounts of Ru and Co of Ru/Co-GD were determined using XRF spectroscopy. As presented in Table 1, the Ru loading of Ru/Co-GD was 1.2 wt%. Meanwhile, the Co loading of Ru/Co-

GD was 3.0 wt%, and smaller than that of the Co/Al_2O_3 precursor (4.0 wt%). These results indicate that Ru is successfully deposited through galvanic replacement reaction, since the galvanic reaction between Ru^{3+} and the pre-reduced Co/Al_2O_3 results in formation of Ru metal and Co ions dissolved in water. The metal loadings of Ru/Co-seq and Ru/Al_2O_3 were also determined using XRF (Table 1). The Ru loadings of the two catalysts were almost the same as that of Ru/Co-GD.

Table 1. Metal loadings, adsorbed amount of CO, and Ru dispersion of the Ru catalysts.

Catalyst	Loading (wt%) [a]		CO adsorption	Ru dispersion
	Ru	Co	(μmol/g_{cat}) [b]	(%) [c]
Ru/Co-GD	1.2	3.0	22.7	22.5
Ru/Co-seq	0.9	3.5	10.2	11.3
Ru/Al_2O_3	1.0	0	11.4	11.4

[a] Determined by XRF. [b] Determined by pulsed CO chemisorption technique. [c] Calculated from the Ru loading and CO adsorption amount.

To estimate the Ru dispersion, the CO adsorption amount on Ru species was evaluated after each Ru catalyst was pretreated under H_2 at 150 ˚C where Ru species is reduced to Ru metal but the reduction of Co species to Co metal is negligible (Figure 1).[31] The dispersion of Ru was evaluated from the CO adsorption amount and the Ru loadings assuming one-to-one binding of CO on Ru. As a result, Ru species of Ru/Co-GD was more highly dispersed than those of Ru/Co-seq and Ru/Al_2O_3.

Figure 2 shows the Ru K-edge FT-EXAFS spectra of Ru/Co-GD, Ru/Co-seq, Ru/Al_2O_3, and the references (Ru metal powder and RuO_2). Prior to the Ru K-edge XAFS measurements, the samples were treated under H_2 at 400 ˚C, and the spectra were obtained without exposure to air. The FT-EXAFS spectra of Ru/Co-GD and Ru/Co-seq showed the first shell peak at 2.4 Å, where Ru/Al_2O_3 and Ru metal powder also showed the first shell peak. The first shell of Ru/Co-GD and Ru/Co-seq was well fitted with a Ru-Ru scattering parameter. The calculated interatomic distance of Ru-Ru was consistent with that of Ru metal as shown in Table 2. Therefore, Ru particles are formed on Ru/Co-GD and Ru/Co-seq without Ru-Co alloying. The coordination number of Ru-Ru (CN(Ru-Ru)) of Ru/Co-GD was smaller than Ru/Co-seq and Ru/Al_2O_3, which suggests that Ru species of Ru/Co-GD is more highly dispersed than those of Ru/Co-seq and Ru/Al_2O_3. This result agrees with the aforementioned Ru dispersion evaluated by the CO adsorption amount (Table 1).

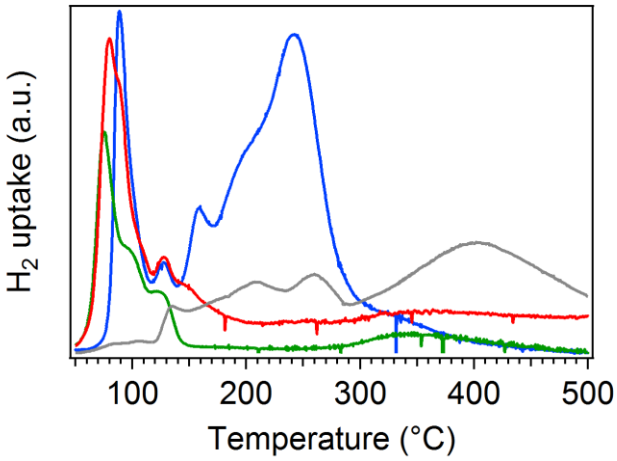

Figure 1. H_2-TPR of Ru/Co-GD (red), Ru/Co-seq (blue), Ru/Al_2O_3 (green), and Co/Al_2O_3 (gray). The Ru species is considered to be completely reduced at 150˚C by H_2, where CoO_x is reduced to CoO but not to Co metal (The H_2 uptake of Co/Al_2O_3 at ca. 120-300 °C is assignable to reduction of Co_3O_4 species to CoO and that at 300-500 °C is to reduction of CoO to Co metal).

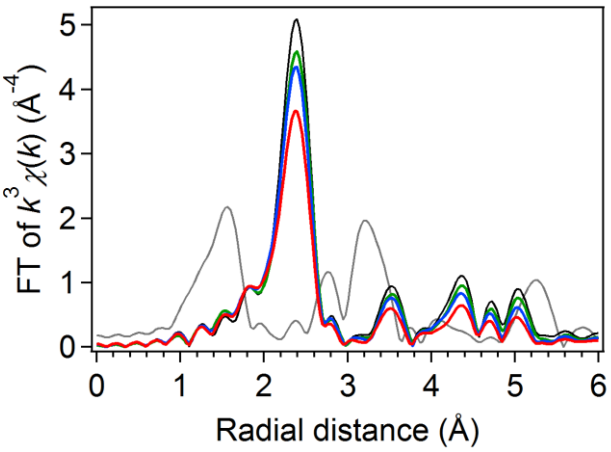

Figure 2. FT of k^3 weighted Ru K-edge EXAFS spectra of Ru/Co-GD (red bold solid), RuP/Co-seq (blue), Ru/Al_2O_3 (green), Ru metal powder (black), and RuO_2 (gray).

Table 2. Structural parameters for Ru-Ru shell of the Ru catalysts. [a]

Catalysts	C.N. [b]	r [c] (Å)	σ^2 [d] (Å^2)	R [e]
Ru/Co-GD	9.2(10)	2.665(4)	0.0046(5)	0.004
Ru/Co-seq	11.0(8)	2.668(3)	0.0046(3)	0.002
Ru/Al_2O_3	11.8(7)	2.678(2)	0.0047(3)	0.001

[a] Determined by XRF. [b] Determined by pulsed CO chemisorption technique. [c] Calculated from the Ru loading and CO adsorption amount.

The CO adsorption FT-IR spectra of Ru/Co-GD, Ru/Co-seq, Ru/Al_2O_3 are shown in Figure 3. The FT-IR spectrum of Ru/Co-GD showed three bands at around 2130, 2054, and 1970 cm^{-1}. The band at 2130 cm^{-1} is assignable to CO adsorbed on Al_2O_3.[32] The band at 2054 cm^{-1} is assigned to linearly adsorbed CO species atop Ru atoms on high coordination Ru sites, i.e., terrace sites.[33] The band at 1970 cm^{-1} is assigned to bridge bonded CO.[34] The FT-IR spectral feature of Ru/Co-GD was different from those of Ru/Co-seq and Ru/Al_2O_3, which were similar and showed intense band at ca. 2080 cm^{-1}. The intense band at ca. 2080 cm^{-1} is attributed to CO adsorbed on low-coordination Ru sites, i.e., corner and edge sites.[33, 34] The intense band due to CO adsorbed on low-coordination Ru sites suggests the formation of small Ru particles. On the other hand, the intense band due to CO adsorbed on terrace sites, which was observed on Ru/Co-GD (Figure 3(a)), reflects large Ru particles. In addition, the relatively high intensity of the band at 1940-1980 cm^{-1} assignable to the bridge bonded CO is usually observed on large metal particles.[34] Thus, if the conventional spherical shape of Ru particles is assumed for the three catalysts, the FT-IR spectra suggest that Ru/Co-GD has larger Ru particles than Ru/Co-seq and Ru/Al_2O_3. This is inconsistent with the aforementioned CO adsorption amounts (Table 1) and the XAFS results (Figure 2). This contradiction can be resolved when the thin shell structure of Ru species covering Co particles is assumed (only) for Ru/Co-GD. For an extreme example, an ideal infinite flat Ru composed of double Ru layer (CN(Ru-Ru) = 9) on a support has high dispersion of Ru (50%) and its surface is composed of high-coordination Ru sites. Therefore, we concluded that Ru/Co-GD has shell structure, which is different from Ru/Co-seq and Ru/Al_2O_3 having usual shape such as spherical shape.

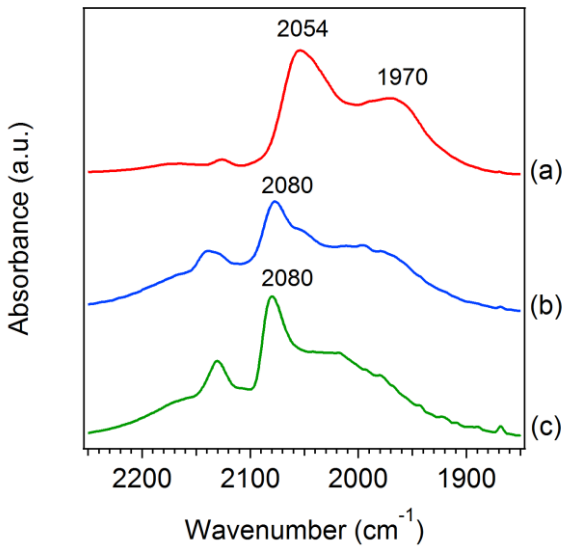

Figure 3. CO adsorption FT-IR spectra of (a) Ru/Co-GD, (b) Ru/Co-seq, (c) Ru/Al_2O_3.

We observed Ru/Co-GD using HAADF-STEM and EDS as shown in Figure 4(a). The red, green, and yellow regions of the EDS map indicate the existence of Ru, Co, and the overlapping of Ru and Co, respectively. Ru species mainly exists in the overlapping region, suggesting that Ru species of

Ru/Co-GD covers Co particles. The result agrees with the formation of Ru shell structure on Co particles. For comparison, we also observed Ru/Co-seq as shown in Figure 4(b). The yellow region was smaller than the red region, although the red region was adjacent to the green region. Thus, Ru/Co-seq forms Ru particles on or in contact with Co particles. Therefore, Ru species of Ru/Co-GD forms shell structure on Co particles, which is not obtained by the conventional catalyst preparation using the sequential impregnation method. It should be also noted that the Co species formed relatively large particles on Al_2O_3 as shown in Figure 4. The large Co particles on Al_2O_3 is considered to give the Ru shell structure having relatively large terrace by the galvanic deposition of Ru^{3+} on the pre-reduced large Co particles.

The surface chemical state of Ru of Ru/Co-GD was investigated by XPS in Ru 3d region. Figure 5 shows the XPS of Ru/Co-GD, Ru/Co-seq, and Ru/Al_2O_3 after treatment under the reaction gas ($NO-CO-C_3H_6-O_2$) at 450 ˚C. The Ru $3d_{3/2}$ peak was hidden in the C1s peak derived from adventitious carbon species. The Ru $3d_{5/2}$ peaks of the samples were separated from the C1s peak as presented by red line in Figure 5. The binding energy of Ru $3d_{5/2}$ peak increased in the order of Ru/Co-GD < Ru/Al_2O_3 < Ru/Co-seq as presented in Table 3. The lower binding energy indicates the formation of more metallic Ru surface.[35, 36] It is suggested that the Ru species having shell structure on Ru/Co-GD is in more metallic state during the catalytic reaction compared to Ru/Co-seq and Ru/Al_2O_3.

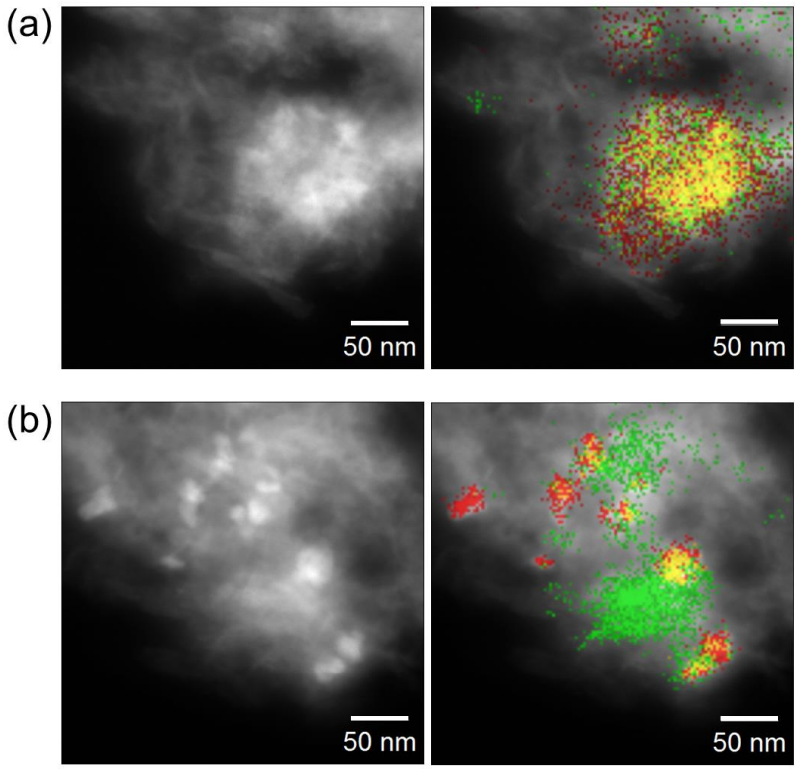

Figure 4. Typical HAADF STEM images and those overlaid with Ru and Co EDS elemental maps for (a) Ru/Co-GD and (b) Ru/Co-seq. For the elemental maps, Ru is indicated in red, Co in green, and Ru+Co in yellow.

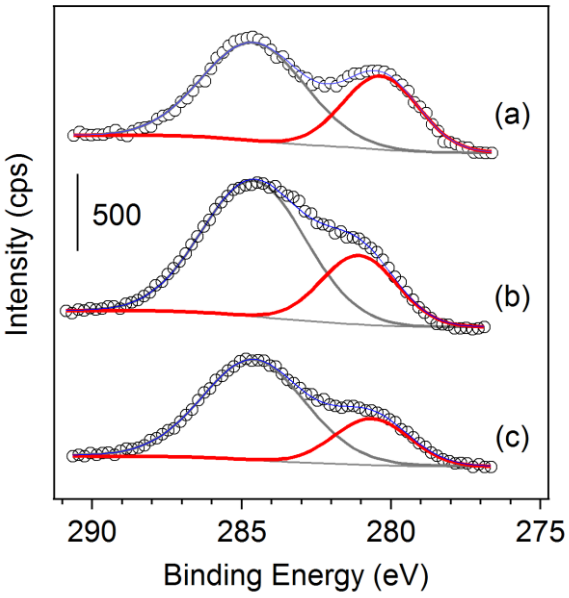

Figure 5. Ru 3d XPS of (a) Ru/Co-GD, (b) Ru/Co-seq, and (c) Ru/Al_2O_3. The raw data are indicated by open circles. The spectra were deconvoluted with two curves: the Ru $3d_{5/2}$ XPS in red; the mixture of C1s and Ru $3d_{3/2}$ in gray.

Table 3. Results of Ru 3d and Co 2p XPS analysis.

Catalyst	Ru $3d_{5/2}$ (eV) [a]	Co $2p_{3/2}$ (eV) [a]	ΔCo 2p (eV) [b]	$A_{sat}/A_{3/2}$ [c]
Ru/Co-GD	280.3	780.8	15.9	0.7
Ru/Co-seq	281.0	781.2	15.6	0.8
Ru/Al_2O_3	280.6	-	-	-
Co/Al_2O_3	-	780.7	15.9	0.6

[a] Peak energy. [b] Difference of the peak energies between Co $2p_{3/2}$ and $2p_{1/2}$. [c] Ratio of the peak areas of Co$2p_{3/2}$ to its satellite peak.

The Co species of the catalysts after the reaction were also characterized by XPS. Figure 6 shows the Co 2p XPS of Ru/Co-GD, Ru/Co-seq, and Co/Al_2O_3 after the reaction (NO-CO-C_3H_6-O_2) at 450 ˚C. The chemical state was evaluated from the peak binding energy of Co $2p_{3/2}$, that of Co $2p_{1/2}$, their difference ($\Delta_{3/2\text{-}1/2}$), and the relative intensity of the satellite peak to the Co $2p_{3/2}$ peak ($A_{sat}/A_{3/2}$), which are listed in Table 3. The peak energies of Co $2p_{3/2}$ and $2p_{1/2}$ indicates the formation of CoO and/or Co_3O_4.[31, 35] It is known that the values of $\Delta_{3/2\text{-}1/2}$ and $A_{sat}/A_{3/2}$ reflect the valence state of Co oxide, and a decrease of these values indicates an increase of Co^{3+} species, i.e., Co_3O_4.[31, 35] Accordingly, the Co oxide species (CoO_x) on Co/Al_2O_3 and Ru/Co-GD are closer to Co_3O_4 compared to that on Ru/Co-seq.

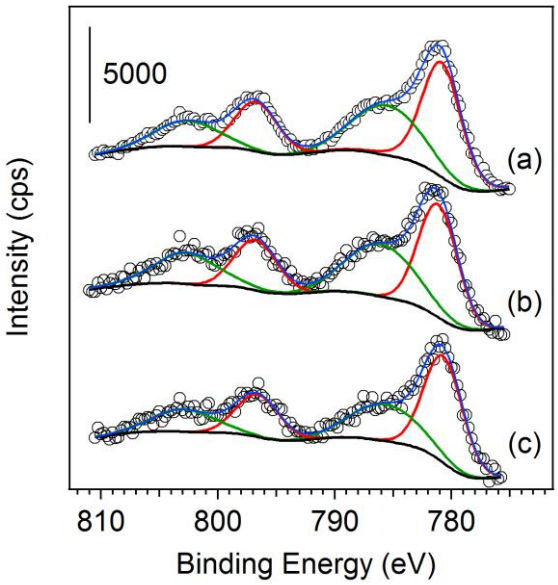

Figure 6. Co 2p XPS of (a) Ru/Co-GD, (b) Ru/Co-seq, and (c) Ru/Al_2O_3. The spectra were deconvoluted with Co 2p XPS in red and its satellite in green.

Based on the above results, the structures of Ru/Co-GD and Ru/Co-seq are schematically drawn in Figure 7. Ru/Co-GD has CoO_x-Ru core-shell structure, and Ru/Co-seq has Ru particles on or in contact with CoO_x. The Ru species of Ru/Co-GD is in more metallic state than that of Ru/Co-seq. The CoO_x particles of Ru/Co-GD are in higher valence state (closer to C_3O_4) than Ru/Co-seq.

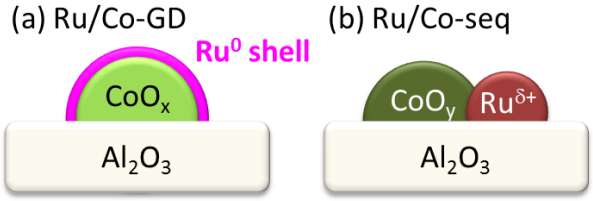

Figure 7. Schematic drawings of the structures of (a) Ru/Co-GD and (b) Ru/Co-seq. The Ru shell of Ru/Co-GD is more metallic than Ru/Co-seq. The Co oxide of Ru/Co-GD is in higher valence state than that of Ru/Co-seq, i.e., x > y.

NO-C_3H_6 reaction.

Figure 8 shows NO conversions as a function of temperature for NO-C_3H_6 reaction under stoichiometric condition over Ru/Co-GD, Ru/Co-seq, Ru/Al_2O_3, and Co/Al_2O_3. The NO conversion over Ru/Co-GD initiated from 250 ˚C, and was completed at 350 ˚C. The temperatures for 50 and 100% NO conversion over Ru/Co-GD were ca. 50 ˚C lower than that over Ru/Al_2O_3. Namely, Ru/Co-GD showed higher catalytic activity than Ru/Al_2O_3. On the contrary, Ru/Co-seq showed slightly lower activity for the NO conversion than Ru/Al_2O_3. It should be also noted that Co/Al_2O_3 showed almost no NO conversion below 450 ˚C. Thus, Ru species is active for the NO conversion. To evaluate the

specific activity of Ru species, the turnover frequencies (TOFs) of Ru/Co-GD, Ru/Co-seq, and Ru/Al_2O_3 were calculated assuming the CO adsorption amount (Table 1) as the amount of Ru surface atom. As presented in Table 4, the TOF of Ru/Co-GD was higher than that of Ru/Al_2O_3, suggesting that Ru/Co-GD has highly active Ru species compared to Ru/Al_2O_3. In contrast, Ru/Co-seq showed lower TOF than Ru/Al_2O_3. Since the STEM observation indicated that Ru/Co-seq contains Ru particles deposited on or in contact with CoO_x particles (Figure 4(b)), the adjacent CoO_x does not enhance the catalytic activity of Ru species for the NO-C_3H_6 reaction. The result suggests that the enhanced catalytic activity of Ru/Co-GD is derived from the shell structure of Ru on CoO_x rather than the contact of Ru with CoO_x.

Previous studies on NO reduction reactions over precious metals including Ru have demonstrated that their rate determining step is the reduction of oxidized metal surface by reducing agents such as C_3H_6 and CO.[28, 37] The results indicate that the reducibility of metal surface determines the catalytic activity for the NO reduction reactions. Accordingly, we examined the reducibility of the Ru species by the temperature programed reduction (TPR) of the Ru catalysts using C_3H_6 as the reducing agent. As shown in Figure 9, Ru/Co-GD showed the first peak at 258 ˚C corresponding to the reduction of Ru species, and the peak temperature was lower than that of Ru/Al_2O_3 (275 ˚C). It is indicated that the Ru species of Ru/Co-GD is more easily reduced by C_3H_6 than that of Ru/Al_2O_3. On the other hand, Ru/Co-seq exhibited the first peak at 291 ˚C, which was higher than that of Ru/Al_2O_3. This indicates that the Ru species of Ru/Co-seq is more difficult to be reduced in comparison with that of Ru/Al_2O_3. The C_3H_6-TPR result is consistent with the result of Ru 3d XPS analysis which indicated that Ru/Co-GD is in more metallic state than Ru/Al_2O_3, and Ru/Co-seq is in more oxidized state than Ru/Al_2O_3. The more metallic sate of Ru/Co-GD is also supported by the CO adsorption FT-IR spectra, because the metallic state causes the shift of the CO adsorption peak to lower wavenumber.[34] Note that the reducibility of Ru species agrees with the catalytic activity for the NO-C_3H_6 reaction. Therefore, the high reducibility of Ru/Co-GD by C_3H_6 is responsible for its high catalytic activity for the NO conversion.

The higher reducibility of Ru/Co-GD than Ru/Al_2O_3 is considered to be derived from the structure of Ru/Co-GD. The structural characterization of Ru/Co-GD showed three unique structural features not seen on or different form Ru/Al_2O_3: (1) the contact of Ru species with CoO_x; (2) the higher Ru dispersion; (3) the Ru shell having relatively large terrace. With respect to (1), Ru/Co-seq having Ru in contact with CoO_x showed low reducibility. Accordingly, (1) the contact of Ru species with CoO_x cannot account for the high reducibility of Ru/Co-GD. As for (2) high Ru dispersion, it has been reported that small Ru nanoparticles is more deeply oxidized compared to large Ru nanoparticles.[9, 38] It is suggested that the high Ru dispersion of Ru/Co-GD is not responsible for its high reducibility. By this process of elimination, we therefore propose that (3) the Ru shell structure having relatively large terrace is the origin of the high reducibility of Ru species and its resulting high catalytic activity for the NO-C_3H_6 reaction. The reason for the high reducibility of the Ru shell might be that the Ru species on terrace has lower affinity to oxygen species than those on low-coordination sites such as corner and

edge.[11, 39-41]

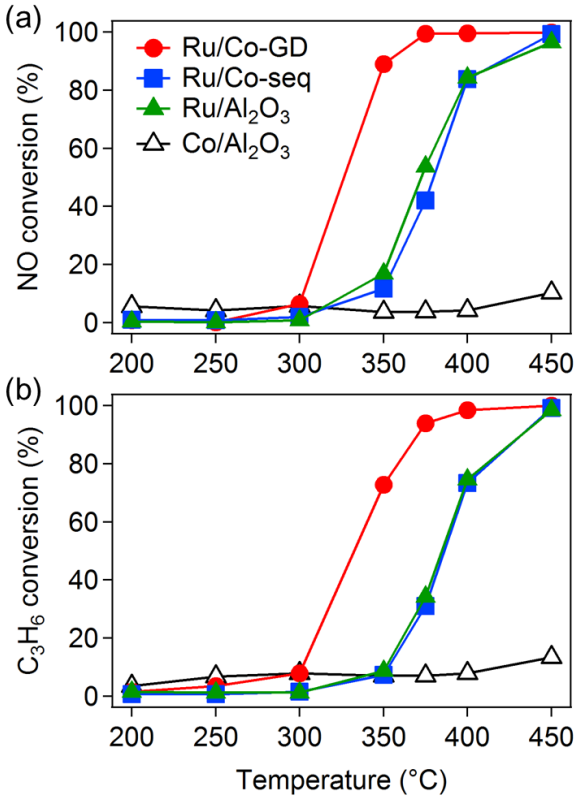

Figure 8. (a) NO and (b) C_3H_6 conversions as a function of reaction temperature for the NO-C_3H_6 reaction over RuCo-GD (red circle), Ru/Co-seq (blue square), Ru/Al_2O_3 (green triangle), and Co/Al_2O_3 (black open triangle).

Table 4. TOFs for the NO-C_3H_6 reaction.

Catalyst	TOF (s^{-1}) [a]
Ru/Co-GD	0.084
Ru/Co-seq	0.030
Ru/Al_2O_3	0.038

[a] Calculated from the NO conversions at 350 ˚C and the CO adsorption amounts.

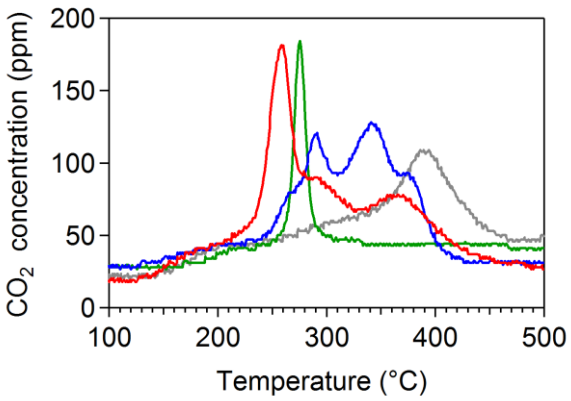

Figure 9. C_3H_6-TPR of Ru/Co-GD (red), Ru/Co-seq (blue), Ru/Al_2O_3 (green), and Co/Al_2O_3 (gray).

NO-C_3H_6-CO-O_2 reaction and Ru vaporization

We applied the Ru catalysts to the NO-C_3H_6-CO-O_2 reaction. Figure 10 shows (a) NO, (b) C_3H_6, and (c) CO conversions over RuCo-GD as a function of reaction temperature, together with those over RuCo-seq, Ru/Al_2O_3, and Co/Al_2O_3 for comparison. The order of the catalytic activity for the NO conversion was Ru/Co-GD > Ru/Al_2O_3 > Ru/Co-seq, which is consistent with the order of the NO-C_3H_6 reaction. In addition, the NO conversions of NO-C_3H_6-CO-O_2 reaction (Figure 10) over all catalysts well agreed with those for NO-C_3H_6 reaction at each temperature (Figure 8). On the other hand, the NO-CO reaction over the catalysts proceeded at least 50˚C lower temperature compared to the NO-C_3H_6-CO-O_2 reaction (Figure 11). It is indicated that the NO-C_3H_6 reaction is the key to the NO conversion in the NO-C_3H_6-CO-O_2 reaction over all of the Ru containing catalysts, and the NO-CO reaction plays little part in the NO-C_3H_6-CO-O_2 reaction. In another respect, the CO conversion in the NO-C_3H_6-CO-O_2 reaction results from CO-O_2 reaction (i.e., CO oxidation), even in the case of Ru/Al_2O_3, although Ru/Al_2O_3 seemed to simultaneously convert NO, CO, and C_3H_6 in the NO-C_3H_6-CO-O_2 reaction (Figure 10). Based on these results, the high NO conversion of Ru/Co-GD for the NO-C_3H_6-CO-O_2 reaction is derived from its high activity for the NO-C_3H_6 reaction. In other words, the Ru shell structure of Ru/Co-GD is effective for NO conversion even in the presence of O_2 and CO. With respect to CO and C_3H_6 oxidation, the Co containing catalysts including Co/Al_2O_3 showed higher catalytic activity compared to Ru/Al_2O_3 (although 100% conversion of CO was not attained over Co/Al_2O_3 because of no NO reduction reaction over Co/Al_2O_3). Accordingly, the enhanced catalytic activity of Ru/Co-GD and Ru/Co-seq for the oxidation of CO and C_3H_6 is attributable to CoO_x. It is also to be mentioned that Ru/Co-GD and Co/Al_2O_3 showed higher oxidation activity than Ru/Co-seq. The higher catalytic activity of Ru/Co-GD and Co/Al_2O_3 can be attributed to their high content of Co_3O_4 species based on the XPS result (Table 3) and the previous reports showing that Co_3O_4 has remarkable activity for oxidation of CO and hydrocarbons.[10] On the basis of the above results, we concluded that the superior catalytic activity of Ru/Co-GD for the NO-C_3H_6-CO-O_2 reaction is due to the Ru shell structure and Co_3O_4 species.

Finally, the effect of Ru shell structure on the Ru vaporization was investigated. Ru/Co-GD was

calcined under air for 10 h at 800 and 1000˚C, and the Ru content was evaluated using XRF spectroscopy. Figure 12 shows the variation of Ru loading with the aging treatment for Ru/Co-GD together with those for Ru/Co-seq and Ru/Al_2O_3. The Ru content of Ru/Co-GD slightly decreased with the calcination at 800˚C; however, the Ru contents of Ru/Co-seq and Ru/Al_2O_3 decreased more significantly compared to Ru/Co-GD. This result indicates that Ru/Co-GD has higher resistance to the Ru vaporization than Ru/Co-seq and Ru/Al_2O_3 (although almost all of Ru on the three catalysts was vanished at 1000˚C). The resistance to the Ru vaporization increased in the order of Ru/Co-GD > Ru/Al_2O_3 > Ru/Co-seq, which agrees with the order of the Ru reducibility. It is reasonable to consider that the high reducibility of Ru/Co-GD is responsible for the suppression of Ru vaporization, since the oxidation of Ru concerns in the vaporization at relatively low temperature (~ 800˚C) but Ru metal has much higher boiling point (~ 4000˚C). Therefore, the Ru shell structure having high reducibility enhanced the suppression of the Ru vaporization as well as the catalytic activity for the NO reduction reaction.

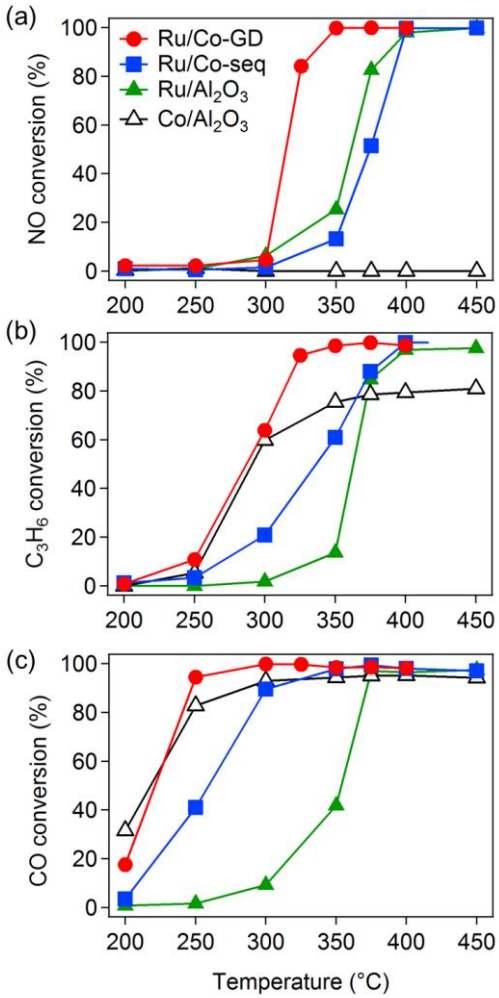

Figure 10. (a) NO, (b) C_3H_6, and (c) CO conversions as a function of reaction temperature for the NO-C_3H_6-CO-O_2 reaction over RuCo-GD (red circle), Ru/Co-seq (blue square), Ru/Al_2O_3 (green triangle), and Co/Al_2O_3 (black open triangle).

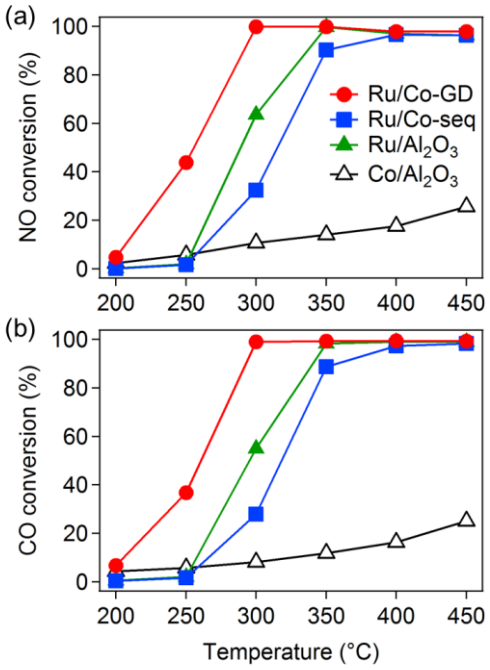

Figure 11. (a) NO and (b) CO conversions as a function of reaction temperature for the NO-CO reaction (NO: 1000 ppm, CO: 1000 ppm, Ar: balance) over RuCo-GD (red circle), Ru/Co-seq (blue square), Ru/Al_2O_3 (green triangle), and Co/Al_2O_3 (black open triangle).

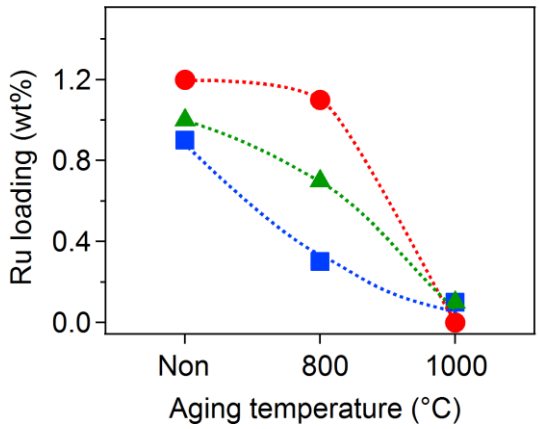

Figure 12. Variation of Ru loadings with aging by calcination at 800 ˚C for 10 h under air and 1000 ˚C for 10 h for Ru/Co-GD (red circle), Ru/Co-seq (blue square), and Ru/Al_2O_3 (green triangle).

6-4. Conclusion

Ru/Co-GD prepared by the galvanic deposition method showed Ru shell structure on CoO_x nanoparticles. Ru/Co-GD showed high performance for the NO-C_3H_6 reaction compared to the conventional catalysts because of the Ru shell structure having high reducibility. Owing to the Ru shell

structure as well as the Co_3O_4 species, Ru/Co-GD showed superior catalytic activity for the NO-C_3H_6-CO-O_2 reaction compared to Ru/Co-seq and Ru/Al_2O_3. The Ru shell structure also contributed to the suppression of Ru vaporization. The findings not only develop the potential for utilization of Ru in the TWCs, but also underline the importance of morphology control of supported metal catalysts to enhance their performance.

6-5. References

1 Granger, P. & Parvulescu, V. I. *Chemical Reviews* **111**, 3155-3207, (2011).

2 Machida, M. *et al. The Journal of Physical Chemistry C* **119**, 373-380, (2015).

3 Haneda, M., Kaneko, T., Kamiuchi, N. & Ozawa, M. *Catalysis Science & Technology* **5**, 1792-1800, (2015).

4 Hosokawa, S. *et al. Chemistry Letters* **43**, 874-876, (2014).

5 Satsuma, A., Ueda, K., Ito, Y., Ang, C. A. & Ohyama, J. *Chemistry Letters* **44**, 703-705, (2015).

6 Tanabe, T. *et al. Applied Catalysis B: Environmental* **105**, 41-49, (2011).

7 Renzas, J. R., Zhang, Y., Huang, W. & Somorjai, G. A. *Catalysis Letters* **132**, 317-322, (2009).

8 Liu, X., Tian, D., Ren, S. & Meng, C. *J. Phys. Chem. C* **119**, 12941-12948, (2015).

9 Joo, S. H. *et al. Nano Letters* **10**, 2709-2713, (2010).

10 Xie, X., Li, Y., Liu, Z.-Q., Haruta, M. & Shen, W. *Nature* **458**, 746-749, (2009).

11 Ohyama, J., Sato, T., Yamamoto, Y., Arai, S. & Satsuma, A. *Journal of the American Chemical Society* **135**, 8016-8021, (2013).

12 Ohyama, J., Koketsu, T., Yamamoto, Y., Arai, S. & Satsuma, A. *Chemical Communications* **51**, 15823-15826, (2015).

13 An, K. & Somorjai, G. A. *ChemCatChem* **4**, 1512-1524, (2012).

14 Gawande, M. B. *et al. Chemical Society Reviews* **44**, 7540-7590, (2015).

15 Chen, S. J. *et al. Catalysis Letters* **145**, 1420-1428, (2015).

16 Sun, Y.-N. *et al. Angewandte Chemie* **122**, 4520-4523, (2010).

17 Willinger, M. G. *et al. Angewandte Chemie International Edition* **53**, 5998-6001, (2014).

18 Strasser, P. *et al. Nat Chem* **2**, 454-460, (2010).

19 Ruban, A., Hammer, B., Stoltze, P., Skriver, H. L. & N テ rskov, J. K. *Journal of Molecular Catalysis A: Chemical* **115**, 421-429, (1997).

20 Tang, H. & Trout, B. L. *J. Phys. Chem. B* **109**, 17630-17634, (2005).

21 Mahara, Y. *et al. Chemistry Letters* **43**, 910-912, (2014).

22 Mahara, Y., Ishikawa, H., Ohyama, J., Sawabe, K. & Satsuma, A. *Catal. Today* **265**, 2-6, (2016).

23 Pan, X., Zhang, Y., Miao, Z. & Yang, X. *J. Energy Chem.* **22**, 610-616, (2013).

24 Kirichenko, O. A. *et al. Appl. Catal., B* **134-135**, 123-129, (2013).

25 Bell, W. E. & Tagami, M. *J. Phys. Chem.* **67**, 2432-2436, (1963).

26 Bradow, R., Jovanovic, D., Petrovic, S., Jovanovic, Z. & Terlecki-Baricevic, A. *Industrial & Engineering Chemistry Research* **34**, 1929-1932, (1995).

27 Gonzalez-Velasco, J. R., Gutierrez-Ortiz, M. A., Gonzalez-Marcos, J. A., Pranda, P. & Steltenpohl, P. *Journal of*

Catalysis **187**, 24-29, (1999).

28 Hornung, A., Muhler, M. & Ertl, G. *Topics in Catalysis* **11-12**, 263-270, (2000).

29 Li, Y. & Armor, J. N. *Applied Catalysis B: Environmental* **1**, L21-L29, (1992).

30 Ravel, B. & Newville, M. *Journal of Synchrotron Radiation* **12**, 537-541, (2005).

31 Wang, Q. *et al. Applied Catalysis B: Environmental* **168– 169**, 42-50, (2015).

32 Comas-Vives, A. *et al. Physical Chemistry Chemical Physics* **18**, 1969-1979, (2016).

33 Loveless, B. T., Buda, C., Neurock, M. & Iglesia, E. *Journal of the American Chemical Society* **135**, 6107-6121, (2013).

34 Chin, S. Y., Williams, C. T. & Amiridis, M. D. *The Journal of Physical Chemistry B* **110**, 871-882, (2006).

35 Wagner, C. D., Riggs, W. M., Davis, L. E. & Moulder, J. F. *Handbook of X-ray Photoelectron Spectroscopy*. (Perkin-Elmer Corp., 1979).

36 Chan, H. Y. H., Takoudis, C. G. & Weaver, M. J. *Journal of Catalysis* **172**, 336-345, (1997).

37 Hirata, H. *Catal. Surv. Asia* **18**, 128-133, (2014).

38 Qadir, K. *et al. Nano Letters* **12**, 5761, (2012).

39 Jiang, L., Hsu, A., Chu, D. & Chen, R. *J. Electrochem. Soc.* **156**, B643-B649, (2009).

40 Shao, M., Peles, A. & Shoemaker, K. *Nano Letters* **11**, 3714-3719, (2011).

41 Sun, Y., Dai, Y., Liu, Y. & Chen, S. *Phys. Chem. Chem. Phys.* **14**, 2278-2285, (2012).

Summary of this thesis

In this thesis, the author investigated two types of interaction between metal and metal/metal oxide; part I is focused on the metal–metal interaction for Ni@Ag catalysts, and part II deals with the metal–metal oxide interactions among Pd-CoO_x, Pd-$CoAl_2O_4$, and Ru-CoO_x catalysts.

In Chapter 1, the author has developed Ag-Ni/SiO_2 catalysts by using galvanic deposition method for CO oxidation. Galvanic deposition between Ag and Ni at –60 °C allowed the formation of a Ni-Ag core-shell (Ni@Ag) structure. Ni@Ag catalysts showed high activity for CO oxidation which is a model reaction.

In Chapter 2, the author has applied the study of Chapter 1 to various 3d transition metals (Fe, Co, Ni, Cu) as well as Ni. Ag-M bimetal catalysts exhibited higher catalytic activity for CO oxidation compared to the Ag, Fe, Co, Ni, and Cu mono-metal catalysts. AgNi bimetal catalyst showed especially excellent activity and TOF. DFT calculation revealed that density of states of Ag was shifted to Fermi level by contact with Ni(111). These results suggest that small Ag NPs or thin Ag shell structure on Ni strongly enhances adsorption of molecule, likely due to the modification of Ag electronic state by adjacent Ni.

In Chapter 3, the author has developed Pd/Co/Al_2O_3 catalyst, which has rich interfaces between PdO and CoO_x, prepared by galvanic deposition method. Pd/Co/Al_2O_3 catalyst prepared by galvanic deposition method exhibited a notable catalytic activity for methane combustion. The high catalytic performance can be attributed to the higher reducibility of PdO NPs on CoO_x species.

In Chapter 4, the author has developed a Pd/$CoAl_2O_4$/Al_2O_3 catalyst with more stable contact between Pd and Co species based on the results obtained in Chapter 3. By using galvanic deposition method, Pd/$CoAl_2O_4$/Al_2O_3 catalyst which was comprised of a $CoAl_2O_4$ phase on γ-Al_2O_3 and dispersed Pd nanoparticles of 2–7 nm in size on a $CoAl_2O_4$ phase was successfully synthesized. This Pd/$CoAl_2O_4$/Al_2O_3 catalyst showed the highest methane combustion activity among the catalysts tested herein even when PdO was initially present on the catalysts. Operando XAFS measurements revealed that the light-off temperature decreased for the PdO phase (i.e., the main active species) generated at lower temperatures. As revealed by CH_4-TPR, PdO in Pd/$CoAl_2O_4$/Al_2O_3 catalyst was reduced at low temperatures by CH_4. PdO species of the catalyst prepared by GD method were effective in activating the C–H bond of CH_4.

In Chapter 5, the author has demonstrated what species of Pd nanoparticle catalysts was the highly active for methane combustion by using time-resolved in situ DXAFS measurement. The PdO nanoparticle was reduced by CH_4 as a 2-step model involving generation of Pd^0 nucleation and growth of Pd^0 domain in a PdO particle. From the above results, the PdO-Pd^0 pair site was highly active species for methane combustion and accelerates the C–H dissociation associated with PdO reduction.

In Chapter 6, the author has described that Ru/Co catalysts prepared by the galvanic deposition method showed Ru shell structure on CoO_x nanoparticles (Co@Ru). Co@Ru catalyst showed high performance for the NO-C_3H_6 reaction compared to the conventional catalysts because of the Ru shell

structure having high reducibility. Owing to the Ru shell structure as well as the Co_3O_4 species, Co@Ru catalyst showed superior catalytic activity for the NO-C_3H_6-CO-O_2 reaction compared to Ru/Co catalyst prepared by sequential impregnation method and Ru/Al_2O_3. The Ru shell structure also contributed to the suppression of Ru vaporization.

In summary, the metal–metal interaction and metal–metal oxide interaction regarding bimetal catalysts for various oxidation reaction has been investigated. The authors discovered that the change of electronic state of Ag in the Ni@Ag structure improved the CO oxidation activity. In the case of the oxidation reaction participating in the metal species, bimetallization of noble metal and base metal was effective as catalyst design based on the d-band-center theory. In the reaction proceeding on the metal oxide surface (*i.e.* methane combustion and three-way reaction), the redox property of the noble metal oxide was involved in the reaction activity. The contact between the noble metal species and the base metal oxide promoted the reducibility of noble metal to improve the catalytic activity. The galvanic deposition method provided a bimetallic catalyst with a core shell or Janus structure of a combination of a noble metal and a base metal.

List of Publications

General introduction

1. Synthesis of Supported Bimetal Catalysts using Galvanic Deposition Method
   Yuji Mahara, Junya Ohyama, Kyoichi Sawabe, Atsushi Satsuma
   The Chemical Record, under revision.

Chapter 1

2. Enhanced CO oxidation Activity of Ni@Ag Core-Shell Nanoparticles
   Yuji Mahara, Hiroyuki Ishikawa, Junya Ohyama, Kyoichi Sawabe, Yuta Yamamoto, Shigeo Arai, Atsushi Satsuma
   Chemistry Letters 43 (2014) 910–912.

Chapter 2

3. Ag–M (M: Ni, Co, Cu, Fe) bimetal catalysts prepared by galvanic deposition method for CO oxidation
   Yuji Mahara, Hiroyuki Ishikawa, Junya Ohyama, Kyoichi Sawabe, Atsushi Satsuma
   Catalysis Today 265 (2015) 2–6.

Chapter 3

4. Enhanced activity for methane combustion over a $Pd/Co/Al_2O_3$ catalyst prepared by a galvanic deposition method
   Yuji Mahara, Junya Ohyama, Takumi Tojo, Hiroyuki Ishikawa, Atsushi Satsuma
   Catalysis Science & Technology 6 (2016) 4773–4776.

Chapter 4

5. Methane combustion over $Pd/CoAl_2O_4/Al_2O_3$ catalysts prepared by galvanic deposition
   Yuji Mahara, Takumi Tojo, Kazumasa Murata, Junya Ohyama, Atsushi Satsuma
   RSC Advances 7 (2017) 34530–34537.

Chapter 5

6. Time-Resolved in situ DXAFS Revealing Highly Active Species of Pd Nanoparticle Catalyst for CH_4 Oxidation
   Yuji Mahara, Kazumasa Murata, Kakuya Ueda, Kazuo Kato, Junya Ohyama, Atsushi Satsuma
   In Preparation.

Chapter 6

7. Formation of Ru Shell on Co/Al_2O_3 by Galvanic Deposition Method and Its High Catalytic Performance for Three-Way Conversion
   Junya Ohyama, Hiroyuki Ishikawa, Yuji Mahara, Takumi Nishiyama, Atsushi Satsuma
   Bulletin of the Chemical Society Japan 89 (2016) 914–921.

Other Publication

8. Metal-Support Interaction Concerning Particle Size Effect of Pd/Al_2O_3 on Methane Combustion
   Kazumasa Murata, Yuji Mahara, Junya Ohyama, Yuta Yamamoto, Shigeo Arai, Atsushi Satsuma
   Angewandte Chemie International Edition 56 (2017) 15993–15997.

9. Direct synthesis of lactams from keto acids, nitriles, and H_2 by heterogeneous Pt catalysts
   S. M. A. H. Siddiki, Abeda S. Touchy, Ashvini Bhosale, Takashi Toyao, Yuji Mahara, Junya Ohyama, Atsushi Satsuma, Ken-ichi Shimizu
   ChemCatChem 10 (2018) 1–8.